POLITECNICO DI MILANO
DEPARTMENT OF PHYSICS
DOCTORAL PROGRAMME IN PHYSICS

DEVELOPMENT AND APPLICATIONS OF A TIME DOMAIN NEAR INFRARED SPECTROSCOPY INSTRUMENT BASED ON WAVELENGTH SPACE MULTIPLEXING

Doctoral dissertation of:

Rebecca Re

Supervisor:
Prof. Alessandro Torricelli
Tutor:
Prof. Rinaldo Cubeddu
The Chair of the Doctoral Programme:
Prof. Franco Ciccacci

2009 - 2011
XXIV Cycle

Ai miei genitori
To my parents

Ringraziamenti

Ho iniziato il mio dottorato tre anni fa con grande entusiasmo avendo capito durante il precedente periodo di tesi, svolto presso il Dipartimento di Fisica del Politecnico di Milano, che la ricerca era ciò che amavo lavorativamente parlando. Ho deciso di intraprendere il dottorato qui perchè "chiudermi" pomeriggi interi in laboratorio con quelli che per me erano "Prof." durante la tesi non era mai stato un peso, ma un occasione per imparare. Durante questi tre anni ho continuato su questa strada con persone che da "Prof." sono diventati compagni di avventura, con insegnamenti che sui libri non si trovano, e non sto parlando solo di strumenti che non ci sono e si creano (perchè come disse qualcuno un ingegnere quello che c' è lo fa funzionare e quello che non c' è lo fa), sto parlando di qualcosa che va al di là di pubblicazioni su riviste, sto parlando dell' insegnamento personale, educativo. E' più che scontato che io debba ringraziare tutti i "Prof." del dipartimento per gli insegnamenti datomi, ma assolutamente doveroso ringraziare persone, che mi sono state accanto come una grande famiglia, e come tale mi hanno sgridata costruttivamente per gli errori e mi sono stati vicini nelle difficoltà che inevitabilmente la vita in tre anni ti pone di fronte. Grazie a tutti per esserci stati e per avermi portato oggi a pensare che mi dispiace proprio che il dottorato sia finito. Vi ricorderò sempre ovunque andrò a lavorare dopo questa esperienza.

Un ringraziamento particolare va al mio relatore Prof. Alessandro Torricelli: uomo di poche ma efficaci parole, che non verranno mai dimenticate, grazie per avermi consigliata ma non obbligata, grazie per avermi fatto scegliere da sola anche sbagliando, perchè sbagliando si impara...quando il danno non è irreparabile!; Prof. Davide Contini: grazie per avermi "tirata su" (come dice lui) durante la tesi e avermi poi "abbandonata" mano a mano durante il dottorato, lasciandomi l'autonomia che ora ho, e per avermi sempre aiutata a credere in me stessa, anche quando mi dimenticavo di farlo; Dott. Lorenzo Spinelli: grazie Lorenzo perchè da te ho imparato cosa vuol dire essere Prof., ho imparato da te (spero bene) ad interfacciarmi con gli

studenti, con le persone, mi hai insegnato ad essere paziente perchè io ti vedo così come una persona molto paziente e disponibile; Prof. Rinaldo Cubeddu: grazie innanzitutto per avermi accolta nel gruppo di ottica biomedica fin dalla tesi triennale. Grazie per avermi chiesto se ero sicura di voler affrontare la laurea specialistica durante il colloquio di ammissione, perchè quando le ho risposto con forte veemenza "sì"ho capito che stavo lottando, per quello che volevo. Grazie a tutti per essere stati il mio gruppo di lavoro.
E come dimenticare la Lucia Zucchelli, Matteo Caffini e Luca Fieramonti ovvero quelli del soppalco. Come dimenticare i momenti passati assieme a cercare di risolvere esercizi e qualunque genere di problema davanti ad una bella scatola di biscotti! Un grazie doveroso va anche a Andrea Farina, mio primo compagno di ufficio, che ho ampiamente stressato nei primi mesi di dottorato. Grazie ancora a Paola Taroni, Andrea Bassi, Antonio Pifferi, Cosimo D'Andrea, Daniela Comelli e Luca Valentini per i piacevoli pranzi accompagnati da discussioni "fisiche". Grazie ai tecnici informatici, elettronici e meccanici: Giuseppe, Amedeo, Maurizio, Riccardo, Carlo, Mauro, Antonio e Luciano, ormai in pensione, per avermi aiutata a creare l'ossimetrino.
Thank you to Clifford C. Dacso, director of the"Abramson Center For The Future of Health" of Houston. Thank you for welcoming me in your group. Grazie al Prof. Luca Pollonini per avermi accolta a braccia aperte a Houston, sia da un punto di vista lavorativo sia da un punto di vista umano. Grazie infinite Luca, e grazie anche a tua moglie Marga, per avermi aiutata ad affrontare la vita texana e grazie infinite per la bicicletta, unico modo per muovermi in quella che più che una città sembra una provincia, non vi dimenticherò mai.
Devo ringraziare qualcuno anche al di fuori dal lavoro.

In particolare grazie alla Ile (Ilenia Pastorelli) e alla Meli (Melissa Andrini) per essermi state Amiche. Grazie per le espatriate, per i caffè spettegulez, anche oltreoceano, e per quando avete rispettato tutto il tempo che avevo bisogno per uscire da situzioni spiacevoli!

Grazie a tutti gli altri amici e amiche che per ovvi motivi non posso citare. Ed infine, grazie a coloro ai quali è dedicata non solo questa tesi, ma tutto il mio percorso di studi e di vita: i miei genitori.

Grazie al mio papà, Gian Piero Re, per aver lavorato tanto anche quando finalmente sei andato in pensione. Grazie per quando mi fai capire le cose anche con un semplice sguardo $\cdots$ a volte tante parole non servono. Tra noi non sono mai servite e mai serviranno perchè ci capiamo così. Sono contenta perchè finalmente ce l' ho fatta a scrivere il mio e il tuo nome da qualche parte, visto?

Grazie alla mia mamma Maria Rosanna Canevari. Anche tu hai lavorato tanto, e a differenza di papà tu parli tanto, fino troppo, e io ti seguo a ruota

$\cdots$ e tu mi ascolti anche quando da te sono le tre di notte e in America è giorno. Grazie per ascoltarmi ma soprattutto grazie, mamma, per avermi detto quel caldo giorno d'agosto se dovevo fare qualche test d'ingresso per qualche università, è per colpa tua se oggi mi dottoro!

Rebecca Re

Preface

During the 3 years PhD course, I focused on the development of an innovative time-resolved near infrared spectroscopy instrument, based on a new modality to inject light into the tissue called wavelength space multiplexing, on its characterization and *in vivo* applications. I also contributed to the development of a CW-NIRS prototype, which to our knowledge is the first example of wireless NIRS instrument for the real time monitoring of the tissue's hemodynamic parameters.

Noninvasive monitoring of blood and tissue oxygenation is a research field where functional near-infrared spectroscopy (fNIRS) can be applied. This technique is employed both to experimentally and clinically investigate cerebral oxygenation and hemodynamic response to a wide range of stimuli in the human brain and to study muscle oxidative metabolism in healthy and pathological subjects. The interest in the neuroscience field is to understand the links between the cortical activation and the hemodynamic changes in the different cortices. Brain activity is, in fact, indicated not only by an electrical activation but also by a vascular response to the neuronal activity that is associated with an increasing of blood oxygenation and volume. Physiological changes are widely studied also in other body compartment such as the muscular system. When muscular fibers are employed for a task, typically an increase of the deoxy-hemoglobin and a decrease of the oxy-hemoglobin is observed. The oxygen saturation reflects the dynamic balance between oxygen supply and demand by the muscle and can be considered a measure of the energy consumption for muscle force production. These information can be used during rehabilitation or training processes.

fNIRS is an optical technique that allows to non-invasively monitor the hemodynamic changes in human tissues exploiting the information carried by light that has traveled through the tissue itself. The hemodynamic changes are well represented by the variations of blood volume and of the oxygen saturation that can be evaluated knowing the content of the oxy- and deoxy-hemoglobin. In 1977 Jobsis discovered that, in the near-infrared spectral

region (700-1000 nm), biological tissues can be considered as transparent and their oxygenation status can be monitored by the measurement of the medium's absorption coefficient, exploiting the differences in the absorption spectrum of the different chromophores, such as oxy- and deoxy-hemoglobin. Accordingly, simple attenuation measurements should be enough to determine the oxy- and deoxy-hemoglobin content. Biological tissues are however diffusive media, i.e. light is not only absorbed, but also undergoes many scattering events before exiting from the tissue. This phenomenon is called Photon Migration. For this reason, simple attenuation measurements at two wavelengths are not enough to extrapolate information about both the absolute values of the oxy- and deoxy-hemoglobin, while only the relative variation can be known with this approach. The NIRS modality, which is based on absorption measurement, is called continuous wave (CW). With a single CW measurement is not possible to determine simultaneously the absorption and the scattering coefficient's values. In order to obtain absolute values with this approach is necessary to perform measurements at different interfiber distances or with more than two wavelengths. In the first case, measurements are performed at least at two different intefiber distances. The smallest one (less than 1 cm) will investigate only the superficial layer of the tissue, the longest one (3-4 cm) will probe both the superficial and the deeper layers. This is due to the typical "banana" shape of light volume in the tissue under the two optodes. Light is narrow near the source optode, more broadened between the injection and detection one. In the second case, is necessary to exploit the information coming from a third wavelength, for example the one around the water absorption's peak, to extrapolate a value for the scattering coefficient at that wavelength. Employing tabulated data is then possible to extract the entire scattering spectrum and compute the absorption coefficient's values at the oxy- and deoxy-hemoglobin wavelengths. Whit this method is however not possible to discriminate between superficial and depth signal. CW technique offers the possibility to have low cost, compact and wireless instruments but has still low depth sensitivity. In this thesis, an innovative instrument based on CW-NIRS will be presented. To our knowledge is the first example of portable and wireless NIRS instrument for the real time monitoring of the hemodynamic parameters. With the time-domain (TD) approach is possible to discriminate between absorption and scattering coefficient. The substantial advantage of the TD modality is the possibility to improve the depth sensitivity employing photons' temporal information encoded in the detected signal. Photons traveling few hundreds of picoseconds inside the medium, have a little probability to reach the deeper region of the tissue, while photons that spend more time within the tissue have a higher probability to reach deeper layers. Depth sensitivity improvement is

a fundamental goal for near infrared spectroscopy because of the anatomical configuration of the tissue under examination, which is typically organize as a layered structure. The only disadvantage of the TD technique is the high cost of some components and the impossibility, with the actual technology, to build compact instruments, if the number of channels required is high. Typically time-domain instruments use a Time Multiplexing (TM) approach to inject light of two different wavelengths into the tissue. Laser pulses are delayed and injected in the same optical fiber, and both the wavelengths are acquired in the same temporal window. With this modality problems of cross-talk between pulses might hamper the overall performances of the system. To avoid the cross-talk between the wavelengths and to increase the signal-to-noise ratio, we have introduced, for the first time, a new approach to inject and collect light into the tissue: the wavelength Space Multiplexing (SM). The two wavelengths are injected alternatively in the two optical fibers by means of an optical 2X2 switch. In this way, we acquire in each detection line and in each temporal window only one wavelength at a time, exploiting the full temporal and dynamic range of the acquisition board.

In chapter 1 of this thesis an overview of the NIRS technique will be presented. At first the optical properties of human tissues and how to extrapolate the hemodynamic parameters will be shown. Then an explanation of the different NIRS approach, i.e. continuous wave, frequency and time domain is described. In the second part of the chapter, the radiative transport theory will be introduced and the diffusion equation presented. Then the solutions of the diffusion equation for the continuous wave and time domain approach will be extrapolated for a homogeneous medium. Finally we will show how the model has to be changed if we consider a heterogeneous medium and how we fit our time-domain data in order to obtain the optical parameters.

In chapter 2, 3 and 4 my contributes to TD and CW NIRS will be presented.

In chapter 2 the TD instrument based on wavelength SM, I developed during my PhD, will be described. The initial version of the instrument had two injection and two detection channels. It was characterized and tested during preliminary *in vivo* measurements. The final version of the instrument has 16X4 channels and is suitable for monitoring the hemodynamic changes in human tissues and to perform brain imaging as well. All the different upgrade stages of the instrument, the system characterization and improvements, and the future perspective will be presented in this chapter.

In chapter 3 three different *in vivo* applications, performed with the instrument described in chapter 2, will be presented. The applications are:

- TD-fNIRS vs. Laser Doppler Flowmetry (LDF): simultaneous acquisitions to provide an experimental evidence to the "Time-Gated (TG) " method we used to analyze data.

  TG method allows to separate from the whole signal the contribution coming from the deeper and the upper layer of a tissue, spreading the temporal information encoded in our signal. It was developed at our department and these measurements give an experimental evidence of it. From the TD-fNIRS signal is possible to extrapolate both the contributions, from the LDF the one coming from the upper layer, being the Doppler signal related to the surface flowmotion due to the peripheral autoregulation. During a Valsalva maneuver, i.e. a forced exhalation with a closed glottis, specific changes occur, which cause variations in the superficial perfusion. We took measurements on the prefrontal cortex of eight healthy volunteers and we found good correlations between the LDF signal and the TD-fNIRS signal coming from the upper layers, demonstrating the goodness of our semi-empirical method.

- TD-fNIRS vs. Electroencephalography (EEG): simultaneous acquisitions to test the feasibility of co-registration, on brain cortex, of these two techniques during a divided attention task.

  One of the goals of the modern diagnostics is to combine different techniques. This study aimed at the monitoring of both the hemodynamic and electrical activity on the prefrontal cortex, during a divided attention task. Divided attention is the skill to distribute the limited mental resources to different sources of information at the same time. Sixteen healthy volunteers were undergone to auditory and visual stimuli. Results suggest that there is a hemodynamic activation modulated by the task in the prefrontal cortex and that there is a temporal cascade among activations with different origin: electrical, systemic and hemodynamic.

- TD-fNIRS and Electrical muscle stimulation (EMS): hemodynamic response of muscle and brain during electrical stimulation at different current thresholds.

  During this study we monitored, on nine healthy volunteers, the muscle behavior during electrical stimulation, in order to understand muscles hemodynamic changes when the stimulation current is varied through different thresholds. The electrical stimulation affects at first muscle but can also indirectly activate peripheral and association cortices. For this reason we monitored also the hemodynamics activations of the

brain. Preliminary results are available on muscle but further investigations are still in progress.

In chapter 4 a report of my activity, during a six months period at the "Abramson Center for Future of Health" (Houston, TX), will be presented. Here I contributed to the development of a CW-NIRS wireless prototype. In addition to the NIRS probe, we used a cardiovascular sensing system that includes an electrocardiogram (EKG) and a photoplethysmograph (PPG) sensor. At first, the instrument in all its parts will be presented. After that an *in vivo* application during muscle incremental exercise will be presented. The final goal of the measurement campaign is to find new physiological indexes and correlations between them, to better identify and quantify the phenomenon of the muscular fatigue. These indexes can be applied in the cardiac rehabilitation, in the muscular training and in the evaluation of muscle performances during spaceflight.

Contents

CHAPTER 1

Functional Near Infrared Spectroscopy (fNIRS): Principles and Theory

The idea to monitor the oxygenation of biological tissues with light was feasible after 1977, when Jobsis demonstrated that was possible to investigate the biological tissues with near infrared light (600-900 nm). In this spectral region photons can propagate through the tissue carrying out information about its optical properties [1]. To estimate the variation of the typical oxygenation index, i.e. saturation (SO_2) and blood volume (tHb), it is enough to estimate the changes in the absorption coefficient (μ_a) of the tissues under investigation, as explained in paragraph 1.1, but to estimate the exact content of those parameters and to have information also about the blood content of the oxy- and deoxy-hemoglobin (O_2Hb and HHb), an evaluation of the scattering coefficient (μ_s) is necessary. The technique that allows to extrapolate these optical parameters is called Near Infrared Spectroscopy (NIRS) or functional NIRS (fNIRS), which allows the monitoring of the hemodynamic changes during particular tasks. The different implementation modalities of this technique will be presented in paragraph 1.2. Paragraph 1.3 will be dedicated to the explanation of the theoretical models of the Photon Migration theory. In paragraph 1.4, how to extrapolate the absolute values of the optical parameters with Time Domain (TD) and Continuous Wave (CW) approaches will be clarified. Finally, in paragraph 1.5 will be explained how to take into account the heterogeneity of the biological tissues during data analysis both in Cw and TD-NIRS modalities.

1.1 Tissue's optical properties

The biological tissues are a really complex matter, because they are made of different layers with an heterogeneous compositions. Many chromophores are then present (O_2Hb, HHb, lipid, water, collagen, ...). When light travels in the tissues is selectively absorbed by one chromophore depending on the wavelength [2, 3]. However biological tissues are diffusive media, and light is not only absorbed but also scattered from the particles inside the tissues. For this reason is important to better understand the phenomenon of the absorption and the scattering of the light and how to extrapolate information about the chromophore of interest as explained in the following sections.

1.1.1 Absorption

Absorption is the phenomenon related with the absorption bands of molecules. When an electron within a molecule is raised by photon absorption to an excited state, the relaxation to the ground state can occur following a non-radiative decay process with the emission of heat and/or a radiative process with the emission of a photon at a different wavelength (luminescent effect). When the electron relaxes to the ground state with the emission of a photon, we have the fluorescence or phosphorescence. These photons are re-emitted at a longer wavelength and can continue their migration through the medium. For our descriptions we will neglect all these effect, but we will consider the absorbed photons as lost for propagation, i.e. the absorption causes a decrease in the energy of the injected beam.

In turbid media, absorption comes from the interaction of light with molecules both of the background medium and of the dispersed particles. If we assume that the medium is constituted of identical absorbers we can define the absorption coefficient as:

$$\mu_a = \tau\sigma_a \quad [cm^{-1}], \tag{1.1}$$

where τ is the density of absorbers per unit of volume [cm^{-3}] and σ_a is the absorption cross-section defined as:

$$\sigma_a = \frac{P_{abs}}{I_0} \quad [cm^2], \tag{1.2}$$

where I_0 is the intensity of the incident radiation, while P_{abs} is the power of the radiation which was absorbed during the interaction. The reciprocal of μ_a is the absorption mean free path (l_a) and represent the average distance that a photon covers before being absorbed. The particles inside the medium

responsible of the absorption are called *chromophores*; is possible to expressed the μ_a in function of them as follow:

$$\mu_a(\lambda) = \varepsilon(\lambda) \cdot c, \tag{1.3}$$

where $\varepsilon(\lambda)$ is the molar extinction coefficient [$M^{-1}cm^2$] at wavelength λ, which gives a measure of the absorbing power of the species, while c is the molar concentration of the absorption species [M cm^{-3}].

Typical values of the absorption coefficient reported at the near-infrared wavelength range for biological tissue are about ≤ 0.04 mm^{-1} [4, 5].

1.1.2 Scattering

Light scattering originates from the interaction of photons with structural heterogeneities inside material bodies at the wavelength scale. The interaction between a photon and a molecule results in a photon moving in a different direction and a molecule that may maintain, increase or decrease its energy. If the energy of the scattered photon is the same as the incident one, the scattering is called *elastic*, as the scattering Rayleigh; if the energy is higher or lower is called *inelastic*, as the scattering Raman. Light scattering can be also influenced by the movement of the scattering particles, e.g. Doppler effect [6]. For our aim the scattering type we have to take in consideration is the elastic one.

Elastic light scattering originates from the heterogeneity of the refractive index inside the medium [7]. For media in which propagation is dominated by multiple scattering, as the biological tissues, the effect of the background is usually negligible, so we can consider only the effect of the particles. The scattering coefficient can be then expressed as:

$$\mu_s = \rho\sigma_s \quad [cm^{-1}], \tag{1.4}$$

where ρ is the density of the scatterers per unit of volume [cm^{-3}] and σ_s is the scattering cross-section defined as:

$$\sigma_s = \frac{P_{sca}}{I_0} \quad [cm^2], \tag{1.5}$$

where I_0 is the intensity of the incident radiation, while P_{sca} is the power of the radiation which was spatially redirected. In this equation we assumed that the scattering cross-section is independent of the relative orientation of the incident light and scatterer, that is equivalent to consider the scattering particles as spherical objects. As we did with the absorption, we can also introduce the reciprocal of μ_s: the scattering mean free path (l_s), which

represents the average distance that a photon cover between two scattering events.

To describe scattering events, is necessary to introduce also the *scattering phase function*: $p\left(\hat{s},\hat{s'}\right)$, also called scattering function. It describes the probability that a photon travelling in direction $\hat{s}$ is scattered within the unit solid angle around the direction $\hat{s'}$. In the case of unpolarized radiation and considering isotropic scatterers (spherical particles or randomly oriented non-spherical particles), the scattering function only depends on the scattering angle ϑ, i.e. the angle between directions $\hat{s}$ and $\hat{s'}$, and is possible to write: $p\left(\hat{s},\hat{s'}\right) = p\left(\vartheta\right)$. The following normalization for the scattering function is thus assumed:

$$\int_{4\pi} p\left(\hat{s},\hat{s'}\right) d\Omega' = 2\pi \int_{0}^{\pi} p\left(\vartheta\right) \sin\left(\vartheta\right) d\vartheta = 1. \tag{1.6}$$

When propagation is dominated by multiple scattering, a single number can be sufficient to characterize the scattering function. This number is the anisotropy factor g, defined as the average cosine of the scattering angle:

$$g = \langle \cos\vartheta \rangle = 2\pi \int_{0}^{\pi} p\left(\vartheta\right) \cos\left(\vartheta\right) \sin\left(\vartheta\right) d\vartheta. \tag{1.7}$$

The anisotropy factor can assume values between -1 and 0 (back scattering), 0 (isotropic diffusion) and between 0 and 1 (forward scattering). To take into account the asymmetry of the scattering phenomenon is common to define the *reduced scattering* or transport coefficient of the medium as follow:

$$\mu_s' = \mu_s \left(1 - g\right). \tag{1.8}$$

For Rayleigh scattering, small particles size in comparison with the wavelength of the incident light, g=0, i.e. the scattering is isotropic. In the biological tissues, typically, the dimensions of the scattering particles are comparable with the wavelength of the incident light (Mie scattering), and the propagation is dominated by multiple scattering events. In this case is not possible to neglect g and the reduced scattering coefficient becomes the most important parameter to describe the scattering. The reciprocal of μ_s' is the transport mean free path (l^{-1}) that is the mean distance travelled by a photon along the initial direction of propagation before it has effectively "forgotten" its original direction of motion. Measurements of the optical properties of biological tissue show a significant intersubject variability and

a dependence on the spectral range considered. Typical values of $\mu_s^{'}$ reported at near-infrared wavelengths range are: ∼0.5-1 mm^{-1} for muscles [4, 5], ∼0.3-2 mm^{-1} for the forehead [8, 9] and ∼0.8-4 mm^{-1} for brain (gray and white matter) [10, 11].

1.1.3 Hemodynamic parameters

From the knowledge of the absorption coefficient is possible to extrapolate the concentration of the different chromophores inside the tissue. In fact, if we consider the biological tissues as composed of n chromophores, equation 1.3 becomes:

$$\mu_a(\lambda) = \sum_{i=1}^{n} \varepsilon_i(\lambda) \cdot c_i. \tag{1.9}$$

The problem change into finding the solution for the following linear system:

$$\bar{\mu}_a(\lambda) = \bar{\varepsilon}(\lambda) \cdot \bar{c}, \tag{1.10}$$

where: $\bar{\mu}_a(\lambda)$ is the vector of the absorption coefficient at different wavelengths, $\bar{\varepsilon}(\lambda)$ is the matrix of the extinction coefficients for the n chromophores and $\bar{c}$ is the vector of the chromophores concentrations. To solve this system is necessary to performed n measurements of the absorption coefficient, each at a different wavelength λ.

1.2 Functional Near Infrared Spectroscopy

Functional near-infrared spectroscopy (fNIRS) is the technique that allows the extrapolation of the typical hemodynamic parameters from the optical properties of a biological tissue [12]. The hemodynamic parameters, such as O_2Hb, HHb, SO_2 and tHHb are considered the basic parameters in the monitoring of brain and muscles activation [13]. The interest in the neuroscience field is to understand the links between the cortical activation and the hemodynamic changes in the different cortices. The brain activity is in fact indicated, not only from an electrical activity, but also from a vascular response to the neuronal activity that imply an increasing of the blood oxygenation and volume [14, 15]. The physiological changing are important also in other body compartment, such as in the muscular system. When muscular fibers are employed for a task, typically is possible to observe an increase (decrease) of the HHb (O_2Hb) [16, 17]. Is then necessary to develop systems for the real-time and in-vivo monitoring of the hemodynamic changes of tissues.

In these kinds of applications, we are interested in finding the concentration of only two chromophores: O_2Hb and HHb. The previous n order system (equation 1.10 in paragraph 1.1.3) becomes a system with two equation and two unknowns. Solving it respect to the concentration we have:

$$\begin{aligned} c_{O_2Hb} &= \frac{\mu_a(\lambda_1)\varepsilon_{HHb}(\lambda_2) - \mu_a(\lambda_2)\varepsilon_{HHb}(\lambda_1)}{\varepsilon_{O_2Hb}(\lambda_1)\varepsilon_{HHb}(\lambda_2) - \varepsilon_{O_2Hb}(\lambda_2)\varepsilon_{HHb}(\lambda_1)} \\ c_{HHb} &= \frac{\mu_a(\lambda_2)\varepsilon_{O_2Hb}(\lambda_1) - \mu_a(\lambda_1)\varepsilon_{O_2Hb}(\lambda_2)}{\varepsilon_{O_2Hb}(\lambda_1)\varepsilon_{HHb}(\lambda_2) - \varepsilon_{O_2Hb}(\lambda_2)\varepsilon_{HHb}(\lambda_1)} \end{aligned} . \tag{1.11}$$

From the graph in figure 1.1, we observe that is possible to exploit the differences between O_2Hb and HHb absorption spectra, and performed only two measurements at two different wavelengths around the isosbestic point. Then is possible to calculate the tHb and SO_2 as follow:

$$tHb = c_{O_2Hb} + c_{HHb}, \tag{1.12}$$

$$SO_2 = \frac{c_{O_2Hb}}{tHb}. \tag{1.13}$$

The extrapolation of the hemodynamic parameters can be accomplished with the employment of different NIRS approaches [13], as shown in the following paragraphs.

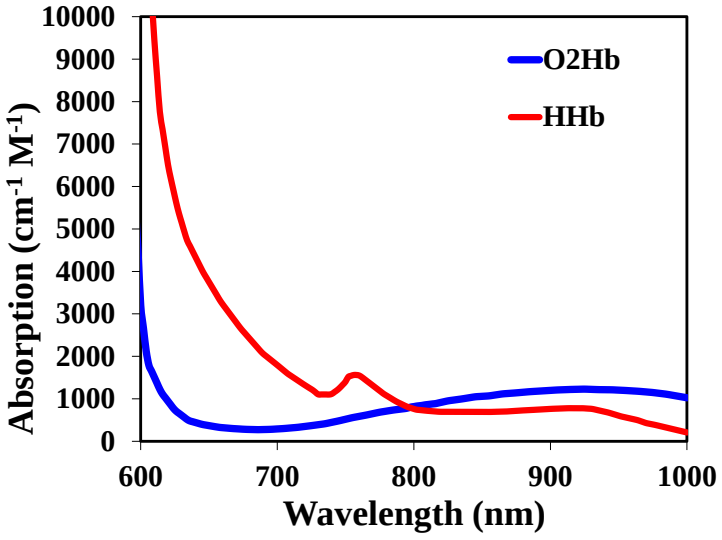

Figure 1.1: Absorption spectra for O_2Hb and HHb in the near infrared region

1.2.1 Continuous wave measurement (CW)

In the continuous wave NIRS (CW-NIRS), light with a constant intensity is injected into the tissue. According to the Lambert-Beer equation [18], light travelling in a non diffusive medium (transparent) of thickness d undergoes a loss of intensity equal to:

$$I_{OUT} = I_{IN} \exp\left(-\mu_a d\right), \tag{1.14}$$

where I_{IN} and I_{OUT} are respectively the intensity of light injected and detected from the tissue, with a reflectance or transmittance geometry. From the Lambert-Beer equation we can obtain the attenuation that light undergoes in a transparent medium:

$$A = -\ln\left[\frac{I_{OUT}}{I_{IN}}\right] = \mu_a d. \tag{1.15}$$

Biological tissues are diffusive media, so that in the attenuation is necessary to take into account the scattering. The expression for the attenuation in thin samples becomes:

$$A = -\ln\left[\frac{I_{OUT}}{I_{IN}}\right] = (\mu_a + \mu_s^{'})d, \tag{1.16}$$

where we can define $\mu_{tot} = \mu_a + \mu_s^{'}$. If we perform a single CW measurement we will be able to determine only the value of the μ_{tot}, estimating the attenuation of the light, but without disentangle the contributions of absorption and scattering. To overcome this problem, it is possible to use a modified Lambert-Beer equation where some correction factors are added [19, 20]:

$$A\left(t,\lambda\right) = -\ln\left[\frac{I_{OUT}}{I_{IN}}\right] = \varepsilon\left(\lambda\right)\cdot c\left(t\right)\cdot DPF(\lambda) + G\left(\lambda\right), \tag{1.17}$$

where: $\varepsilon\left(\lambda\right)$ and $c\left(t\right)$ are respectively the extinction coefficient and the concentration of the chromophore, $DPF(\lambda) = d \cdot B\left(\lambda\right)$ is the differential pathlength factor, which take into account the increase in pathlength between source and detector for scattered light. $G\left(\lambda\right)$ is a parameter related with the photons loss because of the scattering. Without a perfect knowledge of the parameter $G(\lambda)$ is not possible to estimate A and the absolute concentrations of the cromophores. Considering t_0 the time when the experiment started and t_i any time during the experiment, we can express the relative variations of the attenuation as:

$$\partial A\left(\lambda\right) = A\left(t_i,\lambda\right) - A\left(t_0,\lambda\right). \tag{1.18}$$

From the previous equation we can write:

$$\partial A\left(\lambda\right) = \partial c \cdot \varepsilon\left(\lambda\right) \cdot DPF(\lambda), \tag{1.19}$$

obtaining finally [15]:

$$\partial c = \frac{\partial A\left(\lambda\right)}{\varepsilon\left(\lambda\right) \cdot DPF(\lambda)}. \tag{1.20}$$

The modifies Lambert-Beer equation is based on three assumptions:

1. High scattering without consistent changes during the measurements.
   This assumption allows to consider $DPF(\lambda)$ constant at a certain wavelength and to disregard the loss of light intensity due to scattering (G) as long as changes in attenuation are assessed. This assumption is plausible because changes on blood flow are mostly due to the absorption coefficient rather than to the scattering one.

2. The biological medium is homogeneous.
   This assumption is clearly wrong due to the anatomical nature of the tissues typically under examination, such as brain and muscles, which have a layered structure. For this reason the attenuation measurements have a low depth sensitivity.

3. The change in the volume sampled is homogeneous within the sampling volume.
   This assumption is strongly related with the previous one and introduce an additional source of error.

The CW measurements offer a good signal to noise-ratio and a low cost instrumentation that can be miniaturized to the extent of a wireless instrument. For this reason several commercial versions are available. Unfortunately CW methods have a series of disadvantages such as the intensity dependence on the coupling surface (the signal is affected by the skin and hairs colour), the possibility to extrapolate only the relative values of the hemodynamic parameters, with measurements at one wavelength [21], the impossibility in discriminating between the surface and deeper contributions, the sensitivity to the motion artefact and the presence of many approximation in the theoretical model. Some methods to extrapolate absolute values of the hemodynamic parameters were proposed, as the possibility to perform measurements at different interfiber distances [22] or by means of additional wavelengths (see chapter 4).

1.2.2 Frequency domain measurement (FD)

Frequency Domain NIRS (FD-NIRS), also called phase modulation spectroscopy (PSM), makes use of intensity modulated laser light (typically at radio frequencies: from 50 MHz to 1 GHz). The re-emitted wave is demodulated to obtain amplitude and phase as a function of the modulation frequency [23]. The tissue acts like a low-pass filter: the amplitude is a decreasing function of the frequency and the phase typically increases. The amplitude attenuation is due to the absorption and to the scattering, while the phase changes to the scattering, which modify the photons' optical pathlengths. The analytical expressions for amplitude and phase can be obtained by a Fourier transform of the time resolved theoretical expression. The estimation of the optical properties can thus be performed using the photon migration theory. To obtain complete information about μ_a and $\mu_s^{'}$, a scanning through all frequencies from 50 MHz to 1 GHz were required. Most of the instruments are single frequency and use a multi-distance geometry, with a method similar to the one applied for the CW measurements, with all the advantages and disadvantages related to it. One of the most important improvement compared to CW-NIRS is the possibility to extrapolate absolute values of the optical parameters [24, 25, 26].

1.2.3 Time domain measurement (TD)

In the time domain (TD) or time resolved (TR) modality, pulses of light (hundreds of picoseconds) are injected into the medium, and after travelling inside it, are recollected (with a reflectance or transmittance geometry) in order to study the Temporal Point Spread Function (TPSF). In this way is possible to study the impulse response of the tissue. The recollected pulses are broadened (because of the different paths among scattered photons), attenuated (because of the absorption of some photons) and delayed (due to the finite time that photons need to travel from the source to the detector) [27]. From these modification is possible to extrapolate the absolute value of the μ_a and $\mu_s^{'}$, after fitting the experimental TPSF with a proper theoretical model that describe the propagation of photons in a highly diffusive medium [28]. In addition TD modality has the advantage that is possible to extrapolate from the photon's arrival time, important depth information and discriminate in this way between signal coming from the surface and the deeper part of the tissue. To have information about the time of arrival of the photons, particular detection techniques and detectors with a resolution of picoseconds are necessary. For an overview of the different solutions, see ref. [29].

1.3 Photon Migration in turbid media: the radiative transport theory

If we have to consider the propagation of the light in biological tissues, and we want to create a model for it, we have to take into account that they are *diffusive media*. Diffusive media are turbid media that can be described as a background medium in which particles with different refractive index are suspended. In this condition light propagation occurs in the diffusive regime. It means that the propagation id dominated by multiple *scattering* so that photons undergo many scattering events before being detected, and is not possible to know exactly where they will be found. For this reason light propagation inside the tissue is commonly addressed with the term *Photon Migration*. Scattering interaction deflects photons along new directions of propagation. Of course light inside the tissue is affected by the *absorption* as well, which causes the disappearance of photons. Light interaction is a very complex phenomenon, but we can obtain solutions of the photon migration equations. In the following paragraphs, as light-matter interaction phenomena, we will consider only the absorption and scattering.

As shown in the paragraph before, to estimate the concentration of the hemodynamic parameters of interest we have to extrapolate the optical properties of the medium, i.e. the absorption and the scattering coefficient. Ishimaru noticed that there are two different theories to explain multiple-scattering problems [30]. The first is the analytical theory or multiple scattering theory, which it's based on the Maxwell's equations and it's really complex to solve. The other one is the radiative transport theory which is the most widely used approach to study photon migration through highly scattering media and it will be presented in next paragraphs.

1.3.1 The radiative transport equation (RTE)

The radiative transport equation (RTE) is an integro-differential equation that represents the balance of energy (conservation of energy) for light propagation through a volume element dV of an absorbing and scattering medium [30, 31]. The RTE can be obtained by balancing the different mechanisms by which the radiance at a given wavelength, $I(\vec{r}, \hat{s}, t)$, can increase or decrease inside dV. As shown in figure 1.2, the radiance is the average power that at position $\vec{r}$ and time t flows through the unit area oriented in the direction of the unit vector $\hat{s}$, due to photons moving within the unit solid angle around $\hat{s}$. From the radiance is possible to define the power dP that at time t flows within the solid angle $d\Omega$ through the elementary area

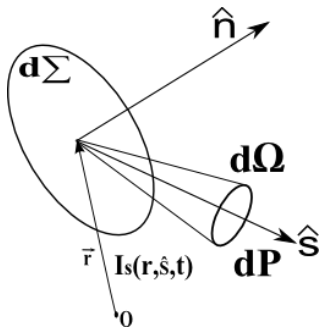

Figure 1.2: Relationship between dP and the radiance I.

$d\Sigma$, oriented along the direction $\hat{n}$ as follow:

$$dP = I\left(\vec{r}, \hat{s}, t\right) \left|\hat{n} \cdot \hat{s}\right| d\Sigma d\Omega. \tag{1.21}$$

In the most general case of time-dependent sources, the RTE can be the expressed as:

$$\begin{aligned} \frac{1}{c_m} \frac{\partial I\left(\vec{r}, \hat{s}, t\right)}{\partial t} = & -\nabla \cdot \left[\hat{s}\, I\left(\vec{r}, \hat{s}, t\right)\right] - \mu_a I\left(\vec{r}, \hat{s}, t\right) - \mu_s I\left(\vec{r}, \hat{s}, t\right) \\ & + \mu_s \int_{4\pi} p\left(\hat{s}, \hat{s'}\right) I\left(\vec{r}, \hat{s'}, t\right) d\Omega' + \varepsilon\left(\vec{r}, \hat{s}, t\right), \end{aligned} \tag{1.22}$$

where c_m is the light speed inside the medium, $\varepsilon\left(\vec{r}, \hat{s}, t\right)$ is the source term that is the power emitted at time t per unit volume and unit solid angle along $\hat{s}$, and $d\Omega'$ is the elementary solid angle in the direction $\hat{s'}$. The term on the left of equation 1.22 represents the total temporal change of energy that is propagating along $\hat{s}$ within dV, $d\Omega$ and dt. On the right, the terms are described respectively as follow:

1. net flux of energy that is propagating along $\hat{s}$, trough the volume dV, within $d\Omega$ and dt;
2. fraction of energy lost for an absorption event;
3. fraction of energy lost for a scattering event;
4. energy coming from any direction $\hat{s'}$ that is scattered in direction $\hat{s}$, within $d\Omega$ and dt;
5. energy generated along $\hat{s}$ in $d\Omega$ and dt by sources inside dV.

In figure 1.3 a graphical explanation of all the terms of the RTE.

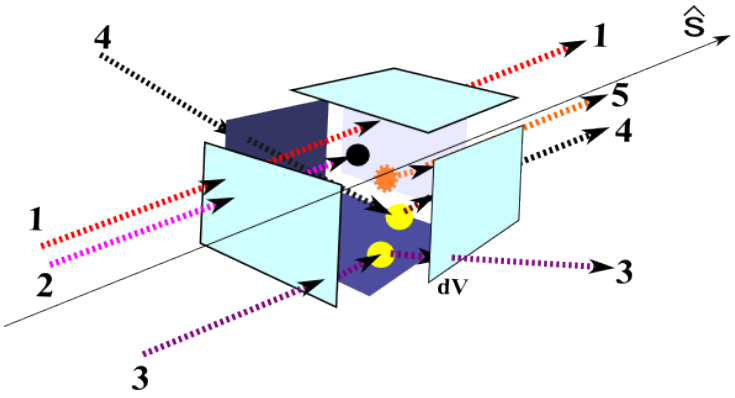

Figure 1.3: Scheme of the terms of the RTE

1.3.2 Diffusion Equation (DE)

The RTE is an integro-differential equation and the retrieval of solutions is an extremely expensive computational process, in terms of time and resources. Its solutions are usually based on numerical methods. No general analytical (closed-form) solutions are available and simpler models are usually employed. When propagation is dominated by multiple scattering, the most widely used model is based on the diffusion approximation that, in the case of time-dependent sources, consists of two simplifying assumptions [32]:

1. the radiance is considered isotropic and can be approximated by the first two terms of a series expansion in spherical harmonics:

$$I(\vec{r},\hat{s},t) = \frac{1}{4\pi}\Phi(\vec{r},t) + \frac{3}{4\pi}\vec{J}(\vec{r},t)\cdot\hat{s}, \tag{1.23}$$

   where $\Phi(\vec{r},t)$ is the fluence rate and it's obtained integrating the radiance over the entire solid angle while $\vec{J}(\vec{r},t)$ is the flux vector which represents the amount and the direction of the net flux of power.

2. time variation of the diffusive flux vector $\vec{J}(\vec{r},t)$ over a time range $\Delta t = 1/\left(v\mu_s^{'}\right)$ is negligible with respect to the vector itself and can be expressed as [33]:

$$\frac{1}{c_m\mu_s^{'}}\left|\frac{\partial\vec{J}(\vec{r},t)}{\partial t}\right| \ll \left|\vec{J}(\vec{r},t)\right|. \tag{1.24}$$

These two conditions are well fulfilled when photons have undergone many scattering events, since scattering tends to randomize the direction of light propagation. Conversely, absorption obstructs the diffusive regime, because

selectively extinguishes photons with long pathlengths. Therefore, the diffusive regime of light propagation can be established when scattering effects are predominant in absorption. Under these conditions it's possible to obtain from an integration of the RTE over all directions and expressing the flux vector as a function of the fluence rate, the following equation [18]:

$$\vec{J}(\vec{r},t) = -D\left[\nabla\Phi(\vec{r},t) - 3\int_{4\pi}\varepsilon(\vec{r},\hat{s},t)\,\hat{s}d\Omega\right], \tag{1.25}$$

where D is the diffusion coefficient defined as:

$$D = \frac{1}{3(\mu_a + \mu_s')}. \tag{1.26}$$

Under the diffusion approximation ($\mu_s' \gg \mu_a$), D can be simplified to $D = 1/\left(3\mu_s'\right)$. Equation 1.25 is called Fick's Law. If the medium has no sources or the sources are isotropic it becomes: $\vec{J}(\vec{r},t) = -D\left[\nabla\Phi(\vec{r},t)\right]$. The physical meaning of the Fick's law is that photons tend to migrate toward those regions of the medium where the photon density is smaller. Substituting it in equation 1.22, we obtain:

$$\frac{1}{c_m}\frac{\partial\Phi(\vec{r},t)}{\partial t} = D\nabla^2\Phi(\vec{r},t) - \mu_a\Phi(\vec{r},t) + 4\pi\varepsilon(\vec{r},t) \tag{1.27}$$

which represents the DE for a homogeneous medium and an isotropic source.

The DE is a partial-differential equation, and any general solution will contain unknown constants that need to be determined by using proper boundary conditions originated from the physics of the problem investigated. In the following paragraph, some solutions for interesting geometries will be presented.

1.3.3 Time Domain DE solution

The solution of the DE was calculated for different sample geometries. In our application we are interested in medium that can be considered as semi-infinite. In order to find that solution it's necessary to use the so called *method of images* (or mirror images) [34]. To apply it we need to employ the Extrapolated Boundary Condition (EBC) [35], assuming that the fluence is equal to zero not on the physical boundary of the diffusive medium, but on extrapolated surfaces at distance $z_e = 2AD$ from the physical boundary (where A is a term that take into account the refractive index mismatch on the media interfaces). The method of images allows to find solutions for

the fluence inside the medium as a superposition of solutions for the infinite medium. If we consider the source as isotropic, i.e. a spatial and temporal Dirac delta source: $q(\vec{r},t) = \delta^3(\vec{r}-\hat{r}_s)\delta(t)$ at $\hat{r}_s = (0,0,z_s)$, we can find the following expression for the reflectance and transmittance of a slab of thickness s [36]:

$$R(\rho,t) = -\frac{\exp\left(-\frac{\rho^2}{4Dc_mt} - \mu_a c_m t\right)}{2(4\pi D c_m)^{3/2} t^{5/2}} \times \sum_{m=-\infty}^{m=+\infty}\left[z_{3m}\exp\left(-\frac{z_{3m}^2}{4Dc_mt}\right) - z_{4m}\exp\left(-\frac{z_{4m}^2}{4Dc_mt}\right)\right], \tag{1.28}$$

$$T(\rho,t) = -\frac{\exp\left(-\frac{\rho^2}{4Dc_mt} - \mu_a c_m t\right)}{2(4\pi D c_m)^{3/2} t^{5/2}} \times \sum_{m=-\infty}^{m=+\infty}\left[z_{1m}\exp\left(-\frac{z_{1m}^2}{4Dc_mt}\right) - z_{2m}\exp\left(-\frac{z_{2m}^2}{4Dc_mt}\right)\right], \tag{1.29}$$

where:

$$\begin{cases} z_{1m} = (1-2m)\,s - 4mz_e - z_s \\ z_{2m} = (1-2m)\,s - (4m-2)z_e + z_s \\ z_{3m} = -2ms - 4mz_e - z_s \\ z_{4m} = -2ms - (4m-2)z_e + z_s \end{cases} \tag{1.30}$$

with $m = 0, \pm1, \pm2, \cdots$ and $\rho = \sqrt{x^2+y^2}$ (interfiber distance).
Reflectance and transmittance curves represent the power crossing the surface per unit area and at a certain interfiber distance. They can also represent the probability that a photon, entering in the medium at the origin of the coordinate system, exits after a time t and at a distance ρ from the incident point, per unit time and area. Equations 1.28 and 1.29 are infinite series and should be truncated for practical applications. When the distances between the boundary of the sources increases, i.e. if m increases, the contribution of the sources is significant only if ρ or t or both are big.

From equation 1.28 and 1.29 is possible to extrapolate the reflectance curve for a semi-infinite medium, considering $s = +\infty$. In this case: $z_{3m} = -z_s$ and $z_{4m} = 2z_e + z_s$. Only the term for $m = 0$ survive and we obtain the

reflectance equation for a homogeneous semi-infinite medium (TRR):

$$R(\rho,t) = -\frac{\exp\left(-\frac{\rho^2}{4Dc_m t} - \mu_a c_m t\right)}{2(4\pi D c_m)^{3/2} t^{5/2}} \left[z_0 \exp\left(-\frac{z_0^2}{4Dc_m t}\right) - z_p \exp\left(-\frac{z_p^2}{4Dc_m t}\right)\right], \tag{1.31}$$

where: $z_0 = 1/\mu_s^{'}$ and $z_p = z_0 + 2z_e$. In the same way it is possible to calculate the expression for the transmittance. Typically, we employ reflectance measurements because head, arms and legs are not thin enough to allow transmittance measurements. From equation 1.31 is then possible to extrapolate the absolute values of μ_a and $\mu_s^{'}$ as will be explained in paragraph 1.4.1.

1.3.4 Continuous Wave DE solution

Once the time-resolved reflectance has been evaluated, the CW one can easily be obtained by integrating the time-resolved equation. The time integral we obtain is [37, 38]:

$$R_{CW}(\rho,\lambda) = \frac{5 - r_d}{6\pi d^3 (1 - r_d)} \frac{1}{\mu_s'(\lambda)} \left[1 + \rho\sqrt{3\mu_a(\lambda)\,\mu_s'(\lambda)}\right] \times \times \exp\left[-\rho\sqrt{3\mu_a(\lambda)\,\mu_s'(\lambda)}\right], \tag{1.32}$$

where ρ is the distance between the source and the detector and $r_d = -1.44n^{-2} + 0.71n^{-1} + 0.668 + 0.064n$ with reflection indexes of $n = 1.33$ for the experiments on a water-based phantom and $n = 1.4$ for the *in vivo* measurements, and where we have introduced the dependence from the wavelength.

1.4 Extrapolation of the optical properties: absolute values

In this section, how to extrapolate the absolute values of the absorption and scattering coefficient, for both the time-domain and continuous wave approach, will be shown .

1.4.1 TD-NIRS: FIT procedure

Equation 1.31, represents the TD reflectance curve for a homogeneous semi-infinite medium, obtained with the theoretical model. Once we col-

lected the experimental reflectance curves, we have to compare them with the theoretical one, in order to obtain accurate estimation of the optical parameters extrapolated during the measurements. The way to compare them is a least square FIT procedure, where different couples of μ_a and $\mu_s^{'}$ are iteratively tested in order to minimize the following parameter:

$$\chi^2 = \sum_{i=1}^{n} \frac{(R_{teo,i} - R_{\exp,i})^2}{\sigma^2}, \tag{1.33}$$

where σ^2 is the variance, R_{teo} and R_{exp} are respectively the theoretical and experimental expression of the reflectance curve. The interpolation interval (fitting range) includes all the points $> 90\%$ ($> 1\%$) of the peak value for what concern the initial part (final part) of the curve, as shown in figure 1.4. The points relative to the photons that arrive for first at the detectors are to neglect because in that region the radiative transport theory cannot work properly, being a non-random model. Photons on the tail of the reflectance curve are neglected because in that region the values are so low that is not possible to discriminate them from the noise.

The experimental curve doesn't contain information only about the medium but also about the instrument. It's then necessary to subtract the instrument's contribution from the R_{exp} to allow a better estimation of the optical parameters. It is possible to estimate the contribution of the instrument, i.e. instrument response function (IRF), performing a measurement with the injection and the detection fibers one in front of the other. The IRF won't be a δ-dirac, but will have a shape that is typical of each instrument. The IRF can be deconvolved with the experimental data. Since the deconvolu-

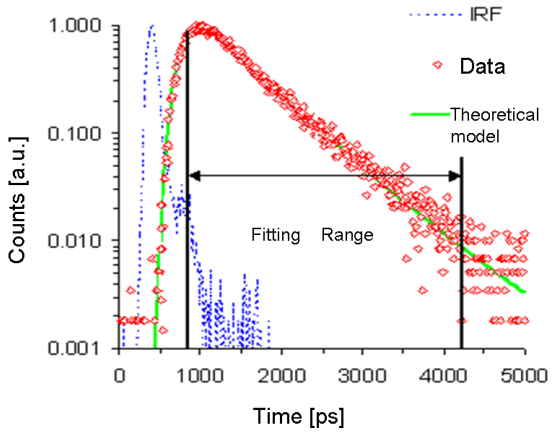

Figure 1.4: Example of FIT process. IRF: blue points. TR data: red points. Convoluted theoretical model: green line.

tion algorithm is more complex than the convolution one, usually the IRF is convolved with the theoretical reflectance curve. The function obtained is the one employed in the least square method [39]. After the determination of the absorption and reduce scattering coefficients is possible to determine the concentration of oxy- and deoxy-hemoglobin, employing equations 1.11.

1.4.2 CW-NIRS

Absolute Values

In equation 1.32, it is evident that $\mu_a(\lambda)$ can be quantitatively calculated if the $\mu_s^{'}(\lambda)$ spectrum is known. A possible way to calculate it and then extrapolate absolute values of the hemodynamic parameters from CW measurements is the one proposed by Rovati et. al. [38]. They suggest, as firstly shown by Wray et al. [40] and Matcher et al. [41], to exploit the absorption of water, taking into account the assumption that the water concentration in human tissues is known with the uncertainty of a few percent [42]. In particular, the spectrum can be obtained combining measurements close to 975 nm, i.e. water absorption peak, with data reported in literature. To clarify this method an example concerning the forearm human muscle is presented. The typical water and hemoglobin absorption coefficients in this region are:

$$\begin{cases} \varepsilon_{O_2Hb}(975\ nm)\ c(O_2Hb) \cong 6.768 \times 10^{-3}\ mm^{-1} \\ \varepsilon_{HHb}(975\ nm)\ c(HHb) \cong 0.79195 \times 10^{-3}\ mm^{-1} \\ \varepsilon_{H_2O}(975\ nm)\ c(H_2O) \cong 36.19 \times 10^{-3}\ mm^{-1} \end{cases}, \tag{1.34}$$

where concentration of water has been assumed to be 78% of the volume, $c(HHb) \cong 20\ \mu M$ and $c(O_2Hb) \cong 60\ \mu M$. From equation 1.34 it's clear that the water absorption at this wavelength is predominant. It's possible to assume that the total absorption in the forearm muscle at 975 nm is due to the water, introducing an error of about the 17%. Therefore, after measuring $R_{CW}(\rho, 975nm)$ we can substitute in equation 1.32: $\mu_a(975\ nm) \cong \varepsilon_{H_2O}(975\ nm)\ c(H_2O)$ and, using an iterative numerical method, it's possible to determine the $\mu_s^{'}$ at this wavelength. In this way we have extrapolated just a point (at λ=975 nm) of the entire scattering spectrum.

To reconstruct the scattering spectrum it's possible to take into consideration data reported by Matcher et al. [43, 44]. They showed that the scattering spectrum decreases with the increasing of the wavelength (from the Mie theory $\mu_s^{'} \propto \lambda^{-b}$); using the slopes ($d\mu_s^{'}/d\lambda$), reported by them, it's possible to calculate the reduced scattering spectrum of water for the tissue under examination and then inverting equation 1.32, it's possible to calculate

the absorption coefficient spectrum. Similar considerations can be applied to other human tissues, e.g. brain, quadriceps.

To determine the concentration of the oxy- and deoxy-hemoglobin we can use equations 1.10 in paragraph 1.1.3. At least three wavelengths are needed, since three cromophores are involved. The resulting equation system is the following one:

$$\begin{bmatrix} \mu_a(\lambda_1) \\ \mu_a(\lambda_2) \\ \mu_a(\lambda_3) \end{bmatrix} \cong \begin{bmatrix} \varepsilon_{O_2Hb}(\lambda_1) & \varepsilon_{HHb}(\lambda_1) & \varepsilon_{H_2O}(\lambda_1) \\ \varepsilon_{O_2Hb}(\lambda_2) & \varepsilon_{HHb}(\lambda_2) & \varepsilon_{H_2O}(\lambda_2) \\ \varepsilon_{O_2Hb}(\lambda_3) & \varepsilon_{HHb}(\lambda_3) & \varepsilon_{H_2O}(\lambda_3) \end{bmatrix} \times \begin{bmatrix} c(O_2Hb) \\ c(HHb) \\ c(H_2O) \end{bmatrix},$$

where λ_1 has to be around 700 nm (oxy-hemoglobin), λ_2 around 830 nm (deoxy-hemoglobin) and λ_3 around 975 nm (water). The solution of this system is achieved by minimizing the least-squares errors. According to the equation 1.12 and 1.13 reported in paragraph 1.2, it's possible to calculate the oxygen saturation (SO_2) and the total hemoglobin concentration (tHb).

Calibration

As already described in paragraph 1.4.1 when we perform a measurement, the experimental reflectance curve, we obtain, carries information not only about the medium under investigation but has also a contribution coming from the instrument. In order to take into consideration this contribution a calibration is necessary. As suggested by Rovati et al. [38] the experimental reflectance curve ($R_{exp}(\rho, \lambda)$) obtained on a phantom of known optical properties, and the theoretical reflectance curve $R_{CW}(\rho, \lambda)$, obtained evaluating equation 1.32 at the panthom's μ_a and $\mu_s^{'}$, differs by a fix percentage. Is then necessary to rescale the curve, fitting the experimental data with the $R_{CW}(\rho, \lambda)$ multiplied by a constant factor K. It's possible to evaluate K as the parameter of the fitting procedure that minimize the reduced χ^2. The calibration constant K is determined on a phantom thus, according to the equation 1.32, must be scaled by a factor η, defined as:

$$\eta = \frac{5 - r_{d,invivo}}{1 - r_{d,phantom}}, \tag{1.35}$$

to obtain the corresponding constant for *in vivo* measurements.

1.5 Heterogeneous media

In the previous paragraphs we treated the biological tissues as homogeneous media. In reality they have a strongly heterogeneous anatomical nature which

can be described as a multilayer structure: scalp, skull and gray and white matter for the head; skin, lipid and muscular fibers for the arms and the legs. Considering the tissues as a multilayer media is an improvement to the model but is not yet enough to obtain a correct description of light propagation because it's often difficult to know exactly which layers compose the tissues and we don't have the necessary knowledge of their optical properties [8]. Is then important the improvement of the depth sensitivity in order to be able to discriminate between upper and deeper layers, being the hemodynamic changes localized mostly in the deeper ones. In the following two paragraphs we present a method to improve the depth sensitivity respectively in the TD and in the CW approach.

1.5.1 Time Domain approach

For each wavelength λ a reference TD-NIRS curve $R_0(t, \lambda)$ is derived, employing an homogeneous model, by averaging the tracks recorded during the initial baseline period of each experiment. Fitting of $R_0(t, \lambda)$ yields the reference absorption value $\mu_{a0}(\lambda)$. Then, at each recording time T during the whole experiment (T=baseline + task + recovery period), changes in the absorption coefficient are derived as:

$$\Delta\mu_a(\lambda; T) = -\frac{1}{c_m \cdot t} ln \left[\frac{R(t; \lambda; T)}{R_0(t; \lambda)} \right], \tag{1.36}$$

where c_m is the speed of light in the medium, t is the arrival time of photons, and $R(t; \lambda; T)$ is the time domain fNIRS curve at the recording time T [45]. To enhance the contribution from deeper layers and to remove possible disturbances caused by superficial layers, we can correct, in the way explained in the following, the previous expression. In literature, it is well known that depth information in TD-NIRS is encoded in the time-of-flight of photons [37, 46]. The early photons are the ones that remain less time inside the tissue and probe, keeping fixed the interfiber distance, the superficial layers, while late photons, the ones that remains more time inside the tissue, have a higher probability to visit deeper layers. Some approaches, where tissues under investigation are modeled as a two-layered semi-infinite medium, with a $\mu_s^{'}$ equal in both layers, were proposed [47, 48]. After the injection of a light pulse and the introduction of an inhomogeneity both in the upper and in the deeper layer, we can write:

$$I\left(t\right) = I_0\left(t\right) \exp\left[-\Delta\mu_a^{UP} L^{UP}(t) - \Delta\mu_a^{INC} L^{INC}(t)\right], \tag{1.37}$$

where $I_0\left(t\right)$ is the time resolved reflectance for the unperturbed medium, $\Delta\mu_a^{UP}$ and $\Delta\mu_a^{INC}$ are the changes of the μ_a in the upper layer and in the

inclusion, and $L^{UP}(t)$ and $L^{INC}(t)$ are respectively the mean-dependent path-lengths (MPL) in the upper layer and in the inclusion [48].

Contini et al. [49] proposed a novel approach, based on the contrast for the early and late part of the TRR function. In the small perturbation regime, equation 1.37 can be written as:

$$I(t) = I_0(t) + \delta I^{UP}(t) + \delta I^{INC}(t), \tag{1.38}$$

where $\delta I^{UP}(t)$ and $\delta I^{INC}(t)$ are the variation of $I_0(t)$, caused respectively by the upper layer and the inclusion inhomogeneity. In this approximation:

$$\begin{cases} \delta I^{UP}(t) = I_0(t) - I_0(t) \exp\left(-\Delta\mu_a^{UP} L^{UP}(t)\right) \\ \delta I^{INC}(t) = I_0(t) - I_0(t) \exp\left(-\Delta\mu_a^{INC} L^{INC}(t)\right). \end{cases} \tag{1.39}$$

Now is possible to introduce the contrast function $C(t)$ defined as:

$$C(t) = \frac{I(t) - I_0(t)}{I_0(t)}. \tag{1.40}$$

Combining equation 1.38, 1.39 and 1.40, we can consider the contrast function as the sum of the contrast caused by the upper inhomogeneity ($C^{UP}(t)$) and the contrast caused by the inclusion ($C^{INC}(t)$):

$$C(t) = \frac{\delta I^{UP}(t)}{I_0(t)} + \frac{\delta I^{INC}(t)}{I_0(t)} = C^{UP}(t) + C^{INC}(t). \tag{1.41}$$

From simulations based on perturbation approach to diffusion theory [47, 50], we can assume that the contrast for a superficial perturbation is the same at both time-gates:

$$C^{UP}(\tau_L) = C^{UP}(\tau_E), \tag{1.42}$$

while for a deep perturbation the contrast at the early time is negligible:

$$C^{INC}(\tau_E) = 0. \tag{1.43}$$

Combining equation 1.41, 1.42 and 1.43 we obtain:

$$\begin{cases} \delta I^{UP}(\tau_L) = \frac{\delta I^{UP}(\tau_E)}{I_0(\tau_E)} I_0(\tau_L) \\ \delta I^{INC}(\tau_E) = 0 \end{cases} \tag{1.44}$$

Combining equation 1.38, 1.39 and 1.44, we obtain the final expression for the $\Delta\mu_a$ for the upper and deeper layers:

$$\begin{cases} \delta\mu_a^{UP} = -\frac{1}{L^{UP}(\tau_E)} \ln\left(\frac{I(\tau_E)}{I_0(\tau_E)}\right) \\ \delta\mu_a^{INC} = -\frac{1}{L^{INC}(\tau_L)} \ln\left(1 + \frac{I(\tau_L)}{I_0(\tau_L)} - \frac{I(\tau_E)}{I_0(\tau_E)}\right) \end{cases} \tag{1.45}$$

Finally, the absorption coefficient is then derived from corrected late gate intensities as:

$$\mu_a(\lambda; T) = \mu_{a0}(\lambda) + \Delta\mu_a(T; \lambda) \tag{1.46}$$

This method allows to improve the depth sensitivity of the time-resolved NIRS measurements. In paragraph 3.1, an experimental evidence of the capability of this method to separate the contributions coming from the upper and deeper layers of the head, will be reported.

1.5.2 Continuos Wave approach

With the CW approach, how to take into account that biological tissues are heterogeneous media is still an open issue. In this paragraph, a method to solve this problem during measurements on muscle, where the superficial layer is typical made off subcutaneous adipose tissue, is presented. Niwayana et al. [51] showed that, during measurements on muscle, the oxygen consumption decreases with the increase of the fat layer thickness. With Monte Carlo simulations they obtained also the mean optical pathlengths in the muscle, which is equivalent to the sensitivity of the measurements. Also this parameter decreases with the increase of the fat layer thickness. A correction curve, which shows the relationship between the thickness of the fat layer and the measurement sensibility for the muscle, can be determined by fitting the curves to the results of Monte Carlo simulations. The relationships between normalized measurement sensitivity S_{muscle}, normalized at 0 mm of the fat thickness, and fat layer thickness h is expressed as:

$$S_{muscle} = exp\left[-\left(\frac{h}{A}\right)^2\right], \tag{1.47}$$

where A is a constant, which depends on the interfiber distance. The fat thickness has to be previously measured by ultrasonography or by means of a skin fold caliper. Once we have calculated the concentration of the hemodynamic parameters, is necessary to divide them by the S_{muscle} factor in order to remove the contribution of the fat layer.

Bibliography

[1] Jobsis F.F., Science 198: 1264, 1977.

[2] http://omlc.ogi.edu/spectra/.

[3] P. Taroni, A. Bassi, D. Comelli, A. Farina, A. Pifferi and R. Cubeddu, J. B. O., 14, 054030, 2009.

[4] A. Kienle and T. Glanzmann, Phys. Med. Biol., 44, 2689-2702, 1999.

[5] P. Taroni, A. Pifferi, A. Torricelli, D. Comelli and R. Cubeddu, Photchem. Photobiol. Sci., 2, 124-129, 2003.

[6] A. Liebert, N. Zolek, R. Maniewski, Phys. Med. Biol., 51, 5737-5751, 2006.

[7] C. F. Bohren and D. R. Huffman, Absorption and Scattering of Light by Small Particles, John Wiley & Sons, New York, 1983.

[8] D. Comelli, A. Bassi, A. Pifferi, P. Taroni, A. Torricelli, R. Cubeddu, F. Martelli and G. Zaccanti, Appl. Opt., 46, 1717-1725, 2007.

[9] A. Torricelli, A. Pifferi, P. Taroni, E. Giambattistelli and R. Cubeddu, Phys. Med. Biol. 46, 2227-2237, 2001.

[10] F. Bevilacqua, D. Piguet, P. Marquet, J. D. Gross, B. J. Tromberg and C. Depeursinge, Appl. Opt., 38, 4939-4950, 1999.

[11] A. Sassaroli, F. Martelli, Y. Tanikawa, K.Tanaka, R. Araki, Y. Onodera and Y. Yamada, Opt. Rev., 7, 420-425, 2000.

[12] F. Orihuela-Espina, D. R. Leff, D. R. C. James, A. W. Darzi and G. Z. Yang, Phys. Med. Biol, 55, 3701-3724, 2010.

[13] M. Wolf, M. Ferrari, and V. Quaresima, J. B. O., 12(6): 062104, 2007.

[14] M. Caffni, D. Contini, R. Re, L. Zucchelli, R. Cubeddu, A. Torricelli, L. Spinelli, In Brain Imaging, ISBN 978-953-307-613-3, InTech - Open Access Publisher, 2011 [In press].

[15] H. Obrig and A. Villringer, J. Cer. Blood Flow & Met., 23:1-18, 2003.

[16] M. Ferrari, M. Muthalib, V. Quaresima, Phil. Trans. R. Soc. A, 369, 114 2011.

[17] T. Hamaoka, K. K. McCully, M. Niwayama and B. Chance, Phil. Trans. R. Soc. A, 369 (1955), 4591-4604, 2011.

[18] F. Martelli, S. Del Bianco, A. Ismaelli, G. Zaccanti, Light propagation through biological tissue and other diffusive media, SPIE, Bellingham, 2010.

[19] M. Cope M., D. T. Delpy, S. Wray, J. S. Wyatt and E. O. Reynolds, Adv Exp Med Biol 248: 33, 1989.

[20] E. O. Reynolds, J. S. Wyatt, D. Azzopardi, D. T. Delpy, E. B. Cady, M. Cope and S. Wray, Br. Med. Bull. 44:1052, 1988.

[21] S. R. Arridge and W. R. B. Lionheart, Opt. Lett., 23:882, 1998.

[22] L. Rovati, A. Bandera, M. Donini, L. Pollonini, IMTC, Instrument and Measurement Technology Conference, Vail, CO, USA, 20-22 May 2003.

[23] A. P. Gibson, J. C. Hebden and S. R. Arridge, Phys. Med. Biol., 50:R1, 2005.

[24] M. A. Franceschini, V. Toronov, M. F. Filiaci, E. Gratton and S. Fantini, Opt. Exp., 6:49, 2000.

[25] B. W. Pogue, S. Giemer, T. McBride, S. Jiang, U. L. Osterberg and K. D. Paulsen, Appl. Opt., 40:588, 2001.

[26] C. D. Kurth and W. S. Tayer, Phys. Med. Biol., 44, 727-740, 1999.

[27] S. L. Jacques S.L., Appl. Opt., 28: 2223, 1989.

[28] M. S. Patterson, B. Chance and C. Wilson, 28 (12), 1989.

[29] D. Contini, Time-resolved functional near infrared spectroscopy for neuroscience, PhD dissertation, 2007.

[30] A. Ishimaru, Wave Propagation and Scattering in random Media, vol. 1, Academic Press, New York, 1978.

[31] M. S. Patterson, B.C. Wilson and D.R. Wyman, Las. Med. Sci., 6, 155, 1991.

[32] L. V. Wang and H. Wu, Biomedical Optics, Principles and Imaging, John Wiley & Sons, New York, 2007.

[33] J. J. Duderstadt and W. R. Martin, Transport Theory, John Wiley & Sons, New York, 1979.

[34] E. Zauderer, Partial differential equations of applied mathematics, John Wiley & Sons, New York, 1989.

[35] R. C. Haskell, L.O. Svaasand, T.T. Tsay, T.C. Feng, M.S. McAdams and B.J. Tromberg, J. Opt. Soc. Am. A, 11, 2727-2741, 1994.

[36] D. Contini, F. Martelli and G. Zaccanti, Applied Optics, 36(19), 4587, 1997.

[37] S. D. Bianco, F. Martelli and G. Zaccanti, Phys. Med. Biol. 47, 4131, 2002.

[38] L. Rovati, L. Pollonini, A. Bandera, M. Donini and G. Salvatori, Rev. Sci. Instr. 75(12),5315, 2004.

[39] A. H. Hielscher, S.L. Jacques, L. Wang and F. K. Tittel, Phys. Med. Biol., 40:1957, 1995.

[40] S. Wray, M. Cope, T. Delpy and E. O. R. Richardson, Biochim. Biophys. Acta, 184, 1988.

[41] S. J. Matcher, M. Cope and D. T. Delpy, Phys. Med. Biol., 38, 177, 1993.

[42] H. Q. Woodward and D. R. White, Br. J. Radiol., 59, 1209, 1986.

[43] S. J. Matcher, P. Kirkpatrick, K. Nahid, M. Cope and D.T. Delpy, Proc. SPIE 2389, 486, 1995.

[44] S. J. Matcher, M. Cope and D. T. Delpy, Appl Opt. 36, 386, 1997.

[45] Y. Nomura, O. Hazeki and M. Tamura, Phys. Med. Biol. 42, 1009-1023, (1997).

[46] J. Steinbrink, H. Wabnitz, H. Obrig, A. Villringer and H. Rinneberg, Phys. Med. Biol., 46, 879-896, 2001.

[47] J. Selb, J. J. Stott, M. A. Franceschini, A. G. Sorensen and D. A. Boas, J. B. O., 10(1), 11013, 2005.

[48] A. Liebert, H. Wabnitz, J. Steinbrink, H. Obrig, M. Moller, R. Macdonald, A. Villringer and H. Rinneberg, Appl. Opt., 43:3037, 2004.

[49] D. Contini, L. Spinelli, A. Torricelli, A. Pifferi, R. Cubeddu, Proc. SPIE Vol. 6629, 662908, 2007.

[50] A. Torricelli, L. Spinelli, R. Cubeddu, F. Martelli, S. Del Bianco and G. Zaccanti, Phys. Rev. Lett., 95, 078101, 2005.

[51] M. Niwayama, L. Lin, J. Shao, N. Kudo and K. Yamamoto, Rev. Sci. Instr. 71(12), 4571, 2000.

CHAPTER 2

A compact Time-Resolved system for NIR spectroscopy based on wavelength space multiplexing

In section 2.1 the development of our system, based on a new modality to inject light into the tissue: the wavelength space multiplexing (SM), is presented. In particular we will describe the SM approach in paragraph 2.1.1, and the system setup in paragraph 2.1.2. The instrument characterization on tissue phantoms and preliminary in vivo measurements during a standard cuff occlusion and a motor cortex response are respectively described in paragraph 2.2.1 and 2.2.2. Finally, in paragraph 2.3, a comparison between the SM and the wavelength time multiplexing (TM) approaches is presented. After the development of this instrument we worked on the improvement of some instrument features and on the increasing of the channels number maintaining an SM configuration, as explained in section 2.4.

2.1 SYSTEM SETUP

2.1.1 The wavelength space multiplexing approach

Typically, systems based on time-resolved NIRS use a TM approach to inject light at two different wavelengths into the tissue. As shown in Fig. 2.1(a), the optical pulses at different wavelengths are delayed, one with respect to the other, by means of an optical fiber delayer line and mixed by means of an optical coupler [1] or a fiber optical splitter [2, 3, 4], which halves the intensity of the pulses. In this way, it is possible to time-multiplex the wavelengths which are both acquired in the same temporal window. The

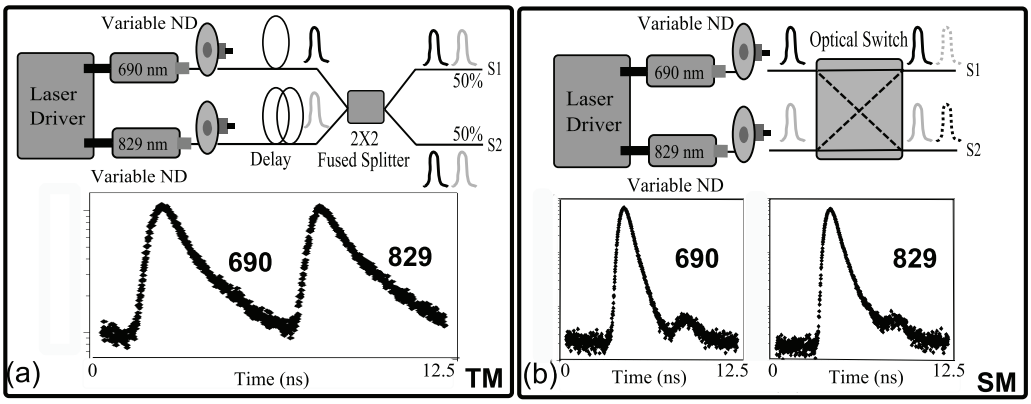

Figure 2.1: Comparison between the two different injection approaches and how the acquired curves appear in a temporal window. (a) TM, (b) SM.

information carried by the curves is acquired simultaneously in time, but problems of cross-talk between pulses might hamper the overall performances of the system. Cross-talk could be due to the superposition of the photon distributions time-of-flight (DTOFs). Nonlinearity in the time-to-amplitude converter might also reduce the available time-interval in the time correlated single photon counting (TCSPC) apparatus. In case of large source detector distance and/or low absorption coefficient, the DTOFs are rather broad and this could result in a partial overlapping of the DTOFs themselves. Another source of cross-talk mights arise from significant changes in the counts at one wavelength, in particular when the count rate is high and when in the system a routing electronics is used to manage signals coming from different detectors. In these cases, it is necessary to keep the count rate low with an overall reduction of the performances.

To avoid wavelength cross-talk and to increase signal-to-noise ratio, we have introduced a new approach to inject and collect light into the tissue based on wavelength SM (Fig. 2.1 (b)). The two wavelengths are injected alternatively into the two channels by means of an optical 2X2 switch. In this way, we acquire in each detection line and in each temporal window only one DTOF at one wavelength at a time. Using this new approach is possible to exploit the full temporal and dynamic range of the acquisition TCSPC boards. Due to the fact that the wavelengths are not simultaneously measured at the same point, the switching rate must be sufficiently high to follow the hemodynamic changes in the tissue under examination (e.g. for the brain 5 Hz sampling rate can be enough).

2.1.2 System description

In Fig. 2.2, a complete scheme of the instrument setup is reported. As light sources, a couple of pulsed diode lasers, working in gain switching modality, operating at 690 and 829 nm with 80 MHz repetition rate (PDL, Picoquant GmbH, Germany) is used. After the laser heads, light is injected into multimode graded index fibers (50/125 μm by means of a custom-made coupler. It combines a couple of neutral density attenuators (NT43-770, Edmund Optics GmbH, Germany), with a total variable attenuation in the range of 0-80 dB, and a standard fiber optics coupler. Variable attenuators are needed during measurements on biological tissues to equalize the signal of the two wavelengths or during the acquisition of the instrument response function (IRF) to avoid damages of the detectors. The attenuators are automatically controlled by stepper motors (440-436, RS Components, Italy). After the attenuation stage, light passes through an optical 2X2 switch (LEONI Fiber Optics GmbH, Germany, maximum switching rate: 5

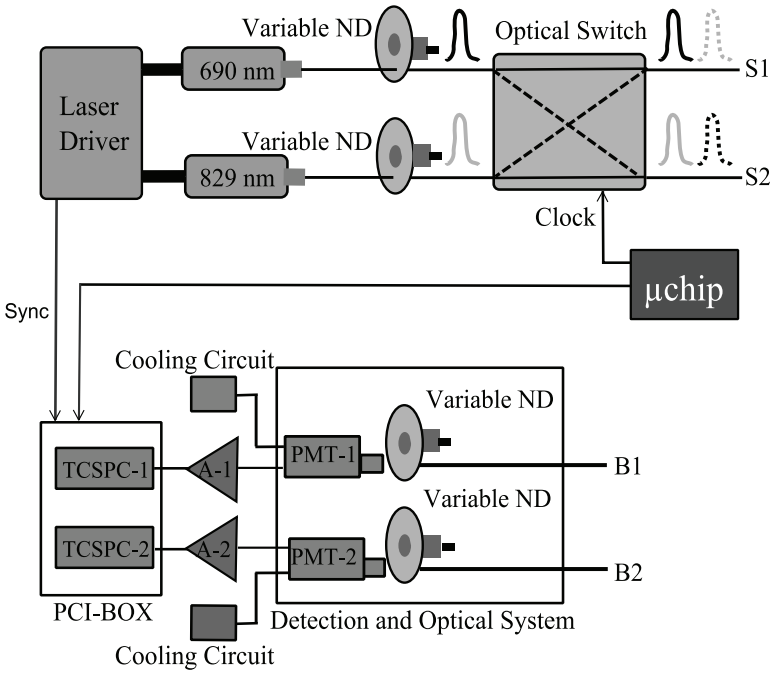

Figure 2.2: Overview of the entire system. ND: neutral density attenuator; S: injection fiber; B: collection bundle; PMT: photomultiplier tube; A: amplifier; TCSPC: time correlated single photon counting board; μchip: micro-controller unit; and Sync: synchronization signal.

ms), which allows the wavelength SM.

Photons re-emitted by the sample are collected by two custom-made glass fiber optic bundles (Loptek Glasfasertechnick GmbH, Germany) with 3 mm diameter and 0.49 numerical aperture. After the bundles, the signal is equalized by variable neutral density attenuators (like in the acquisition section). Then, the signal is coupled to the active area of a photomultiplier tube (PMT) (PMC-100, Becker&Hickl, Germany) by means of a proper optical lens system. This is composed of two aspherical lenses with a focal lengths of 18.75 and 25 mm, respectively (NT-47-729/730, Edmund Optics Gmbh, Germany), arranged inside a C-mount tube. This configuration allows to reach a coupling efficiency of 96%, keeping the dimensions of the entire optical system around 52 mm (from bundle to the active area of the PMT). The PMTs are cooled by an internal Peltier system driven by external home-made circuits. After the PMTs, the electrical signals are amplified (HAFC-26, Becker&Hickl, Germany).

The acquisition of time-resolved reflectance curves is accomplished by two parallel and identical boards (SPC130, Becker&Hickl, Germany) for TCSPC [5]. They are placed in a PCI-box (PCI-Cardbox 2F, IBP Instruments Gmbh, Germany) interfaced with a laptop and have a useful count rate of 4 MHz each. The maximum count rate and the commutation time of the optical switch (5 ms) impose a minimum in the acquisition time of about 10 ms to have a reliable (about $2 \cdot 10^4$ counts per curve) measurement.

All the system is controlled by a home-made software, written in C-language in the LabWindows/CVI environment (National Instruments, Austin, TX), interfaced to a micro-controller unit (dsPIC30F2010, Microchip Technology, Inc., Chandler, AZ). The micro-controller unit receives, through a serial communication, the setting parameters from the laptop and provides a trigger signal to synchronize the optical switch and the data acquisition of the TCSPC boards. The system is also provided by suitable probes (made of Velcro stripes and custom-made plastic holders) for positioning of the injection fibers and of the collection bundles on the tissue.

In Fig. 2.3, a typical instrument response function (IRF, black points) and a DTOF curve (open symbols) at 690 nm are shown. The full width at half maximum (FWHM) of the IRF is approximately 570 ps. Similar characteristics were observed for the other wavelength.

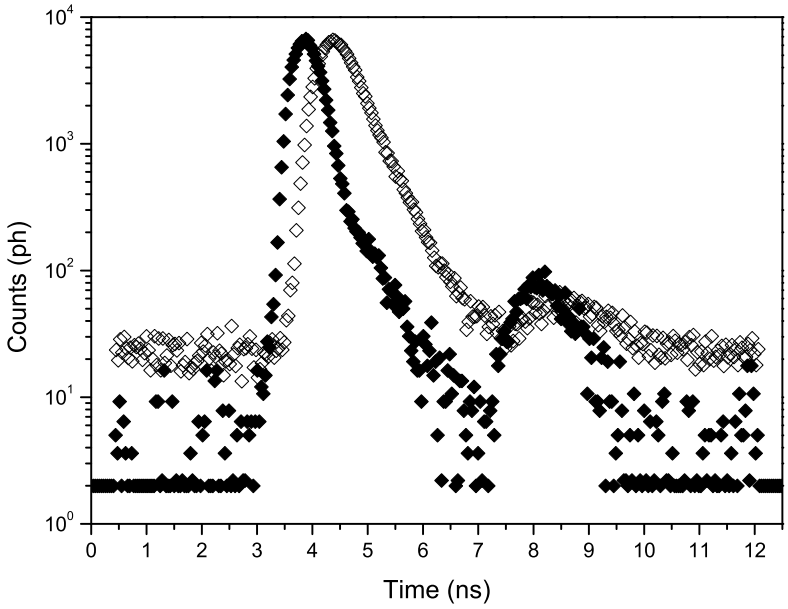

Figure 2.3: Example of the instrument response function (black points) and of a time-resolved reflectance curve (open symbols) at 690 nm.

2.2 SYSTEM CHARACTERIZATION

2.2.1 Medphot protocol

A standard characterization protocol was employed to evaluate the system's performances in terms of measurement results and to make it comparable with other photon migration instruments. The applied protocol, developed within the framework of the European thematic Network Medphot [6], schedules to measure a set of 32 solid phantoms based on epoxy resin with TiO_2 powder as the scatterer and black toner as the absorber. Each phantom has a label composed of a letter (A-D) and a number (1-8) representing, respectively the nominal reduced scattering (5-20 cm^{-1}, 5 cm^{-1} step) and the nominal absorption (0-0.49 cm^{-1}, 0.07 cm^{-1} step) coefficients at 660 nm. A simultaneous estimate of reduced scattering coefficient and absorption coefficient for each source-detector couple was achieved by best fitting of DTOFs with a standard model of diffusion theory, as described in paragraph 1.4.1.

Linearity of μ_a and $\mu_s^{'}$

Reflectance measurements on all the phantoms and for all the injection and detection lines were performed with an interfiber distance of 2 cm. Time-resolved reflectance curves with about 1.5×10^6 counts (acquisition time: 1 s for each wavelength) were acquired. The results, shown in Figs. 2.4 and 2.5, refer to only one injection-detection line at, respectively, the two different wavelengths of 690 and 829 nm. The points represent the average over 10 repeated measurements on each phantom, the bars on the respective standard deviations.

In Figs. 2.4 (a) and 2.4 (d), the measured absorption (reduced scattering) versus the conventional true absorption (reduced scattering) coefficients are respectively plotted. The solid line in Fig. 2.4 (a) represents the best fit of the first four points obtained averaging over the different phantoms. The solid line in Fig. 2.4 (d) was obtained with the same principle but fitting on the last three points. We chose these fitting points since the diffusion theory works properly in the range of low absorption and high reduced scattering values.

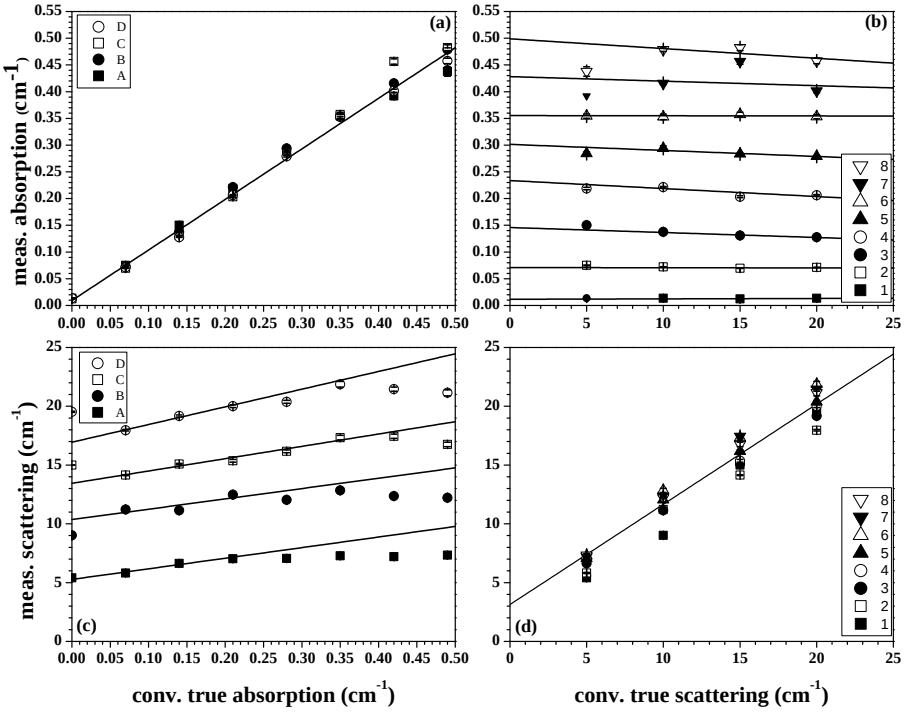

Figure 2.4: Linearity for the absorption and reduced scattering coefficients at 690 nm. The black bars represent the standard deviation among 10 different acquisitions.

The experimental points, for both the coefficients, are well aligned along this line and not much dispersed around it, suggesting a good linearity of the instrument. In Figs. 2.4 (b) and 2.4 (c), the measured absorption (reduced scattering) versus the true reduced scattering (absorption) coefficients are respectively plotted. The solid lines represent the best fit of the second, third, and fourth point for the same reasons explained before [in Fig. 2.4 (c), it is not considered the first point]. Where the solid lines are not horizontal, there is a coupling between the optical parameters. It happens for high value of the two coefficients, as expected from the validity of the diffusion model [7]. This behavior does not cause us problems; in fact, typical values for the two optical coefficients of the biological media are about μ_a=0.14 cm^{-1} and $\mu_s^{'}$=10 cm^{-1} (phantom B3), and in this range we observe no coupling between the optical coefficients and good linearity.

Similar results were found for data at 829 nm, as shown in Fig. 2.5. As expected from the absorption and scattering spectra of the phantoms, the points are shifted toward lower absolute values, even if they preserve the characteristics of linearity showed for the data at 690 nm.

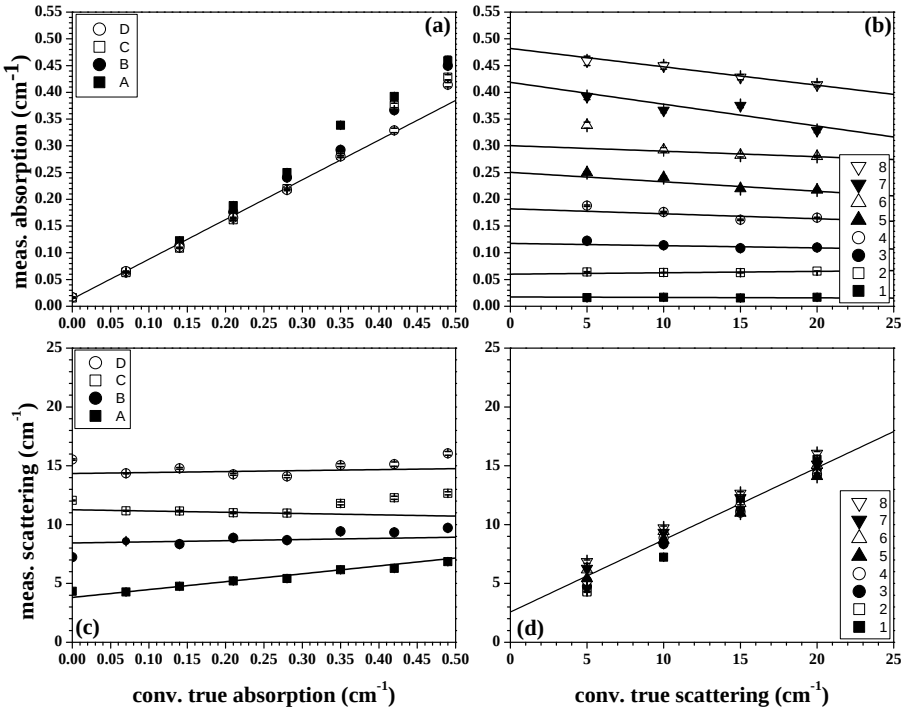

Figure 2.5: Linearity for the absorption and reduced scattering coefficients at 829 nm. The black bars represent the standard deviation.

Noise

Noise test allows to estimate the required number of counts of the DTOF curve in order to have limited variability of the measurement results due to random effects. In Fig. 2.6, the coefficient of variation (CV) for the absorption and reduced scattering coefficient at 690 nm [Fig. 2.6 (a)] and 829 nm [Fig. 2.6 (b)] is shown. We need more than 5×10^5 (7×10^5) counts for the scattering at 690 nm (absorption at 690 and 829 nm, scattering at 829 nm) to have a CV lower than 1%. This is a typical CV value to perform measurements with acceptable precision. Normally, during an *in vivo* experiment, a collection time of about 200 ms is sufficient to acquire a curve of about 5×10^5 photons. The solid line is a linear fit of the CV as function of photons counts N, which has a trend very close to the one indicated by the photon noise statistics [8]. Indeed, we found a power law dependence: CV$\div$N^n, where coefficient n=-0.54 (n=-0.54) for absorption at 690 nm (829 nm) and n=-0.57 (n=-0.49) for reduced scattering at 690 nm (829 nm). We note that the last points, relative to the largest counts, refer to a small number of curves to represent a realistic statistics.

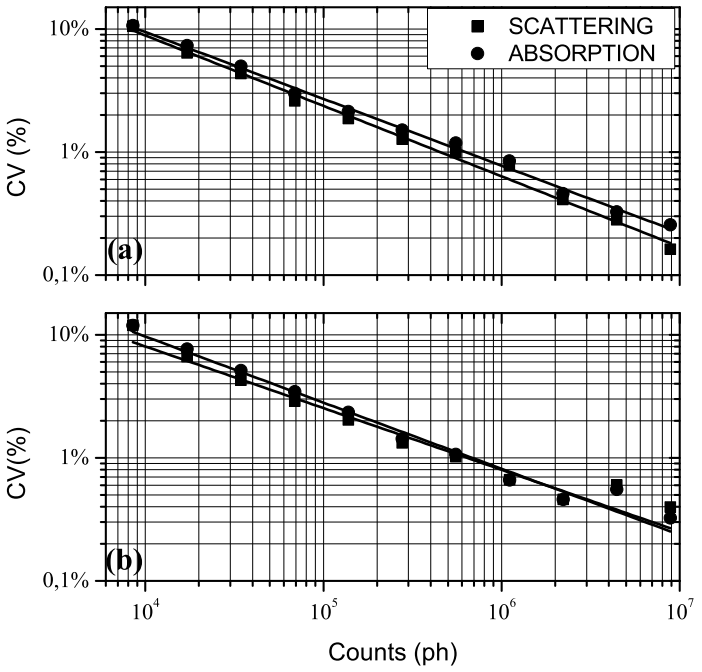

Figure 2.6: CV for the absorption and reduced scattering coefficients. The solid lines are the linear fit of CV. (a) CV at 690 nm. (b) CV at 829 nm.

Stability

The measurements were performed in a reflectance geometry, on phantom B3, with an interfiber distance of 2 cm and an acquisition time of 2 s (1 s for each wavelength), for a total of 300 min. In Figs. 2.7 (a) and 2.7 (b), the results of the stability test are expressed as percentage variations with respect to the average value, over the last 30 min, of the absorption coefficient, respectively, at 690 and 829 nm for one injection-detection line. To reach a stability level of ±3% (±1%) of the average value, the system takes about 24 min (78 min) being this the warm-up time of laser heads.

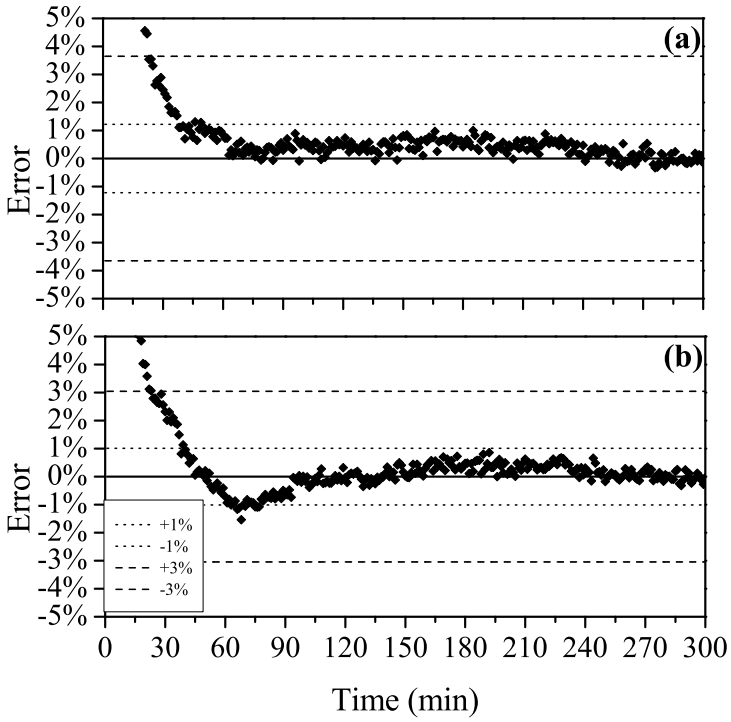

Figure 2.7: Stability test: percentage variations with respect of the average value of the absorption coefficient at (a) 690 nm and (b) 829 nm.

Reproducibility

We performed the same measurements in the same experimental conditions (reflectance geometry, 2 cm interfiber distance, 1 s acquisition time, phantom B3) in three different days to evaluate the reproducibility. We calculated the displacement of the measured optical parameters obtained at

each day with respect to the value found averaging the values over the days. We found, for one injection-detection line, a displacement of about 8% (7%) for the absorption (reduced scattering) coefficient at 690 nm; at 829 nm, we obtained 6% for both the optical coefficients.

2.2.2 Preliminary in vivo measurements

We performed preliminary tests to check the performances of our instrument during in vivo measurements aiming at monitoring the hemodynamic changes during muscle cuff occlusion and brain activation. Taking the assumption that deoxy-hemoglobin and oxy-hemoglobin (HHb and O_2Hb, respectively) are the main chromophores contributing to absorption, their concentrations are easily derived by using the knowledge of the extinction coefficient [9]. To enhance the contribution from deep layers and to remove possible disturbances caused by superficial adipose layers, a correction method based on the use of late time windows (1750-2500 ps) was also applied, see paragraph 1.5.1.

Cuff occlusion on the arm muscle

A standard arterial cuff occlusion of the arm muscle on a male adult volunteer was performed. The measurement protocol scheduled an arterial occlusion (180 mm Hg, left arm) consisting of 1 min of baseline, 2 min of task, and 3 min of recovery, for a total of 6 registration minutes. The measurements were performed in a reflectance geometry, with a sample acquisition rate of 400 ms (200 ms for each wavelength) and an interfiber distance of 2 cm. We put on the medial aspect of each arm, one injection fiber and one detection bundle by means of a black rubber pad connected to brand fasteners (ONE-WRAP®, Velcro Italia Srl, Italy). They guarantee a good adhesion of the fiber to the skin also in the event of movements of the subject.

In Fig. 2.8 (a), the time courses for the variations of HHb and O_2Hb on both the arms, calculated as difference with the average values over the first 30 s of the baseline period, are shown. During the arterial occlusion, the flow of the deoxygenated blood through the veins and the influx of the oxygenated one through the artery are inhibited. In fact, we observe an increase of the HHb and a decrease of O_2Hb during the entire occlusion task. On the right arm, relevant variations of the hemodynamic parameters are not present, as expected. When the cuff is released (slow release, in a few seconds, to avoid abrupt changes), we observe a return to the baseline value with the presence of oscillations (i.e., undershoot for HHb and overshoot for O_2Hb). We notice a delay in the response of HHb compared to O_2Hb, as expected, since the

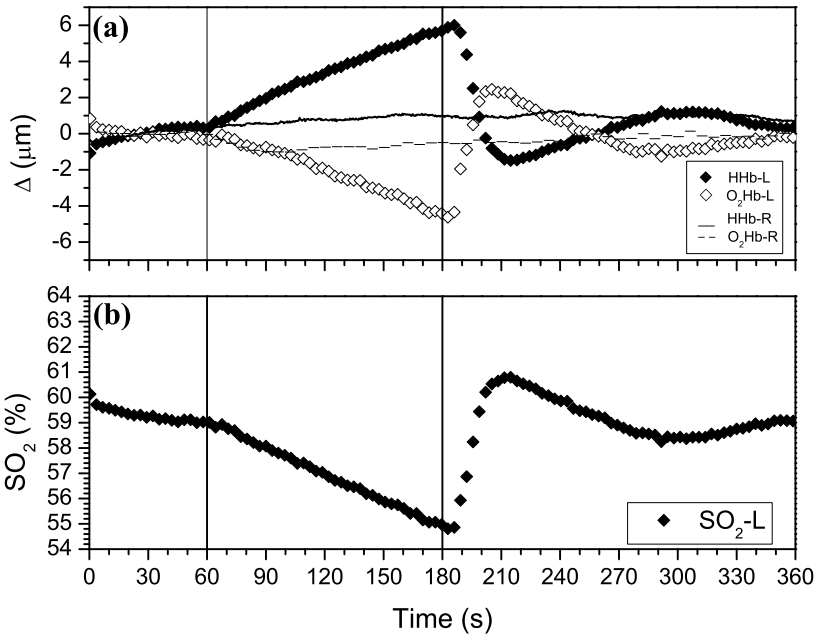

Figure 2.8: Arterial occlusion on the left arm. (a) Changes in HHb (ΔHHb) and O_2Hb (ΔO_2Hb) on the left (l) and right (r) arm. (b) Time course of the absolute value of the saturation coefficient (SO_2%).

veins are released after the arteries, this effect being enhanced by the slow release of the cuff.

One of the advantages of time-resolved technique is the possibility to extract not only the relative variations, but also the absolute values of the optical parameters. This can be exploited to estimate, as example, the time courses of blood oxygen saturation [SO_2=O_2Hb/ (O_2Hb+HHb)]. In Fig. 2.8 (b), SO_2 measured during the arterial occlusion on the left arm is shown. During baseline, SO_2 is around 60%, a typical value for human muscle [3, 11], while a decrease till about the 55% is observed during the arterial occlusion period.

Motor cortex response during hand movements

We employed our instrument also during an *in vivo* test on an adult volunteer to study the hemodynamic response of the motor cortex during the movement of the right hand. The injection and detection fibers were arranged on the scalp over the focal point for hand movement (optodes centered across the C3 and C4 positions, as defined by the 10/20 EEG International System) with an interfiber distance of 2 cm. The measurement protocol consisted of

10 s of baseline, 20 s of motor task (opening and closing right hand), and 10 s of recovery. An acquisition time of 1 s (0.5 s for each wavelength) was used. The protocol was repeated 15 times, and the results were averaged.

In Fig. 2.9, changes in HHb (ΔHHb) and O_2Hb (ΔO_2Hb) during the measurements are plotted. The graph in Fig. 2.9 (a) shows the results for the left hemisphere. Here, it is evident that the increasing of O_2Hb and the corresponding decreasing of HHb during the motor task, as expected, by the contralateral brain activation. The graph in Fig. 2.9 (b) refers to the right hemisphere, where there are not significant task related changes during the experiment, as expected.

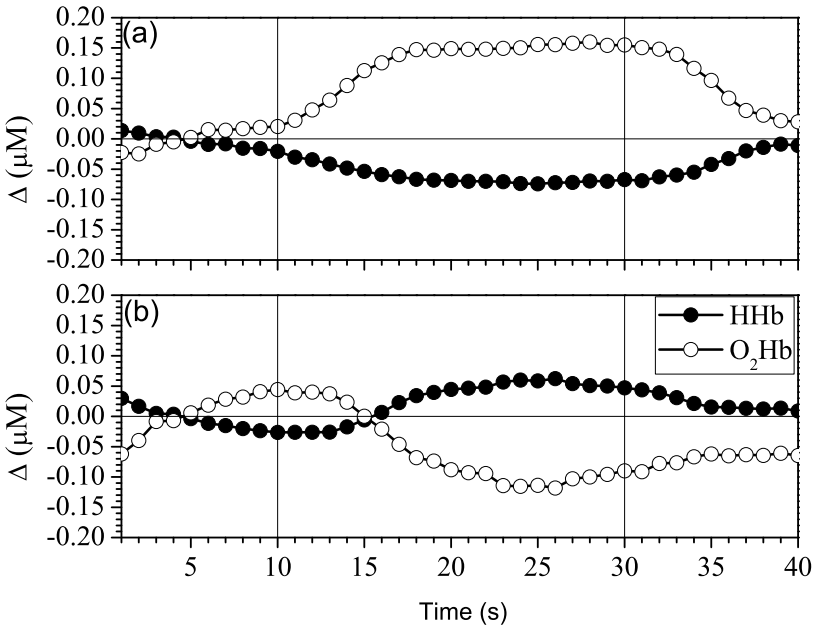

Figure 2.9: Changes in HHb (ΔHHb) and O_2Hb (ΔO_2Hb) during right hand movements. (a) Left hemisphere. (b) Right hemisphere.

2.3 WAVELENGTH SPACE MULTIPLEXING AND TIME MULTIPLEXING APPROACH: A COMPARISON

To quantify the cross-talk between the wavelengths, we have compared the two different approaches to inject light into the tissue in three different configurations: SM, TM in a dual-channel system, and time multiplexing in a system with more detection channels, where a routing electronics is introduced, time multiplexing with router (TMR). We have done measurements keeping one wavelength (λ_F) at a fixed count rate (four different values: 10^5, 5×10^5, 10^6, 1.5×10^6 photons/s) and varying the count rate at the other wavelength (λ_V) (nine values: $\pm75\%$, $\pm50\%$, $\pm25\%$, $\pm10\%$, and 0% of the constant value). Figure 2.10 shows the case for λ_F=690 nm and λ_V =829 nm. In principle, varying the intensity of λ_V, we should not observe a variation in the amount of the count rate at λ_F and the points in Fig. 2.10 should be horizontals. This is what happens when the count rates are low (λ_F at 10^5 counts/s) [Fig. 2.10(a)]. By increasing the value of the counts at λ_F [Figs. 2.10(b)-10(d)], the SM configuration shows the absence of cross-talk

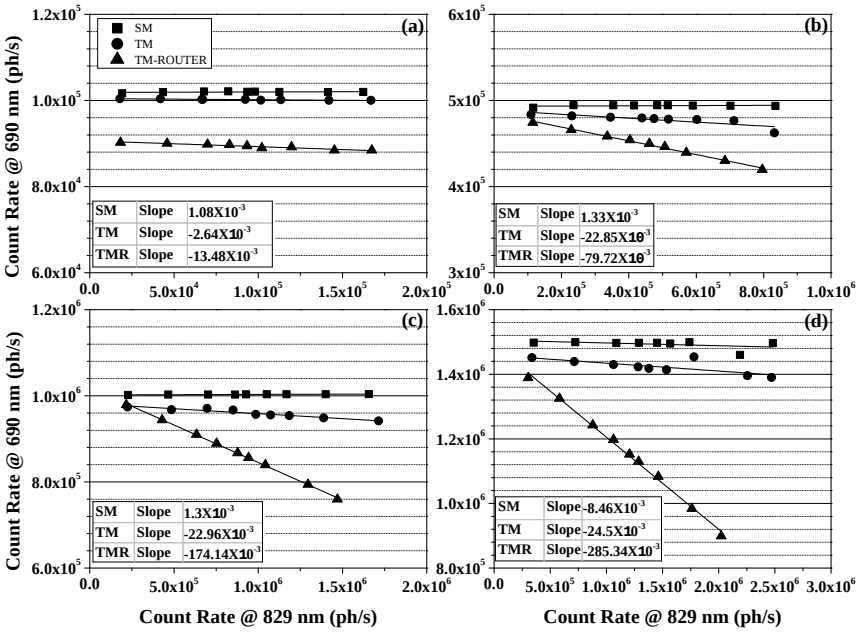

Figure 2.10: Trend of the count rate at 690 nm when it is kept fixed at different values and the count rate at 829 nm is varied. Fixed values: (a) 10^5 photons/s, (b) 5×10^5 photons/s, (c) 10^6 photons/s, and (d) 1.5×10^6 photons/s. The results are shown for three different configurations: SM, TM, and TMR. The solid lines are the linear fit.

between the wavelengths, as expected, since the two curves relative to the two different wavelengths are acquired in two different temporal windows (see linear fit and solid lines). To quantify the cross-talk, a linear regression of the points for each configuration has been performed. The slope parameter (dimensionless) represents the relative change in the acquired photons count rate at λ_F with respect to the acquired photon count rate at λ_V. The slope of the linear fit increases in the TMR configuration already from the second value [Fig. 2.10(b)]. This behavior is not present in the TM configuration, which has a trend similar to the SM one. This suggests that a routing electronics introduces a saturation threshold, which limits the photons count rate in each temporal window. Therefore, when the number of channels is large, a tradeoff between the number of channels (quality of the imaging) and the count rate (quality of the signal-to-noise ratio) is required.

Then, we have evaluated the effect of the cross-talk on the estimation of the absolute values of the optical parameters. In Fig. 2.11, we plotted the dependence of the scattering coefficients at 829 nm at different values of λ_V. When the count rate at λ_F is low, the slopes of the linear fit (solid line) are

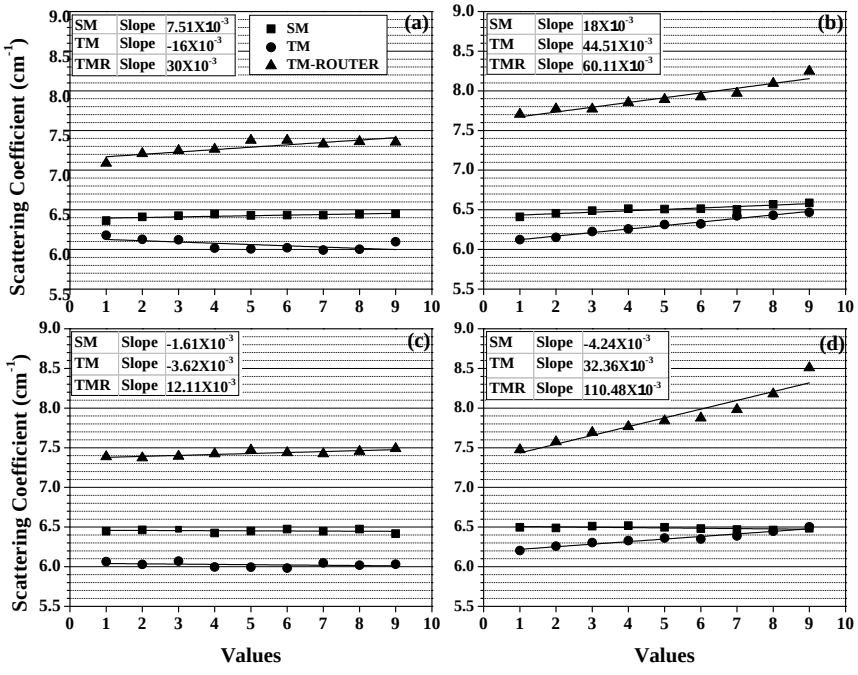

Figure 2.11: Scattering coefficients at 829 nm. First row: λ_F=690 nm and λ_V=829 nm; second row: λ_F=829 nm and λ_V=690 nm. First column: fixed value of 10^5 photons/s; second column: fixed value of 1.5×10^6 photons/s. The solid lines are the linear fit.

small, in fact line are almost horizontals, for all the three different configurations, as shown in Figs. 2.11 (a) and 2.11 (c). When the count rate at λ_F is 1.5×10^6 photons/s, the slopes become higher for the TM configuration and much higher for the TMR configuration. This shows that keeping a high count rate at λ_F and varying it at λ_V, an error in the determination of the absolute values of the scattering coefficient is introduced.

The main reason for this behavior is the partial overlap of the DTOFs (and of possible reflections in the optical system) at the two different wavelengths in the TM and TMR configurations. This could be avoided by reducing the frequency repetition rate. However, not all laser sources can operate at different repetition rates. Furthermore, reducing the repetition rate will not eliminate the cross-talk due to the acquisition of more DTOFs in a single TCSPC window. This behavior is not present in the SM configuration, which exploits the entire TCSPC window for one DTOF at one wavelength at a time. Similar results were obtained for the scattering coefficients at 690 nm and for the absorption coefficients at both wavelengths.

2.4 SYSTEM IMPROVEMENTS

Even if the instrument characterization (paragraph 2.2) shows good results in terms of linearity, stability, noise and reproducibility, some other characterizations and improvements were necessary in order to further improve the instrument efficiency. In particular, we look into the ideal count rate during the measurements, the switch performances, a way to reduce the power losses, how to overcome some heating problems and the best way to take measurements to extrapolate value of μ_a and $\mu_s^{'}$. Then we increased the number of injection and detection channels, transforming the 2×2 prototype in a multichannel 16×4 instrument.

2.4.1 Determination of Maximum Count Rate

We wanted to determine the maximum count rate that we can set during the measurements in order to remain in single photon statistics and to avoid the acquisition board saturation (about 4-5 MHz). The TCSPC boards can detect only one photon per signal period. If the detection rate is so high that the detection of a second photon within the recorded time interval becomes likely, the waveform is distorted (pile-up effect), and this is reflected in a bad extrapolation of the optical properties of the sample during the fit process, explained in paragraph 1.4.1. During the data analysis, in fact, a different shape in the reflectance curve means a different absorption or scattering coefficients. At this purpose, we took measurements on phantom B3 (μ_a=0.14 cm^{-1}; $\mu_s^{'}$=10 cm^{-1}) at different count rates, in a range between 500 Kcounts and 6000 Kcounts (500 Kcounts steps), with an interfiber distance of 2 cm.

In figure 2.12 the values of the reduced scattering at 690 nm, relative to PMT1 and source number 2, are shown. The values found for $\mu_s^{'}$ during the first measurements, where the count rate is low, are pretty close to the real one. In the inset of figure 2.12 are reported some percentage values that represent how much the scattering coefficients found, differ from the right one. They are calculated as the difference between the value found and the average among the values referring to the first four counts levels, divided by the average itself. Increasing the count rate, we observe a progressive overestimation of the $\mu_s^{'}$ value. This is due to the fact that the board is reaching its saturation limit and we're going towards the limit of the single photon statistics. From the graph and the inset, it's clear that we have to fix a maximum count rate around 3 millions of counts to be able to extrapolate reasonable values (+ 1.9%). Similar results were found for the absorption coefficient.

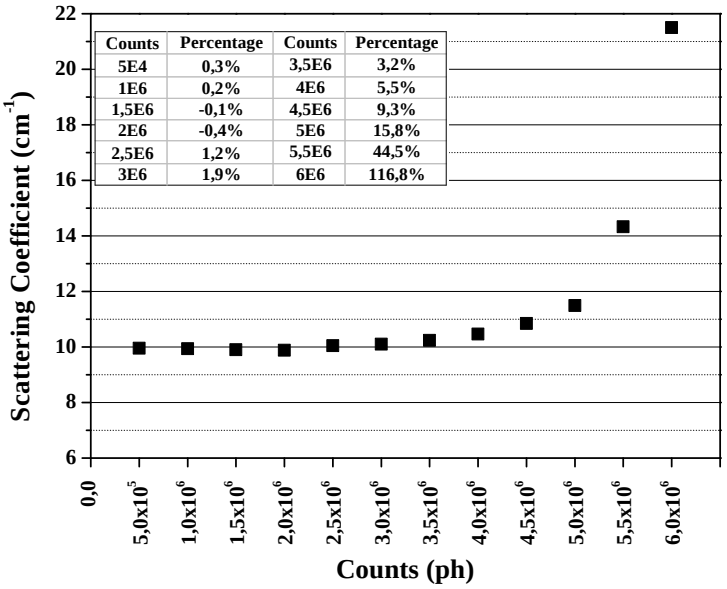

Figure 2.12: Scattering coefficient, at 690 nm, at different count rates.

2.4.2 Switch Characterization

A specific fiber optical switch characterization was done, to better understand its behavior and set a maximum switching frequency threshold, if necessary. The accuracy of the switching time is, in fact, very important in order to implement the space wavelength multiplexing without losing the information regarding which wavelength is in one channel at a certain measurement time. The minimum switching time certified by the builder is 5 ms. If the acquisition boards saturation is about 4 MHz, it means that it's possible to have 4 millions of counts per each second. To be able to extrapolate the optical parameters, during the analysis procedure, about 20 Kcounts per curve are necessary, this implies that each measurement has to be at least 5 ms. In the SM modality, to have a complete acquisition, 4 steps are necessary: 1) switch movement towards the "parallel" position (5 ms), 2) acquisition ($\geq$ 5 ms) 3) switch movement towards the "crossed" position (5 ms) 4) acquisition ($\geq$ 5 ms), for a total of at least 20 ms each measurement, 10 ms each wavelength.

We characterized the optical switch at different switching time (0.02, 0.025, 0.03, 0.04, 0.05, 0.1, 0.25, 0.5 and 1 s). We performed measurements on phantom TC (μ_a=0.14 cm^{-1}, $\mu_s^{'}$=10 cm^{-1}), with an interfiber distance of 2 cm and fixed acquisition counts at 100 Kcounts/s. If the switch behavior was the same, operating at different switching rate, we should always obtain the same counts; we found a different result instead. In graph 2.13 the nor-

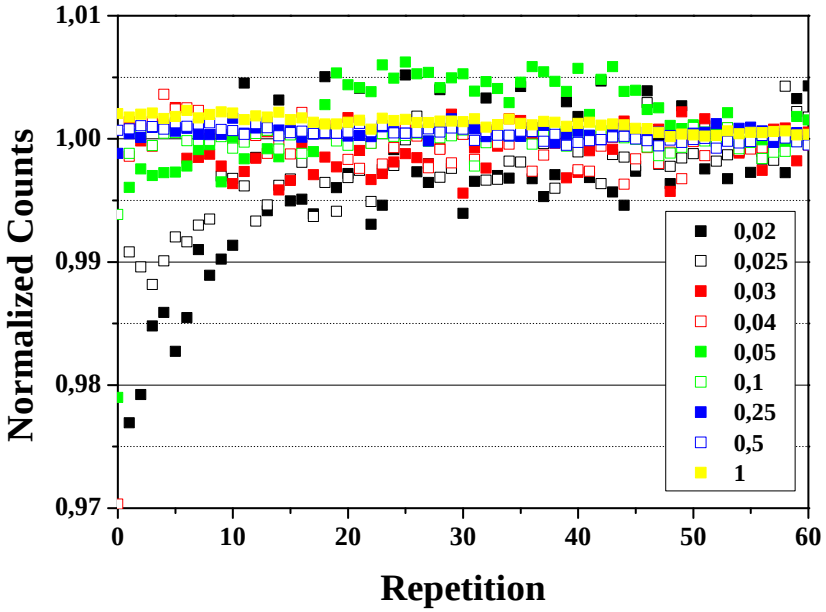

Figure 2.13: Normalized counts (@ 690 nm) registered in function of the switch repetitions, at different switching rates (see legend).

malized counts at different switching rate (see legend) are shown. They are obtained dividing the counts by the average of the last fifty points. When the switching rate is fast, there is an error in the measure, and the counts are underestimated. Only after some repeated movements, the switch starts to work at full. This is probably due to an inertia of some mechanical components or to the time that the piezoelectric actuator needs to move the fibers. As the switching rate becomes slower (from 0.02 to 1 s), the error is lower. To overcome this problem is enough to wait for the switch to perform some movements before starting to save the measurements.

Typically it's simpler to think about the time that we need to wait before saving, instead of the number of movements. In graph 2.14 the same result in function of time is presented. It's easy to see that, with the fastest switching rate, it's necessary to wait about 2 seconds before recording the right amount of counts. This procedure is necessary only once, at the beginning of a measurement, and does not introduce further delays. To solve this problem was enough to modify the micro-controller program so that the recordings start 2 seconds after the beginning of the switch movements.

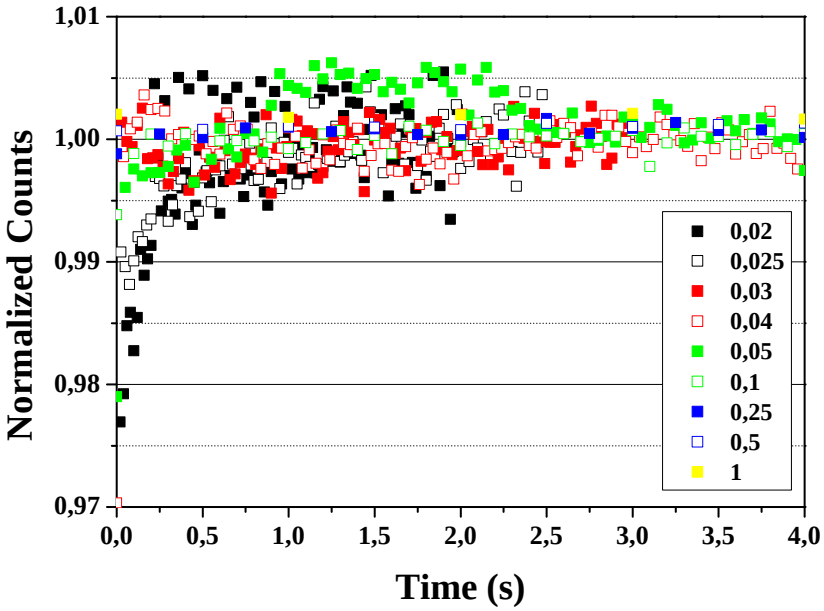

Figure 2.14: Normalized counts (@ 690 nm) in function of time, at different switching rates (see legend).

2.4.3 Effects of the attenuation on IRF

During the instrument characterization, we found some problems in extrapolating the right optical parameters in phantom with high absorption and reduced scattering coefficient. It can be due, of course, to the limit of the diffusion model, which doesn't work properly at those values (see chapter 1). But the error made during the computation was not always constant, but it changed in some different measurements, where the only difference was how the IRF was recorded. Typically the measurement is done with an attenuation in front of the PMTs, provided by the variable circular attenuators, in order to obtain the amount of counts required. When we have to record the IRF, we remove the sample and we place the injection and the detection fibers directly one in front of the other. For this reason it's necessary to increase the attenuation in front of the PMTs.

We tested the way to take the measurements and the IRF in terms of attenuation, doing some trials on phantom B3 (μ_a=0.14 cm^{-1}, $\mu_s^{'}$= 10 cm^{-1}) and B5 (μ_a=0.28 cm^{-1}, $\mu_s^{'}$= 10 cm^{-1}). We kept fix the counts under the principal peak at 500 Kcounts and we varied the attenuation of the variable attenuators in front of the PMTs from 45° to 315°, 45° of step. It corresponds to a variation from about 1.66 to 0, 0.33 of step, in terms of optical density (OD). After that we took the IRF with the same procedure. In graph

2.15(a), the reduced scattering coefficient at 690 nm, found for B3 phantom, is shown; in figure 2.15(b), for phantom B5. These values are extrapolated analyzing data with all the combination between PMTs attenuation during the IRF (x-axis) and PMTs attenuation during the phantom measurements (see legend). As shown in figure 2.15(a) the computed scattering coefficient is always close to its real value for phantom B3; the same doesn't happen on phantom B5 (Figure 2.15(b)). In this case, fitting data coming from measurements and IRF with different attenuations, we obtained values for the reduce scattering coefficient completely different, with an error, which can reach 5 cm^{-1} (50%). Similar results were found for both the wavelengths, for phantoms with higher absorption and scattering coefficients and for both the optical coefficients. This means that different attenuations during measurements and IRF acquisition cause differences in the extrapolation of the optical parameters themselves.

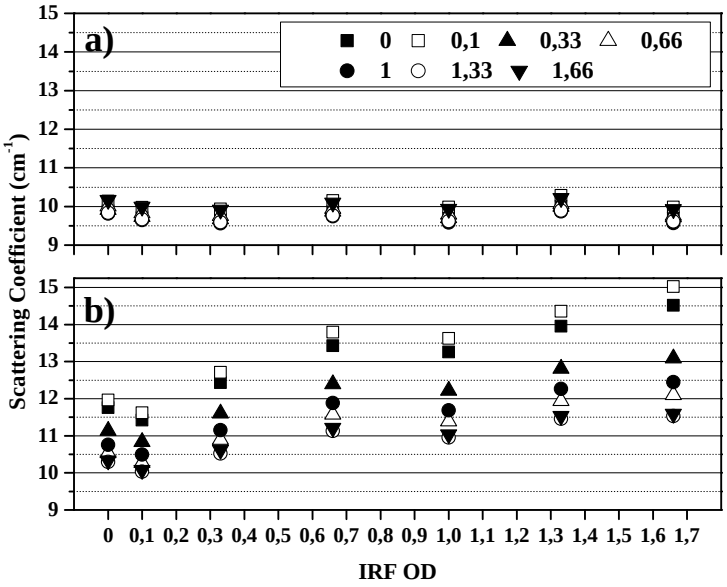

Figure 2.15: Reduced scattering coefficient for phantom B3 (a) and phantom B5 (b) in function of different PMTs attenuations during the IRF recording, at different attenuation during the measurements (see legend, values expressed in OD).

As clarify in table 2.1, to obtain the right value, it is necessary to acquire the measurements on the sample and during the IRF recording with the same attenuation in front of the PMTs.

		P.A. [OD]						
		0	0.1	0.33	0.66	1	1.33	1.66
	0	11,76	11,96	11,13	10,54	10,76	10,30	10,33
	0.1	11,42	11,62	10,84	10,27	10,49	10,04	10,07
	0.33	12,43	12,71	11,60	10,89	11,15	10,52	10,62
IRF	0.66	13,42	13,79	12,39	11,57	11,88	11,13	11,21
[OD]	1	13,26	13,62	12,22	11,39	11,68	10,95	11,04
	1.33	13,95	14,36	12,81	11,94	12,26	11,46	11,53
	1.66	14,52	15,02	13,09	12,10	12,45	11,53	11,59

Table 2.1: Reduced scattering coefficient for phantom B5 acquired at different attenuations [OD] in front of the PMTs during measurements on phantom (P.A,) and during Instrument Response Function (IRF)

2.4.4 Thermal Noise

The sensitivity of the TCSPC technique is limited mainly by the dark counts rate of the detector. The dark counts are the ones that are recorded when there's no light incident on the detector's active area. Defining the sensitivity as the intensity at which the signal is equal to the noise of the dark signal the following equation applies:

$$S = \frac{(R_d * N/T)^{1/2}}{Q} \tag{2.1}$$

where: R_d=dark count rate, N= number of time channels, Q= quantum efficiency of the detector and T= overall measurement time [5]. The dark count rate depends on the cathode type, the cathode area, and the temperature. Taking into account that we cannot change the cathode characteristics, the factor that affects mostly the dark counts is the temperature in the environment around the detector. Additional heating, i.e. by the voltage divider resistor, amplifier connected to the output or any other similar electronic or mechanical device should be avoided. The easiest way to keep the dark count rate low is thermoelectric cooling. As explained in chapter 2.1.2 we introduced, at this purpose, some cooling circuits to activate the internal cooling system of the photomultiplier. As shown in graph 2.16 the introduction of the cooler reduces the dark counts from about 223±15 to 33±6 counts per each acquisition window (12.5 ns).

The PMTs and the optical detection system need to be placed in a dimmed environment, because of the high sensitivity of the PMTs active area. In the first version of the instrument, described in the section before,

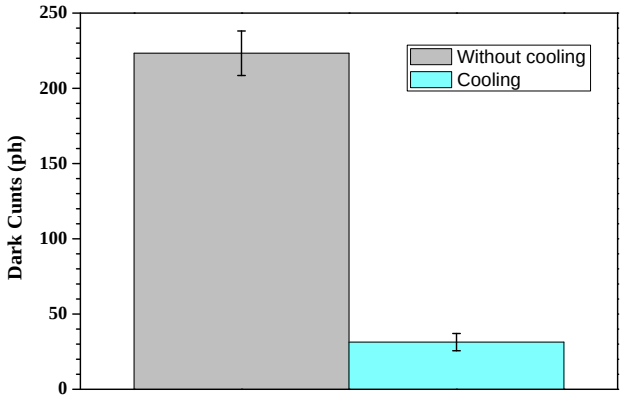

Figure 2.16: Averaged dark counts for one photomultiplier with and without the cooling system. The black bars represent the standard deviation.

we placed the PMTs and all the detection optics in a metal box, so that no light from outside was able to reach the inner part of it. In these conditions we tested the stability in time of the PMTs' dark counts, doing measurements each second for two hours and a half. In figure 2.17 it's clear how the counts decrease during the first 20 minutes (warm-up time) because of the effect of the cooling system. After this initial decreasing, the counts don't remain constant, as they should do, but they continue to increase till the

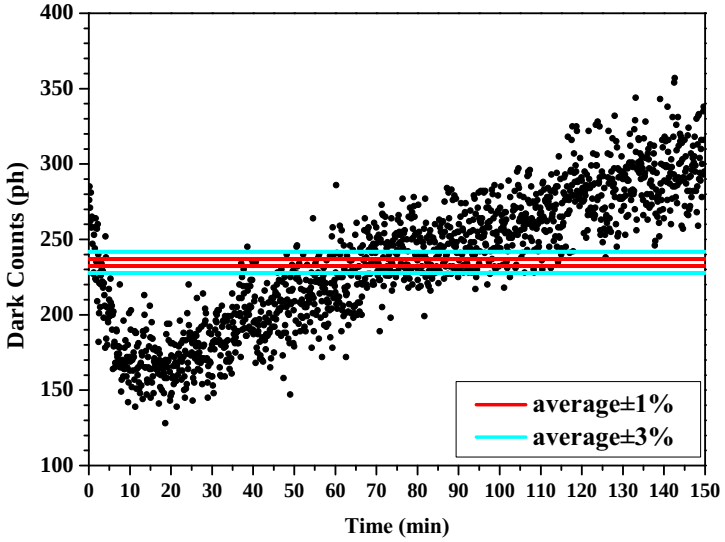

Figure 2.17: PMTs' Dark Counts: stability test of the complete detection section, as it was in the first instrument version.

end of the measurement period. As consequence the signal is never stable in the range ±3% and the ±1% of the average counts, calculated in the last 15 minutes. This is due to the progressive heating of the environment inside the box. The elements that mostly concur to the heating are the attenuators' stepper motors. To prevent the overheating inside the box, the ideal solution was to divide the area where the motors are placed from the one with the photomultiplier tubes. An additional requirement was that the motors should remain in a dimmed environment because they are fixed together with the bundles and are close to the C-mount tubes aperture (see scheme in fig. 2.18(a)). What we thought to do was to divide the detection box in two parts by means of a wall. Making a hole next to the C-mount tube, was possible to place the wall between the PMT and the variable attenuator (red line in figure 2.18(a)). In this way the side with the optical coupling system was left in the dark and close part of the box, while the side with the PMTs was completely open making easier the heat dispersion. Two fans were also added, as shown in figure 2.18(b).

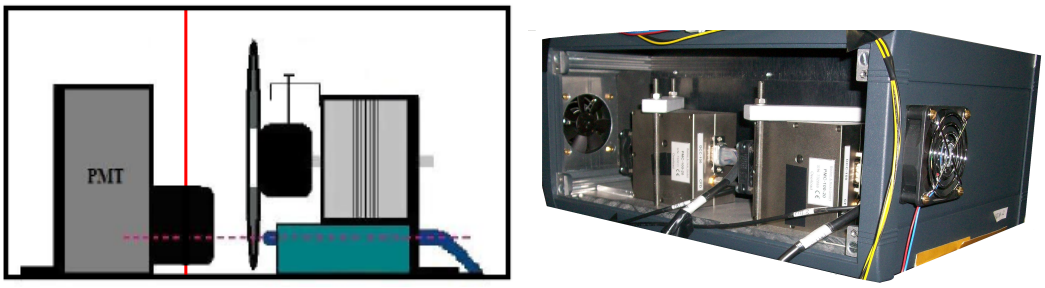

(a) (b)

Figure 2.18: a) Scheme of the detection system inside the box before the modifications. b) The detection box after the modifications. In the fore the new open part with the PMTs.

We tested again the stability of the PMTs dark counts in this new configuration, with a measurement equal to the one explained before. In figure 2.19 the results are shown. With the new configuration the average value of the dark counts obtained after an initial warm-up period (about 30 minutes), is 293.5±1.4. This value guarantees a good signal-to-noise ratio; furthermore it remains stable in time around the average (horizontal lines). Similar results were obtained for the other PMTs employed in the system.

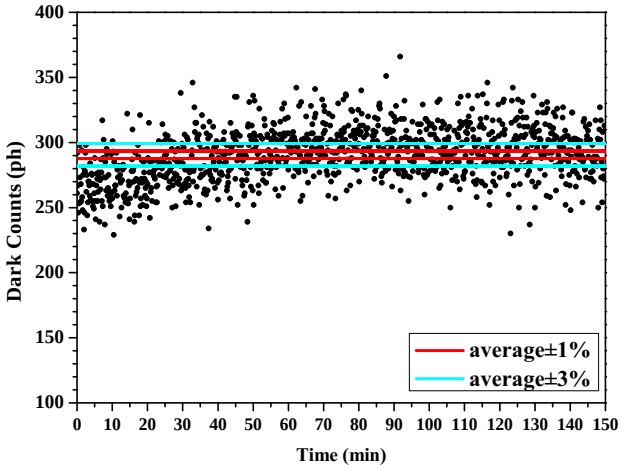

Figure 2.19: PMTs' Dark Counts: stability test of the complete detection section after the modifications.

2.4.5 Bundle Characterization

The choice of the right kind of optical fibers using to detect light coming from the sample, is still an open issue. Good detection fibers should, at first, allow to collect as much signal as possible, being the biological tissues diffusive media. At this purpose a high Numerical Aperture (NA) is required because the signal transmitted is proportional to the square of the numerical aperture. However, the employment of fibers with high NA, such as bundles of fibers, affects the propagation of the optical pulses in terms of temporal dispersion. The time spread inside the fibers can be express as:

$$\Delta t = \frac{nl}{c_o} \cdot \left(\frac{1}{\sqrt{1 - \frac{NA^2}{n^2}}} - 1 \right), \tag{2.2}$$

where n is the refractive index of the core material, l is the length of the fiber bundle, and c_o the speed of light in vacuum [14]. This equation shows that increasing the NA, also the temporal dispersion increases (inter-modal dispersion).

To have an experimental evidence of how much the choice of different bundles influences the optical pulses' characteristics, three different bundles were tested. We used bundles with respectively 1, 2 and 3 mm of diameter, in an IRF configuration, with a thin layer of Teflon in front of the bundles entrance; Teflon it's a scattering medium, which allows to fill the whole NA by light [14]. In table 2.2 the counts and the FWHM recorded are shown. The

	Counts		FWHM		Barycenter	
	690 nm	829 nm	690 nm	829 nm	690 nm	829 nm
3 mm	964000	909800	573	570	3300	3600
2 mm	783800	667600	543	548	3500	3786
1 mm	274000	275800	655	639	3540	3818

Table 2.2: Optical bundles characterization in terms of counts [ph], FWHM [ps] and barycenter position [ps] of the reflectance curve in the IRF configuration.

FWHM found for the smallest bundle is the highest one, in contrast with the theoretical estimation. Probably this is due to a non exacted placement of the bundles during this experiment. Comparing the FWHM of the bundles with respectively 2 and 3 mm of diameters, an increase of the temporal dispersion of about 30 ps was found. The counts increased of the 23%. For this reason it's reasonable to choose bundle with 3 mm of diameter. They are made of step index, glass fibers, and have a numerical aperture of 0.57, a length of 1.5 m and a refractive index of 1.62004. If we use these values inside the equation 2.2 we obtain a theoretical temporal dispersion of 546.56 ps. In our experiment we obtain a FWHM of about 573 ps. This value includes the contribution coming from the entire system, not only from the bundles. Assuming that the input and the output pulses of the bundle, are roughly Gaussian functions of time, the broadening Δt due to the propagation along the bundle may be estimated from this equation [15]:

$$\Delta t_{out}^2 = \Delta t_{in}^2 + \Delta t^2, \tag{2.3}$$

where Δt_{out} is the value found in our measurement and Δt_{in} is the width of the pulses before the bundle. Assuming that the injection fibers give a pulse broadening that is negligible in comparison with the one provided by the bundles, we can use as Δt_{in} the FWHM of the laser at 1 mW, then 70 ps. In this way we obtained an experimental dispersion: $\Delta t_{experimental}$= 568.71 ps, in perfect agreement with the theoretical result. This confirms also that the biggest contribution to the pulse broadening comes effectively from the bundles, being the temporal resolution of the photomultiplier of about 200 ps (FWHM). To reduce the temporal dispersion we could use graded index fibers, instead of step index ones. However the optical filling factor of bundles will be inferior, causing considerable reduction in the light collection efficiency. Another solution could be to reduce the NA of the fibers inside the bundles, but this means again to reduce the intensity of the signal collected. To increase the signal, lost with a prospective decrease of the NA, we could

change the material of the fibers inside the bundle, from glass to plastic, but this is not suitable because the glass guarantees less losses than plastic because of the absence of the Hydroxil (OH^-), which is highly absorbent in the NIR spectral region. It could be also possible to increase the diameter of the bundle doing a trade of between signal attenuation and pulse broadening. At the moment the problem of bundles dispersion and how to solve it remain an open issue for the time-resolved NIRS instruments where the shape of the pulse is a key feature during the extrapolation of the optical parameters (chapter 1).

2.4.6 Improvement of the injection and detection channels number

In the medical diagnostic field, imaging systems are often required, in particular in the neuroscience applications, where is useful to create maps of the hemodynamic activations of the brain cortex. At this purpose, an instrument with an elevated number of channels is required. In our department a time-resolved NIRS system, based on wavelength time multiplexing, with 16 injection and 16 detection channels, was already developed [4]. On the base of the successful employment of that multi-channel instrument in the clinical practice [16], we tried to increase the number of channels of the instrument described in the previous chapter, in order to exploit all the advantages of the wavelength space multiplexing. We increased the total number of channels making changes both in the injection and in the detection section. We increase the injection channel from 2 to 16, and the detection ones from 2 to 4. The instrument is actually a 16X4 multichannel system. We tested the performances of the instrument after the upgrade and we found the same behavior of the previous one in terms of linearity, stability, noise and reproducibility.

Injection channels

To improve the number of injection channels we inserted two 1X9 optical switches (F-109-05 Piezosystem Jena GmbH, Germany) just after the 2X2 optical switch, as shown in figure 2.20. They are independently controlled by the micro-controller unit, which was replaced with a new one (dsPIC30F6014, Microchip Technology, Inc., Chandler, AZ). With this configuration is possible to inject the two wavelengths in eight different channels each, for a total of sixteen injection channels, without losing an SM configuration. One channel per switch was used as “stop” position. The switching time is less than 2 ms. These switches were set up in order to work with fibers with

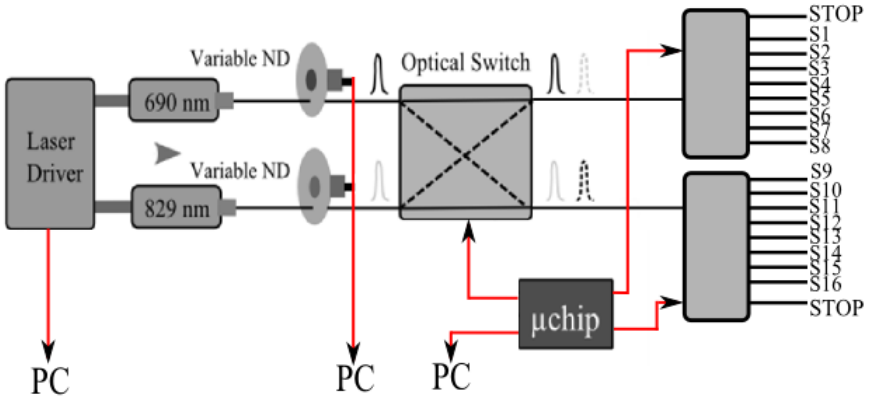

Figure 2.20: Scheme of the new injection section. In black the optical connections, in red the electronic ones.

100 μm of core. Then we changed the optical injection fibers; we used glass, graded index fibers with 100-140 μm (core-cladding) and $NA = 0.29$, in order to reduce the insertion losses due to the laser light coupling with the fibers. During this upgrade, we also introduced the possibility to control the variable stepper motor via PC. In this way, once the attenuators are in the right position, is possible to interrupt the current flux to the motors in order to decrease the environment heating (see paragraph 2.4.4).

Detection channels

To improve the number of detection channels from two to four without losing the independence among them, we doubled the entire detection section. Then we doubled the bundles and the detection boxes and we inserted other two TCSPC boards (SPC130, Becker & Kickl Gmbh, Germany). We replaced the PCI-box with a personal computer able to host four boards. Finally we implemented all the necessary changing in the micro-controller software to control four acquisition line and we implemented the computer stepper motor control, as done in the injection section. In figure 2.21, a scheme of how appears the four channels detection section after the upgrade is presented.

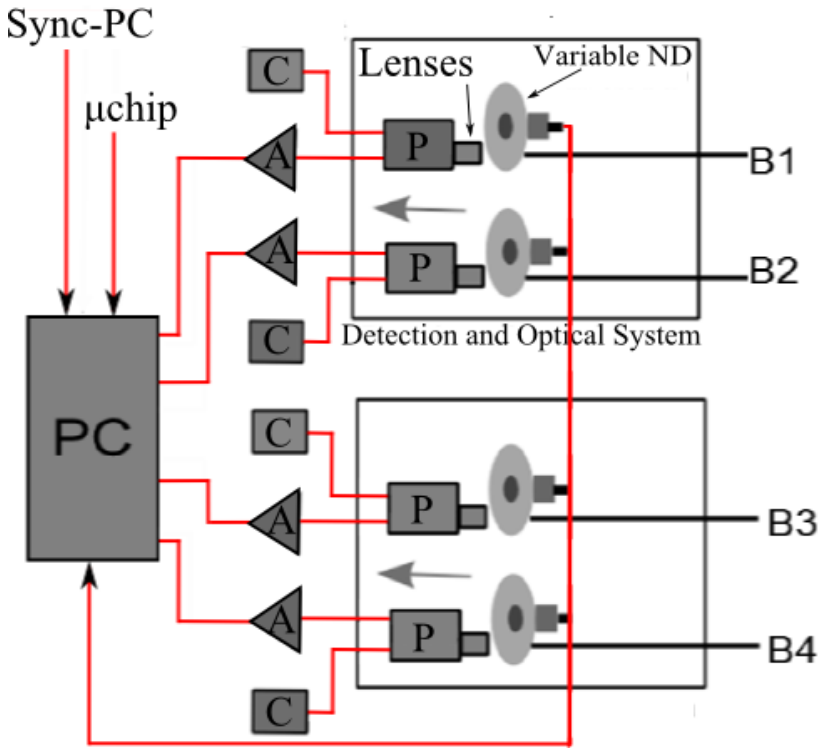

Figure 2.21: Scheme of the new detection section. In black the optical connections, in red the electronic ones. A: Amplifier, C: Cooling circuit, P: photomultiplier tube.

2.5 CONCLUSION AND PERSPECTIVE

In this chapter we described the development and the characterization of a compact, dual-wavelength, dual-channel system for time-resolved fNIRS spectroscopy [12, 13]. It is based, for the first time, on the wavelength space multiplexing approach that allows to avoid cross-talk affecting system based on the wavelength time multiplexing approach and to increase signal-to-noise ratio. The instrument was also validated during preliminary in vivo tests. In the following chapter some applications on human will be presented. Then we described all the tests and the modification applied to the instrument, to improve its performances and to build a new version with sixteen injection and four acquisition channels. For the future, the following further improvements are already scheduled:

- NEW LASER SOURCES: We will employ new semiconductor lasers and drivers (SEPIA II, Picoquant GmbH, Germany), more stable and powerful to increase the signal to noise-ratio.

- NEW DETECTORS: we will employ hybrid detectors (HPM-100-50, Becker&Hickl, Germany) instead of photomultiplier tubes. The principle of the hybrid detector yields excellent timing resolution, a clean TCSPC instrument response function, high detection quantum efficiency up to NIR wavelengths, and extremely low afterpulsing probability. The absence of afterpulsing results in a substantially increased dynamic range of TCSPC measurements. This module is operated via detector controller (DCC-100, Becker&Hickl, Germany).

- NEW ATTENUATORS: with step attenuation (not continuous), to partially solve the problems with the IRF recordings (see paragraph 2.4.3).

- AUTOMATIC ATTENUATION: before performing a measurement, a carefully and independent equalization of all the couples injection-detection channels is necessary. At the moment is carried out by the operator. We are working on an automatic algorithm, which will allow to equalize automatically the signals in the different channels just setting the number of counts needed.

- MEDICAL DEVICE: we will turn the instrument from a prototype into a medical device tailored not only to the laboratory but also to the clinical use. We will enclose it in a 19" rack, in the fulfillment of the safety regulations, with a modularity concept (i.e. the possibility to substitute a section of it without changing the others).

Bibliography

[1] H. Wabnitz, M. Moeller, A. Liebert, A. Walter, R. Erdmann, O. Raitza, C. Drenckhan, J. P. Dreier, H. Obrig, J. Steinbrink, and R. MacDonald, Proc. SPIE 5859, 58590H, 2005.

[2] M. Kacprzak, A. Liebert, and R. Maniewski, European Conferences on Biomedical Optics, Munich, Germany, 2005.

[3] D. Contini, A. Torricelli, A. Pifferi, L. Spinelli, F. Paglia, and R. Cubeddu, Opt. Express 14, 5418, 2006.

[4] D. Contini, L. Spinelli, M. Caffini, L. Zucchelli, A. Tosi, R. Cubeddu and A. Torricelli, Biomedical Optics and 3-D Imaging: OSA Optics and Photonics Congress, Miami, Florida, USA, 2010.

[5] W. Becker, Advanced Time-Correlated Single-Photon Counting, Springer-Verlag, Berlin, Germany, 2005.

[6] A. Pifferi, A. Torricelli, A. Bassi, P. Taroni, R. Cubeddu, H. Wabnitz, D. Grosenick, M. Mller, R. Macdonald, J. Swartling, T. Svensson, S. Andersson-Engels, R. L. P. Van Veen, H. J. C. M. Sterenborg, J. M. Tualle, H. L. Nghiem, E. Tinet, S. Avrillier, M. Whelan, and H. Stamm, Appl. Opt., 44, 2104 ,2005.

[7] R. Cubeddu, A. Pifferi, P. Taroni, A. Torricelli, and G. Valentini, Med. Phys. 23, 1625, 1996.

[8] W. Louisell, Quantum Statistical Properties of Radiation, Wiley, New York, 1973.

[9] S. Prahl, Oregon Medical Laser Center;
See http://omlc.ogi.edu/spectra.

[10] D. Contini, A. Torricelli, A. Pifferi, L. Spinelli, and R. Cubeddu, Proc. SPIE 6629, 662908, 2007.

[11] S. Ferrante, D. Contini, L. Spinelli, A. Pedrocchi, A. Torricelli, F. Molteni, and G. Ferrigno, J. Biomed. Opt. 14, 044011, 2009.

[12] R. Re, D. Contini, M. Caffini, R. Cubeddu, L. Spinelli, and A. Torricelli, Rev. Sci. Instr. 81, 113101, 2010.

[13] R. Re, D. Contini, M. Caffini, L. Spinelli, R. Cubeddu, and Alessandro Torricelli, in Clinical and Biomedical Spectroscopy, Vol. 7368 of Proceedings of SPIE-OSA Biomedical Optics (Optical Society of America, 2009), paper 7368-15.

[14] A. Liebert, H. Wabnitz, D. Grosenick, and R. Macdonald, JBO 8(3), 512-516, 2003

[15] M. Young,"Optics and lasers: including fibers and optical waveguides", Springer-Verlag, Berlin (2000)

[16] A. Torricelli, D. Contini, M. Caffini, L. Zucchelli, R. Cubeddu, L. Spinelli, E. Molteni, A. M. Bianchi, G. Baselli, S. Cerutti, E. Visani, I. Gilioli, D. Rossi Sebastiano, E. Schiaffi, F. Panzica, S. Franceschetti,In European Conferences on Biomedical Optics, SPIE/OSA, Munich, Germany, 2011.

CHAPTER 3

TD-fNIRS Application

As explained in chapter 1, the fields where TD-fNIRS can be applied are different. The instrument we developed (see chapter 2) was employed for different purposes. At first it was used during simultaneous TD-fNIRS and laser Doppler flowmeter acquisitions, as shown in paragraph 3.1. This study aimed at providing an experimental evidence to the "Time-Gated" method, described in paragraph 1.5.1, that we apply to separate the signal contributions coming from different layers of the tissue under examination. It was also interesting to find similarities and correlations between the two techniques in order to understand their complementarity.

The simultaneous use of different acquisition techniques, "multimodal approach", it's a very powerful aspect in the medical diagnostic and research field, in particular in the neuroscience studies, where there is still a lot to understand. To this end we tested also the feasibility of parallel co-registration employing both electroencephalography and our TD-fNIRS instrument, as explained in paragraph 3.2. This study aimed at the monitoring of both the hemodynamic and electrical activity on the prefrontal cortex, during a divided attention task.

In paragraph 3.3, an application on muscle and brain is presented. This study focused on the hemodynamic changes in the arm muscles and in the cerebral cortex while an electrical muscle stimulation is performed.

In the future, the idea is to apply our instrument directly on patient during clinical studies.

3.1 TD-fNIRS vs Laser Doppler Flowmetry (LDF): a "Time-Gated" theory validation study

As explained in paragraph 1.5.1, with the time gated approach is possible to separate the TD-fNIRS signal coming from the deeper layers of the tissue under analysis from the one coming from the upper layers. In this paragraph, an experimental validation of this theory is proposed. To fulfill this purpose, we applied an experimental protocol on the prefrontal cortex (PFC), with the simultaneous employment of TD-fNIRS and Laser Doppler Flowmeter (LDF) technique. From the TD-fNIRS signal is possible to extrapolate both the contributions coming from the more superficial layers and the deeper ones, which are related to an autonomic driven variability. LDF signal is, instead, related to surface flowmotion due to the peripheral autoregulation [1, 2, 3]. The principal aim of this work is to find a correlation between the LDF and the TD-fNIRS signal due to the early photons (superficial signal), thus is possible to provide a validation to the "time-gated" approach. A possible way to test this correlation is the simultaneous use of the two techniques to probe what happens in the prefrontal cortex region during a Valsalva Maneuver (VM).

The Valsalva maneuver is a widely used procedure for assessing the integrity of the Autonomic Nervous System (ANS), in which a subject tries to exhale forcibly with a closed glottis so that no air exits through the mouth or nose as, for example, in strenuous coughing, straining during a bowel movement, or lifting a heavy weight. Specific changes occur in blood pressure and the rate and volume of blood returning to the heart, as the maneuver impedes venous return. Therefore, its main consequences on autonomic regulation consist in variations of perfusion and intrathoracic pressure, and in an increase of heart rate. The raise of intrathoracic pressure that occurs during the Valsalva maneuver elicits rapid changes in preload and afterload [4]. Heart rate and total peripheral resistance, which are increased during the execution of the maneuver, maintain their higher values in the immediate aftermath of it. During the VM we don't expect to see an activation of the gray matter (deep layers) but only a local variation of the hemodynamic parameters on the surface of the prefrontal cortex.

The simultaneous use of TD-fNIRS and LDF devices was previously proposed only in an invasive study on piglets [5], where the authors wanted to verify that the content of information in the TD-fNIRS signal, is not disturbed by the noise due to autoregulation, which contributes to the vasomotion signal detected by the LDF. For the originality of this simultaneous and non-invasive recording is also interested to look not only at the corre-

lation between the two signals but also at the information carried by each signal.

In paragraphs 3.1.1 and 3.1.2 the LDF technique and the compatibility whit our TD-fNIRS instrument will be presented; in paragraph 3.1.3 the measurement campaign to compare the two technique, performed in collaboration with the "Department of Bioengineering" of Politecnico di Milano, is described. In the same paragraph also TD-fNIRS data analysis and the correlation with the LDF ones are shown. We will focus on TD-fNIRS signal and on its correlations with the LDF one. For further details relating to LDF data, see Aletti et Al. [6, 7].

3.1.1 Laser Doppler Flowmetry (LDF)

The Doppler effect is the frequency change of a wave for an observer that is moving relative to the wave source itself. It can be used in the medical field to measure the Doppler shift in wavelength experienced by laser light injected into the tissue and scattered from particles moving with the blood flow. Typically, the technique called Laser Doppler Flowmetry employs monochromatic laser light, to extrapolate the speed of the erythrocytes in movement inside the superficial capillaries, thus is suitable for the non-invasive monitoring of the temporal variation of the micro-circulation blood flow [8, 9]. After being injected into the tissue, light is back-scattered towards the photodetector with a change in phase proportional to the scattering angle. If the particles, i.e. the erythrocytes, are in movement, the scattering angles continuously change and accordingly to that, the pattern on the photodetector changes as well. Since is possible to correlate this pattern, which is the intensity detected as function of the time, to the power spectral density of the laser Doppler, is possible to extrapolate the hematic perfusion. The Doppler shifted percentage of light depends on the concentration of the erythrocytes in movement, while the frequency shift amplitude depends on their average speed. In the systems available on the market, is possible to monitor these two quantities through a unique perfusion index, expresses in arbitrary perfusion unit (A.U.), which represents the product between the erythrocytes concentration and their average speed. It's not possible to extrapolate directly the absolute values of these indexes, because it's not possible to evaluate exactly the volume under the optical probe. Typical values are volumes of approximately 1 mm^3, with a penetration depth of about 1-2 mm.

3.1.2 Instrument compatibility: problems and solutions

The PMTs used in the TD-fNIRS system have an active area which is sensible to all the wavelengths in the range between 300 nm and 900 nm. In addition these photomultiplier tubes are sensible to the single photon, see paragraph 2.4.4 for details. The laser Doppler output beam is a continuous wave laser with a wavelength of 780 nm, a 3 mm beam, with a nominal power of 1 mW [Perimed AB, Sweden]. With empirical trials, we tested that this powerful wavelength causes a high noise in the detected TD-fNIRS signal, which is completely covered when the probe of the two different instruments are close, and saturates the PMTs of our system, avoiding any simultaneous measurement in the same point. For these reasons was necessary to rebuild the optical system inside the C-Mount tube in front of the PMTs and to find the optimal probe placement, in order to avoid the crosstalk between the laser sources coming from the two instruments.

Optical Coupling Rebuilding

We tested different solutions to avoid any effect of the laser Doppler (780 nm) on our detector. The main idea was to add some filters in the coupling system to stop the laser Doppler signal, but allowing the TD-fNIRS wavelengths to pass across them. We took in consideration two different combinations of optical filters:

1. longpass filter, f_{cut} around 829 nm + shortpass filter, f_{cut} around 690 nm;
2. bandpass filter, f_{cut} around 829 nm+ bandpass filter, f_{cut} around 690 nm.

All the filters have to be 25 mm of diameter, to be suitable for the engagement in the tube. They should be as thin as possible, because of the limited space between the PMT and the variable attenuator (52 mm), and not introduce too many losses in the detected signal. The filters that fit better with our requirements were the following ones:

1. longpass: f_{cut}=810 nm, transmittance: T(830)=97.09% and T(780)=0.0197%, thickness 3 mm, clear aperture 23 mm, XIL0810 Asahi Spectra, USA;
2. shortpass: f_{cut}=710 nm, transmittance T(690)=95.04% and T(780)=0.0002%, thickness 1 mm, clear aperture 23 mm, XVS0710 Asahi Spectra, USA;

3. bandpass: f_{cut}=690 nm, transmittance T(690)=81%, thickness 6 mm, clear aperture 22 mm, FWHM 12 nm, XBPA690 Asahi Spectra, USA;

4. bandpass: f_{cut}=828.5 nm, transmittance T(828.5)=84%, thickness 6 mm, clear aperture 22 mm, FWHM 11 nm, XBPA830 Asahi Spectra.

In figure 3.1, the percentage transmittance and the optical density of the filters are shown.

We prepared different optical projects with the software Zemax (Zemax Development Corporation, USA). The introduction of the longpass filter (fig.3.2(a)) reduces the theoretical coupling percentage from the 100% to the 93%, the introduction of the shortpass doesn't reduce the efficiency (fig.3.2(b)), the introduction of the bandpass filters (fig.3.2(c)) reduces it from the 100% to the 45%. All the percentages, mentioned before, are theoretical because in the project we didn't consider the losses that light undergoes when it crosses a physical surface. To estimate them, we measured directly the counts at the photodetector before and after the introduction of the different filters. After the introduction of the longpass and the shortpass

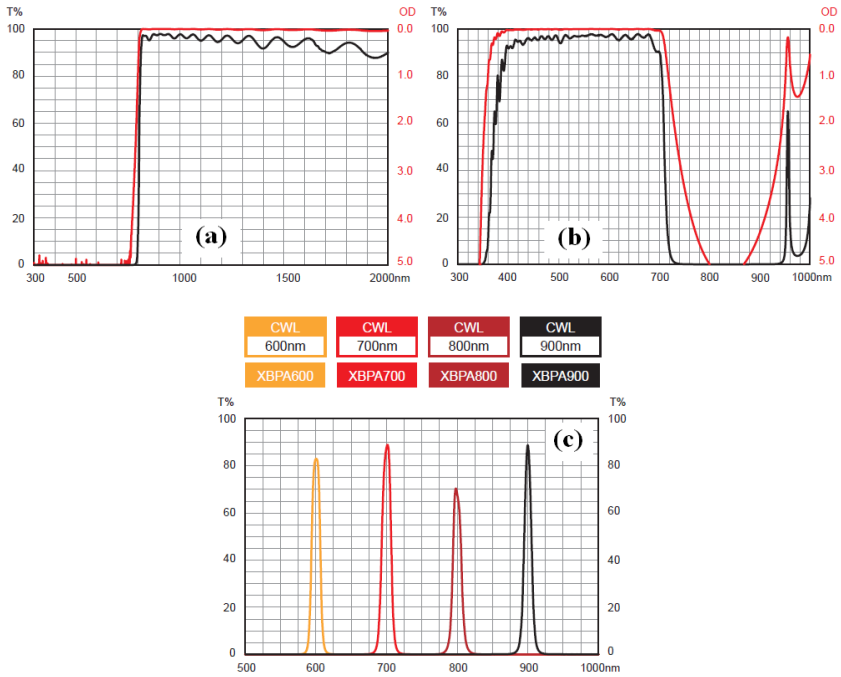

Figure 3.1: Percentage transmittance and optical density of the (a) longpass filter, (b) shortpass filter and (c) bandpass filters (XBPA700-900).

filters, the counts decrease of about the 13%, of about 32% and 42% with the bandpass respectively at 690 nm and 828.5 nm. It's clear how the better solution is the combination of a shortpass and a longpass. We decided to introduce the shortpass in the channel number one and the longpass in the channel number two. In this way during the measurements the photomultiplier number one detected only the NIRS wavelength at 690 nm, the photomultiplier number two, only the one at 829 nm.

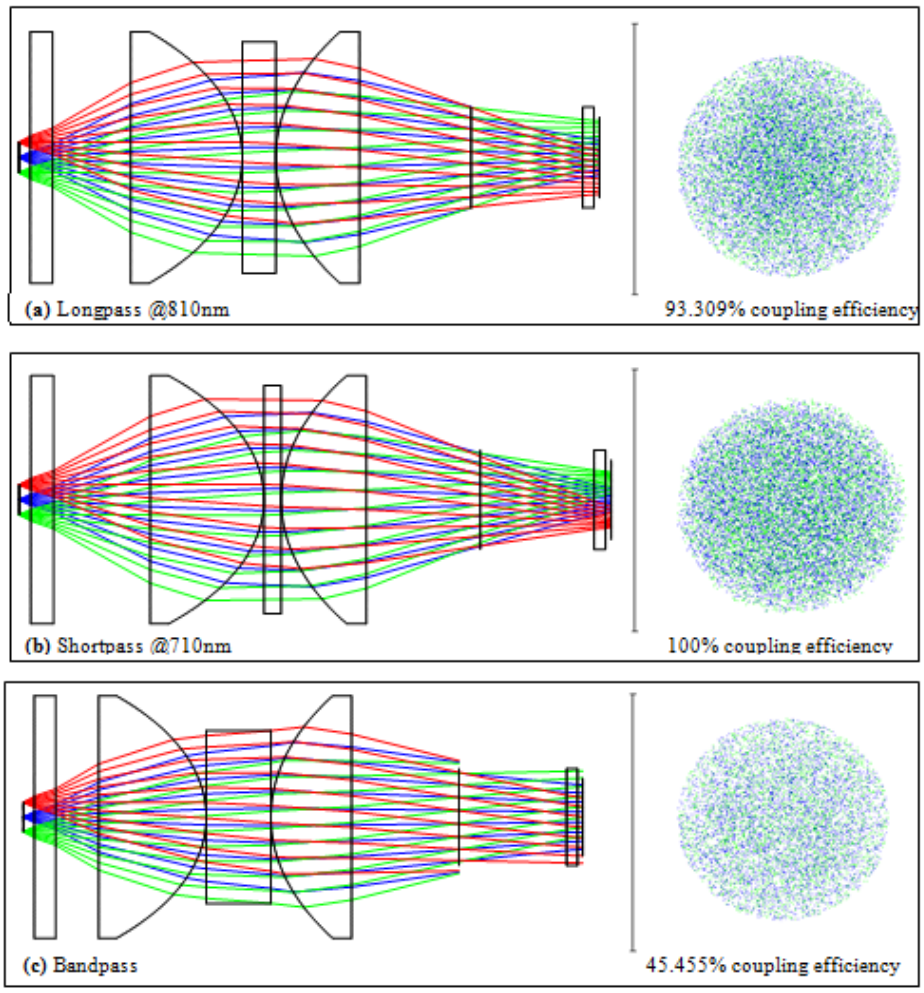

Figure 3.2: Optical project with a) longpass filter, b) shortpass filter and c) bandpass filter.

Probe placement

Despite the introduction of the filters, the laser Doppler signal resulted still too powerful for our detector. We tested its real power founding that it was not 1mW, as declared on the datasheet, but 10 mW. To avoid the optical crosstalk between the two instruments the only other possible solution was to place the TD-fNIRS probe at least 6 cm far from the Doppler ones. However human face is a heterogeneous microvascular region: angiographic characteristics of deep horizontal sub-dermal plexus, endothelial and vascular smooth muscle cell heterogeneity, and plasticity of the microvasculature, autonomic asymmetry and facial neuropsychological asymmetry are possible causes of microvascular asymmetry [10]. Then a preliminary experiment was necessary, to assess if perfusion dynamics acquired on the left and right temples may be averaged in order to reduce the amount of data during simultaneous acquisition with TD-fNIRS signals.

Eight healthy volunteers (25±2 years), sitting comfortably in a quiet, conditioned, dimly lit room, were required to perform a Valsalva Maneuver (VM) for a duration of 15 seconds. All subjects, who voluntarily enrolled in the study after signing the informed consent authorization, were non-smokers and had no history of cardiovascular or respiratory disorder. Alcohol, caffeine and any drugs were not taken for a half day before the experiments. The laser Doppler flowmeter was connected to a laptop equipped with a data acquisition system (Perimed Systems, Inc., Sweden). Two coaxial probes (Perimed AB, Sweden) were placed on the right and left temples with double-sided tape. Prior to the beginning of the protocol, the subjects adapted to the environment where the experiment was carried out, sitting on an armchair for at least 10 min after placing the LDF and TD-fNIRS probes on their head. Baseline recordings of spontaneous vasomotion, in conditions of spontaneous hemodynamic variability, were acquired for 10 min at rest. At the end of this baseline period all subjects were asked to execute a forced expiratory maneuver (VM) for 15 s. Then recovery baseline recordings followed for 10 min, to assess the spontaneous vasomotor variability and recovery from the strong stimulation provided by VM.

The signals were acquired at 32 Hz, then time series were extracted and downsampled to 4 Hz, by means of an anti-aliasing low-pass filter, in order to limit the bandwidth to the regulatory mechanism of interest, from very slow local vasomotor phenomena related to vascular autoregulation up to faster respiratory and heart beat frequencies. LDF signal was first filtered by a moving average to remove any residual low frequency trends, which might introduce spurious peaks in the power spectrum. Correlation analysis between LDF channels (left temple, right temple) before VM provided with the cor-

relation coefficient range of microcirculation perfusion at rest (0.65±0.85). During recovery following VM, the coefficient decreased to (0.45±0.85) (Fig. 3.3). Pre-VM r-coefficient values were higher than post-VM in 7 subjects out of 8 ($p< 0.01$) (Table 3.1). During VM, higher values of correlation between the two LDF channels were found (0.96±0.02, $p< 0.001$). The good correlation obtained in the preliminary experiment subsequently enabled to average the two laser Doppler signals, in order to reduce redundant data.

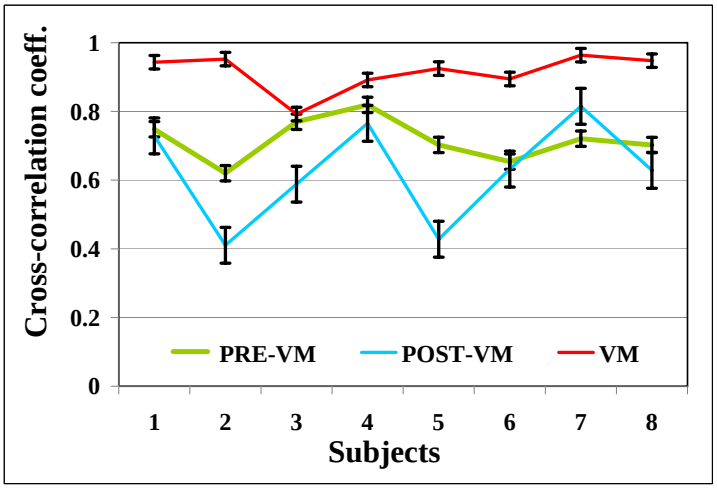

Figure 3.3: Cross-correlation coefficients between left and right-temple skin flow signals in pre-VM, during Valsalva, and post-VM periods in the 8 subjects participating in the preliminary protocol. (Error bars represent the standard error).

Subject	pre-VM (p-value)	VM(p-value)	post-VM (p-value)
1	0.75 $p< 0.01$	0.94 $p< 0.001$	0.73 $p< 0.01$
2	0.62 $p=0.08$	0.95 $p< 0.001$	0.41 $p=0.12$
3	0.77 $p< 0.01$	0.79 $p=0.07$	0.59 $p< 0.09$
4	0.82 $p< 0.01$	0.89 $p< 0.01$	0.77 $p< 0.05$
5	0.70 $p< 0.01$	0.92 $p< 0.001$	0.43 $p=0.07$
6	0.65 $p=0.05$	0.89 $p< 0.01$	0.63 $p< 0.05$
7	0.72 $p< 0.01$	0.96 $p< 0.001$	0.81 $p< 0.01$
8	0.70 $p< 0.01$	0.95 $p< 0.001$	0.63 $p=0.05$

Table 3.1: Correlation coefficients of LDF signals of left and right temples. During VM correlation is significant in 7 out of 8 subjects ($p< 0.01$).

3.1.3 TD-fNIRS and LDF measurements

During this measurement campaign, approved by the Institutional Review Board (IRB), we employed simultaneously our 2X2 version TD-fNIRS instrument and the commercial LDF, previously described. Thirteen healthy volunteers (28±2 years) were enrolled and gave their informed consent to participate in the study. The experimental set-up and the protocol were the same of the preliminary one: 10 min of spontaneous variability recordings, 15 s of force expiratory Valsalva maneuver and 10 min of recovery to baseline (for details see the previous paragraph). The TD-fNIRS probes were place on the forehead, slightly to the right of the frontal suture, in Fp2 position, and with 2 cm between the source fibers and the detection ones (interfiber distance). Data were acquired at 1 Hz to improve the signal-to-noise ratio, without moving the switch. The LDF probes were placed on the left and right temples at a distance longer than 6 cm from the TD-fNIRS optode for the reasons illustrated in paragraph 3.1.2. Data were acquired at 32 Hz.

TD-fNIRS signal

Artifact free, approximately 5 minutes long stationary segments were selected in pre-VM and post-VM epochs of the acquired data. We extrapolate, as explained in paragraph 1.5.1, the early and late gates for both oxy- and deoxy-hemoglobin; in the following, the signals will be referred to as oxyHb-extra, deoxyHb-extra, oxyHb-intra, and deoxyHb-intra respectively for early and late gates. In figure 3.4, an example of oxyHb in the extra cerebral and intra cerebral compartment for one typical subject. The values are obtained subtracting the average value of the baseline period. It's clear how the effect of the VM is evident in the extra cerebral layer, where the oxyHb increases. When the VM starts (600 s) is visible an undershoot that represents the deep inspiration preparing the VM onset, followed by a marked overshoot during the forced expiration. Intra cerebral TD-fNIRS signals calculated from the late photons measurements did not show the fast rising spike inside. This difference implies that the model to separate early and late photons is working properly, causing VM just an autonomic (superficial) reaction. The same differences between the two compartments were found in the deoxy-Hb. As example, in figure 3.5, the average of the deoxy- and oxy- Hb in the intracerebral compartment is shown.

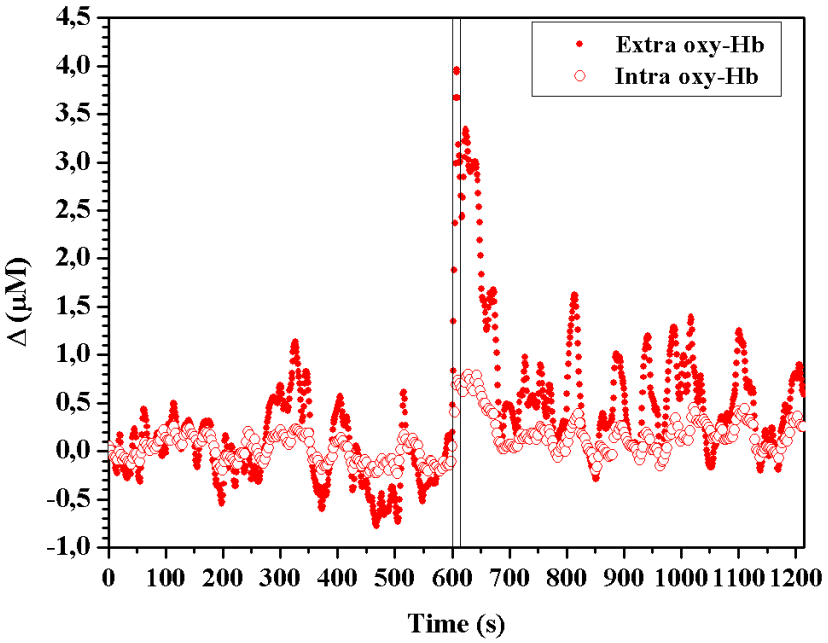

Figure 3.4: TD-fNIRS signal of extra- and intra- cerebral oxyHb.

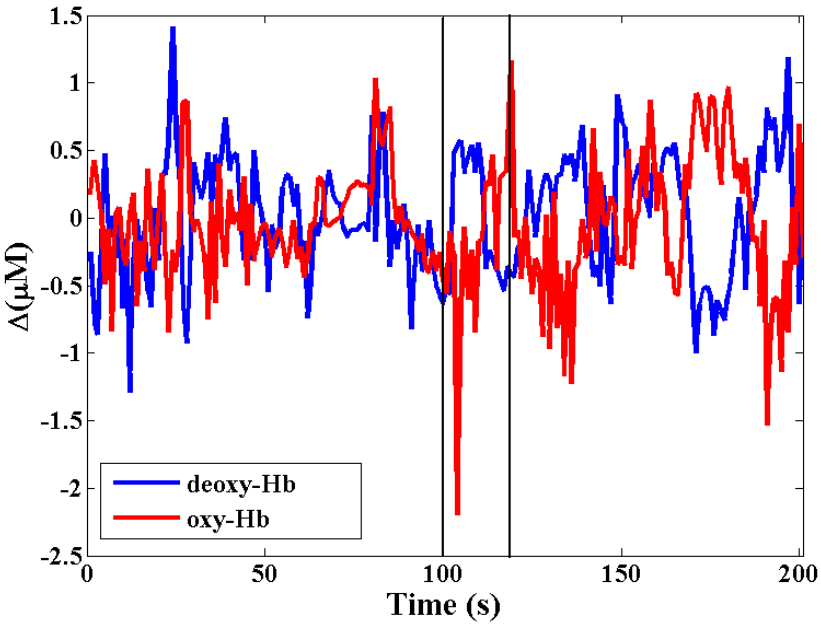

Figure 3.5: Grand average of TD-fNIRS cortical oxy-Hb (red) and deoxy-Hb (blue) measurements, referred to late photons measures of intracerebral hemodynamics.

LDF signal

LDF signals were acquired at 32 Hz, then time series were extracted and downsampled to 4 Hz, by means of an antialiasing low-pass filter, in order to limit the bandwidth to the regulatory mechanisms of interest, from very slow local vasomotor phenomena related to vascular autoregulation up to faster respiratory and heart beat frequencies. In addition, time series derived from the right and left LDF raw measurements were averaged. LDF signal was first filtered by a moving average to remove any residual low frequency trends, which might introduce spurious peaks in the power spectrum. For details regarding the LDF signal analysis see Aletti et al. [6].

TD-fNIRS vs LDF: time analysis

Time domain analysis entailed the computation of cross-correlation functions between the averaged LDF signal and oxyHb-extra, deoxyHb-extra, oxyHb-intra, and deoxyHb-intra in three different epochs: pre-Valsalva (1200 samples), during Valsalva (50 samples) and post-Valsalva (1200 samples). All the 13 volunteers display similar responses to VM in the averaged LDF and surface oxy-Hb dynamics, as shown in figure 3.6. Both the signals present the typical pattern of the VM as explained in paragraph 3.1. After the end of the VM (15 s after the onset), surface oxy-Hb concentration fall more rapidly ($\sim$ 13 s) than the LDF signal ($\sim$ 18 s). The comparable patterns shown by both LDF and extracerebral TD-NIRS in the time domain ap-

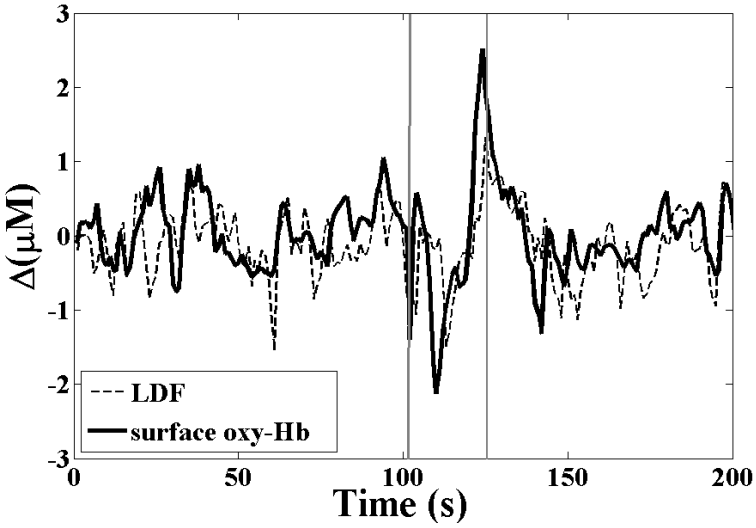

Figure 3.6: Grand average of LDF (dotted) and TD-fNIRS surface oxy-Hb (solid) signals.

peared consistent with previous results reported by Tsuji et al.[11], and by Brady et al.[12], who respectively found a peak of coherence between TD-fNIRS signal and arterial blood pressure in neonates and between TD-fNIRS and LDF in piglets, at frequencies lower than 0.04 Hz. For the time interval preceding VM, the statistical analysis was carried out by applying parametric t-paired test to correlation data of the paired LDF channels; a Wilcoxon rank sum non parametric test was used to assess significant differences between LDF and TD-fNIRS data. Differences between two groups (e.g. pre-VM vs. VM; post-VM vs. VM and pre-VM vs. post-VM) were analyzed using paired 2-tailed Student's t test if Kolmogorov-Smirnov null hypothesis of normal distribution could not be rejected. The level of significance was set to p=0.05. Normalized correlation coefficients between LDF and TD-fNIRS during VM were compared by using Wilcoxon sum rank nonparametric test in order to get more robust statistics being the population not normally distributed (Kolmogorov-Smirnov, $p< 0.05$). All the statistics were performed using R statistical software and Matlab Statistical Toolbox. High correlation ($r> 0.9$) was found during VM between LDF and all TD-fNIRS signals; but the correlation, calculated in this way, doesn't take into account the smaller amplitude of the intra cerebral signal, in comparison with the extra cerebral one. However, after scaling it (Fig. 3.7) by TD-fNIRS signal rms (i.e., TD-fNIRS rms correlated to LDF), significantly higher values (0.04±0.010, p=0.02 surface oxy-Hb; 0.01±0.006, p=0.01 surface deoxy-Hb) were obtained for surface signals compared to cortical ones (0.02±0.008 cortex oxy-Hb; 0.009±0.0015 cortex deoxy-Hb).

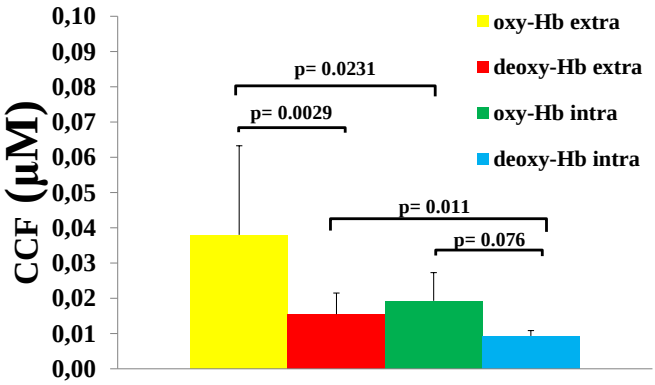

Figure 3.7: Cross-correlation coefficients between average LDF and TD-fNIRS, rescaled by rms of surface and cortex oxy-Hb and deoxy-Hb. Data are mean ±SD.

TD-fNIRS vs LDF: spectral analysis

Similarly, higher r coefficients were found for oxy-Hb compared to deoxy-Hb. LDF signal, carried also some oscillations which are characteristic of different physiological systems (cardiac, respiratory, autonomic,...). These oscillating components covered a wide frequencies range, for this reasons a spectral analysis of the signals was done, not only on LDF signal but also on the TD-fNIRS one, in order to find other correlations between the two techniques. Typically the frequencies spectrum is divided in three regions: very low frequencies (VLF: 0.005-0.04 Hz, vascular band), low frequencies (LF: 0.04-0.15 Hz, autonomic band) and high frequencies (HF: 0.15-0.4 Hz). The spectral components of the LDF signal were analyzed in different previous works [3, 13], but their origin is still not completely understood, in particular in the VLF region. In this work the frequency domain analysis was performed as followed. Power spectra of time series before and after VM were estimated via autoregressive (AR) parametric model estimation, and also computed by non parametric approaches (Welchs modified periodogram). While AR spectral estimation provided with good results with LDF time series, severe limitations were found with TD-fNIRS, due to high levels of baseline drifts. For this reason the analysis was repeated by means of Welch's periodogram and results presented in the following are referred to this spectral computation technique. Original signals were split into shorter segments, partially overlapping (overlap of 50%). A data window (Hamming window of 80 samples, fs=1 Hz) was applied to each stationary segment (pre-VM, post-VM) and a modified periodogram was computed. The use of the Hamming window was aimed at improving the spectral resolution by reducing the effect of lateral lobes. Finally power spectral density (PSD) estimates of all segments were averaged. Power in the VLF, in the LF, in the HF band, and in the bands where the dominating phenomenon is the pulse ($0.8<f<2$ Hz) was computed [14]. Then normalized correlation coefficients between power contents in the VLF and autonomic band were compared by using Wilcoxon sum rank nonparametric test. Regression analysis was applied to quantify the correlation between the spectral power of LDF and TD-fNIRS time series in the VLF band and in the autonomic band (LF+HF: 0.04-0.26 Hz). Also, cross-correlation analysis was carried out to assess the correlation between VLF, LF, and HF normalized powers in the spectra of the left temple and right temple laser Doppler flowmotion signals. Boxplots were derived to compare medians and averages of different populations through paired Student t-test. Wilcoxon sum-rank non-parametric test was applied to the second phase-protocol data. During pre and post-VM, the spectral analysis of LDF and TD-fNIRS time-series revealed the presence of

a large VLF component and significant activity in the LF (vasomotor) and HF (respiratory) band, as shown in figure 3.8. Due to the relatively low spontaneous variability of the TD-fNIRS signal, and to the possible entrainment phenomena occurring when respiratory frequencies of subjects slowed and approached the 0.15 Hz (which may have occurred because of the length of the protocol), limits in separating LF and HF bands were found. The LF and HF bands were lumped together and taken into consideration as one band, representative of autonomic control of hemodynamics. This was also justified by the fact that either in pre-VM and post-VM epochs, both LDF and TD-fNIRS displayed VLF and LF+HF activity, but low correlations ($0.1<r<0.2$) were found in both bands between TD-fNIRS and LDF signals. Power coherence calculation confirmed VLF band-related power to be the main common power component of surface skin flowmotion signal detected by LDF and extra cerebral oxy-Hb obtained through TD-fNIRS, both before and after VM. Therefore the HF power component is not significant in TD-fNIRS signal. The power of VLF and LF+HF band did not vary significantly post Valsalva maneuver in either LDF or extracerebral oxy-Hb signals (Fig.3.9). The preponderant power content in the VLF band was consistent with the typically slow rhythms of peripheral microvascular hemodynamics [9] which characterize the vasomotion phenomena detected by the LDF signal.

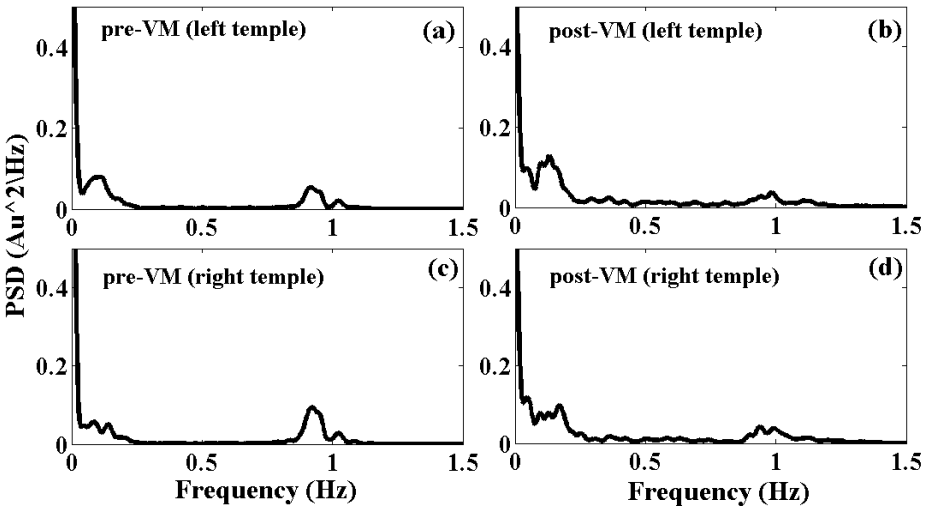

Figure 3.8: Power spectra of LDF (a-d) signals during pre-Valsalva (left) and post-Valsalva (right) for one subject.

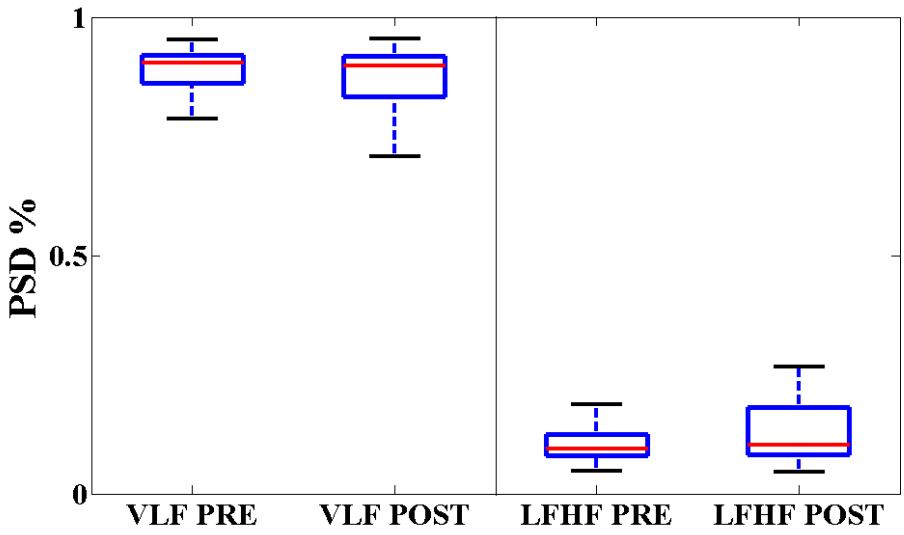

Figure 3.9: Box-plot of total VLF (left) and LF+HF (right) power of LDF before and after VM.

	Pre-Vm		Post-VM	
	VLF	LF+HF	VLF	LF+HF
LDF	0.889±0.050	0.101±0.036	0.868±0.075	0.131±0.066
Deoxy-Hb extra	0.711±0.160	0.289±0.192	0. 609±0.157	0.391±0.136
Oxy-Hb extra	0.648±0.155	0.351±0.159	0.635±0.140	0.365±0.142
Deoxy-Hb intra	0.750±0.127	0.249±0.118	0.739±0.101	0.264±0.096
Oxy-Hb intra	0.770±0.120	0.232±0.119	0.756±0.117	0.246±0.115

Table 3.2: Values of VLF and LF+HF components assessed on LDF and TD-fNIRS signals (mean±std).

3.1.4 Conclusion and perspective

This study demonstrated the feasibility of simultaneous TD-fNIRS and LDF measurements and confirmed the effectiveness of time resolved TD-fNIRS in separating deep from surface signals during provocative maneuvers like a Valsalva maneuver. With a time-gated analysis of the TD-fNIRS signal is possible to assume that the extra cerebral signal, described by the early photons, is representative of the extra cortical areas of the frontal skull. The intra cerebral one, described by the late photons is representative of the activations in the gray matter of the brain. This evidence strengthens that the model-based separation of time-resolved NIRS early (superficial) and late (deep) photons is able to cancel, or at least attenuate, the surface confounding effects.

One of the issues which remains to be addressed is whether autonomic control [15] affects deep cortical hemodynamics more than simple systemic provocative tests, such as Valsalva. Further experiments, including other autonomic tests, might shed light on the difference in variability between surface and cortex TD-fNIRS signals. Considering the potential significance of TD-fNIRS in portraying the functional activation of the prefrontal cortex, it might also be useful to further investigate the relationship between surface flowmotion and deep recordings in presence of simple functional tasks [16], such as finger tapping.

3.2 TD-fNIRS vs. Electroencephalography (EEG): co-registration during a divided attention task

One of the goal of the modern diagnostics is to combine different techniques in order to overcome possible uncertainties in the results, which is possible to encounter using a single method. For this reason, several works present the simultaneous use of the TD-fNIRS technique together with Electroencephalography (EEG) [17, 18, 19]. Therefore there are some investigation fields where, despite an optimum status of the technique already employed, the measurements results are still incomplete. It's the case, for example, of the divided attention studies. Divided attention is the skill to distribute the limited mental resources to different sources of information at the same time and/or to a number of sensory modalities [20]. Among the neurophysiological categories of attention, the ability to split attention to more than one feature and/or object simultaneously is the one that more easily exhausts cognitive capacities. Previous studies have suggested that prefrontal, parietal, and limbic areas support the higher attention sub-functions. A dual task is not, however, inevitably associated with higher prefrontal activation [21]. It remains unclear which areas in the brain are responsible for divided attention. The EEG technique is well suited to demonstrate differences in brain-state which have been described when performers adopt an effective strategy in order to fulfill cognitive, auditory, visual and motor tasks. The electrical activity has been widely investigated, but it is interesting to complete this information with hemodynamics parameters. The considerable differences existing between hemodynamic and electrical signals, their different physiological nature and time dynamics, make it difficult to investigate neurovascular coupling as a whole. In previous studies it has been demonstrated that the performance of a cognitive task involves the response of several physiological districts, such as central nervous system (CNS), autonomic nervous system (ANS) and cerebro-vascular system [22, 23, 24].

The aim of the study is to test the feasibility of simultaneous EEG and TD-fNIRS recordings, during the probes placement phase, and to clarify the time relationship and the information shared between the two techniques for what concern data analysis. In order to obtain further information about the hemodynamic response and to study the activation of ANS elicited by the execution of the cognitive task, an additional electrocardiographic (ECG) derivation was recorded. The TD-fNIRS recordings were executed by means of the 2X2 instrument described in chapter 2.1.2, while the EEG recordings and data analysis were performed in collaboration with the "Department of Bioengineering" of Politecnico di Milano [25, 26].

3.2.1 Experimental protocol

Sixteen healthy volunteers (8 male, 8 female) took part in the present study, which was approved by the Institutional Review Board (IRB). All subjects were right handed and declared normal vision and hearing. Mean age was 25.6±3.8 years. None of them had a life time or family history of neurological or psychiatric illness. Written informed consent was obtained from all volunteers, after that and test procedure have been explained. The divided attention test (TDA) is a modification of the attention test described in Zimmermann et al. [27], achieved in order to improve its difficulty. It was presented on a PC screen using the software Presentation (Neurobehavioral Systems Inc, Albany, CA) and it consists of a 86 seconds baseline rest period, which provided the subject's baseline track, five blocks of task lasting 165 s each (inter-block period of 85 s) and a 300 seconds recovery period at the end of the experiment. Each activation block contained 60 couples of auditory and visual stimuli, 5 targets and 55 non-targets. Visual stimuli consisted of images containing 17 white crosses on a black background, in random position, which were considered "Valid Visual Condition" (VVC). When, instead of a cross, one white circle appeared it was considered an "Invalid Visual Condition" (IVC). In the meanwhile the auditory stimuli were presented. They consisted of two sounds of the same tone, considered "Valid Auditory Condition" (VAC), while couples of sounds with a different tone (1000 or 1500 Hz, 100 ms lasting) were considered "Invalid Auditory Condition" (IAC). The subjects were asked to press the left button of the mouse as fast as possible whenever an IVC appeared, to press the right button of the mouse as fast as possible whenever an IAC was presented, and to withhold the response when both stimuli were valid, see figure 3.10(a). The task was designed so that it could never happen that an IVC was simultaneously presented with an IAC. The Inter Stimulus Interval (ISI) between two consecutive images was set at 2650 ms, and every visual stimulus (image) remained on the screen for 1500 ms (stimulus duration). The total amount of presented images was 300, as well as the number of couples of tones; among them all, 15 images and 15 couples of tones were invalid. Then, the probability was set at 5 for both IVC and IAC.

During the measurements a 19 channels EEG was recorded with Ag/AgCl electrodes (impedance below 5 KΩ, international 10/20 system), using common ground as reference in A1 and A2 positions (Figure 3.10(b)). Two couples of bipolar electrodes were used to collect Electrooculogram and ECG signal. The recordings were performed by a 32-channel AC/DC amplifier (SAM-32, Micromed Italy, QuickBrain System). The A/D sampling rate was 256 Hz.

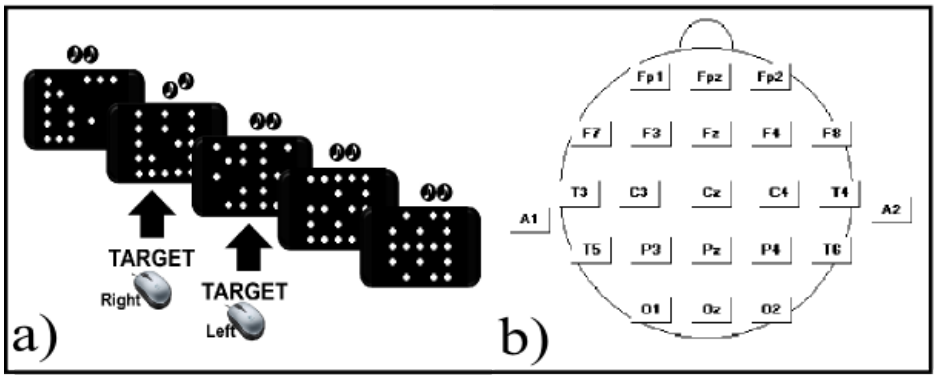

Figure 3.10: (a) Schematic representation of the stimulation protocol. (b) international 10-20 electrodes placement.

For the TD-fNIRS acquisition our 2X2 instrument, described in chapter 2.1.2, was employed. The two channels were positioned on the forehead of the subjects, on the left and right side, below the FP1 and FP2 electrodes. The two instruments have been synchronized so that the recording of the signals started automatically with the beginning of the test and all the signals (NIRS, EEG and ECG) and the behavioral data recorded by Presentation were time realigned. Measurements of the optical properties of the prefrontal cortex were performed at the same time in the two different locations with a sampling rate of 1 Hz.

3.2.2 Data analysis and results

TD-fNIRS signal

To enhance the contribution from deep layers and to remove possible disturbances caused by superficial layers in the TD-fNIRS signal, a correction method based on the use of late time windows (1750-2500 ps) was applied (see paragraph 1.5.1). We extrapolated the oxy- (O_2Hb) and deoxy-hemoglobin (HHb) content and then we subtracted the baseline from their value. At first we evaluated the signals coming from the Fp1 and Fp2 pads, in order to understand if their behavior was the same and it was possible to average the two contributions. The high correlation values of the deep oxy-and deoxy-hemoglobin, for all the sixteen subjects, suggested that was possible to average the two signals.

After that, TD-fNIRS signals were averaged over all the measured subjects, in order to understand the general behavior of the signal with the time.

In figure 3.11 the averaged signals show an increase of O_2Hb and a correspondent decrease of HHb at the beginning of the task period. Then, HHb shows a return to the baseline values, while O_2Hb shows only an average reduction during the task, but without any return to the baseline condition. This behavior, related with a prolonged cognitive effort, was already found

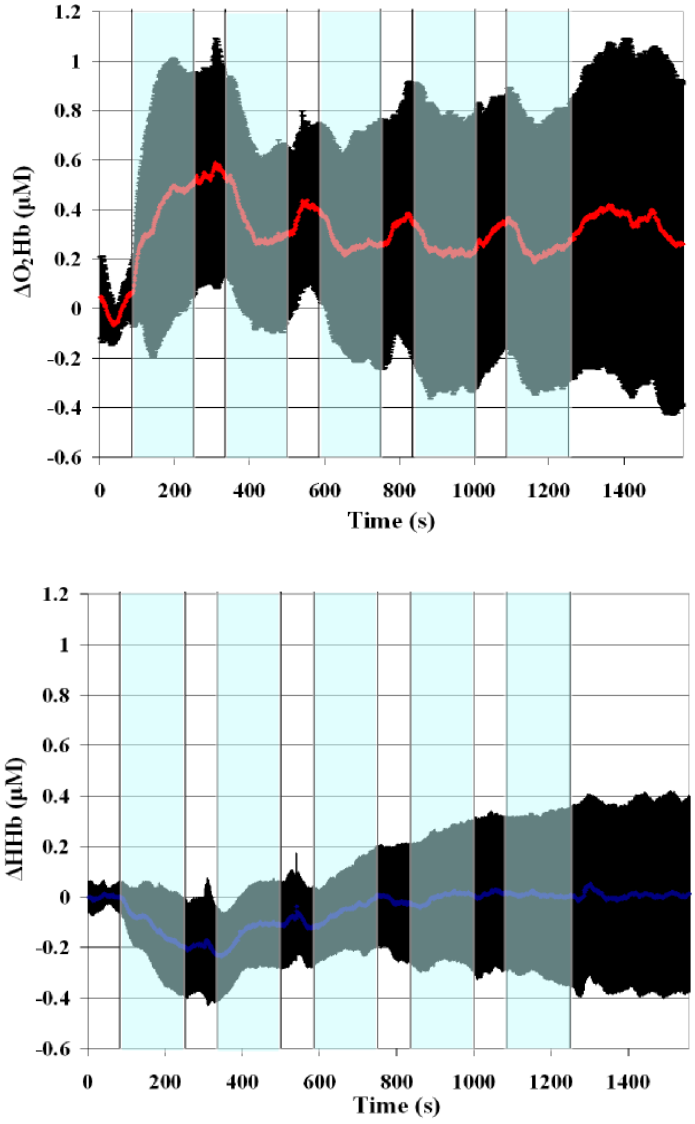

Figure 3.11: Average over all the measured subjects of O_2Hb (first row) and HHb (second row) signals. Black areas represent the standard deviation.

in a previous study during a Continuous Performance Test [28]. Observing the hemodynamic pattern of the 5 different trials, constituting the entire task, it is possible to identify a different behavior between the first block and the following ones. In fact, in the first block we observe a typical activation pattern with an increase of O_2Hb and a decrease of HHb with respect to the baseline values. Conversely, in the following blocks, we observe a decrease of O_2Hb and a slightly increase of HHb. A possible explanation of this different trend could be the presence of a recovery behavior with longer latency during the task repetitions between oxygen consumption, caused by neurons activation, and local oxygen recruitment, caused by changes in local blood flow. A further confirmation of this hypothesis is the increase of O_2Hb during the rest periods, interleaved between two subsequent trials. Then, a frequency analysis was applied. We identified two main contributions in TD-fNIRS signals: one, in low frequencies range, due to the sustained attention condition required by the whole test and another one, in a higher frequencies range, due to the modulation caused by the switching between test and rest periods. We separated TD-fNIRS low and high frequency components (LF and HF): a low pass filter (Chebychev IIR filter, 6 coefficients, pass band 0,002 Hz and stopped-band 0,003 Hz, with 30 dB maximum ripple amplitude) allowed the isolation of LF contribution, which was then subtracted from the whole signal to obtain the HF contribution. In figure 3.12 an example is shown. The LF signal is modulated by the generic cognitive load due to the complexity of the whole experiment. It expresses the change from a basal condition to a condition where the subject is stimulated from a neurosensorial point of view. The HF one is instead modulated by the periodicity of the single task blocks.

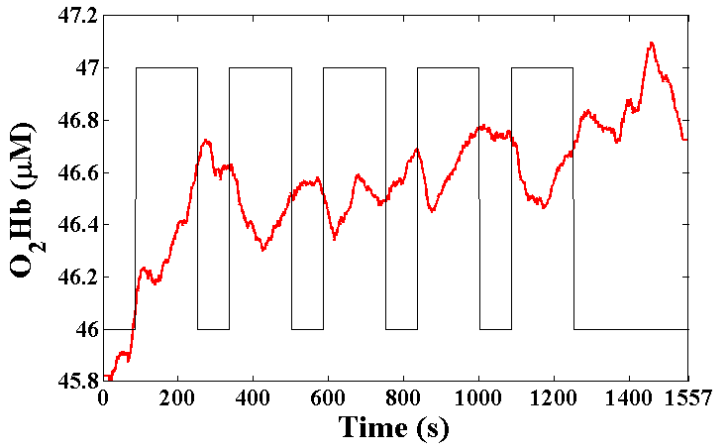

(a) Time course of the original O_2Hb depth signal. The square wave represents the time course of the task blocks.

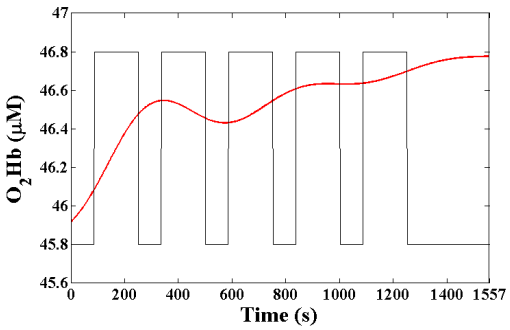

(b) LF component.

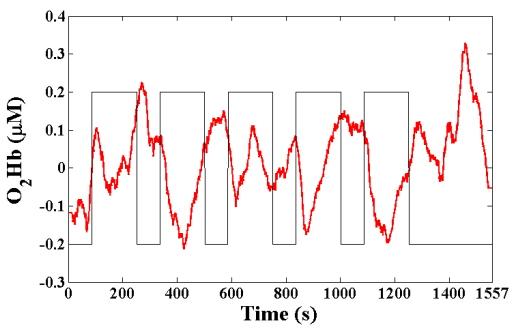

(c) HF component.

Figure 3.12: TD-fNIRS frequency analysis

EEG signal

At first, in a preliminary analysis, the raw EEG data were digitally band pass filtered between 0.5 and 48 Hz, they underwent Laplacian Surface Operator and were cleaned by ocular and muscular artifacts by Independent Component Analysis (ICA) and downsampled at 128 Hz, using the free Matlab toolbox EEGlab (Schwartz Center for Computational Neuroscience, University of California, San Diego, CA) for reducing the computational time of following processing steps. After that a time-resolved analysis was done to obtain a preliminary Event-Related Potential (ERP) Analysis. The preliminary ERP analysis shows differences in the electrical response at latencies of around 400 ms, after a VVC stimulus with respect to the response after an IVC stimulus, and mainly in the median parietal sites (Fig. 3.13). The same behavior was also found for the auditory stimuli. There is ample evidence that P300 latency varies with stimulus evaluation time. Stimulus evaluation is performed compulsively, even in ignore conditions. Hohnsbein et Al. [29] found that P300 latencies are delayed for divided attention as compared with other attentive categories, and peak around 380 ms with maximum amplitude over the median sites Pz and Cz. This is probably due to the fact that stimulus processing is suboptimal in the divided attention tasks, as a result of the dilution of processing resources. Differently, there are weaker dissimilarities between valid and invalid conditions in the EEG signals over the pre-frontal and frontal sites (FP1, FP2, Fz) in both conditions (Fig. 3.14). A possible explanation could be that frontal cortex activation is more related to a general attentional request of the task, but it is only partially involved

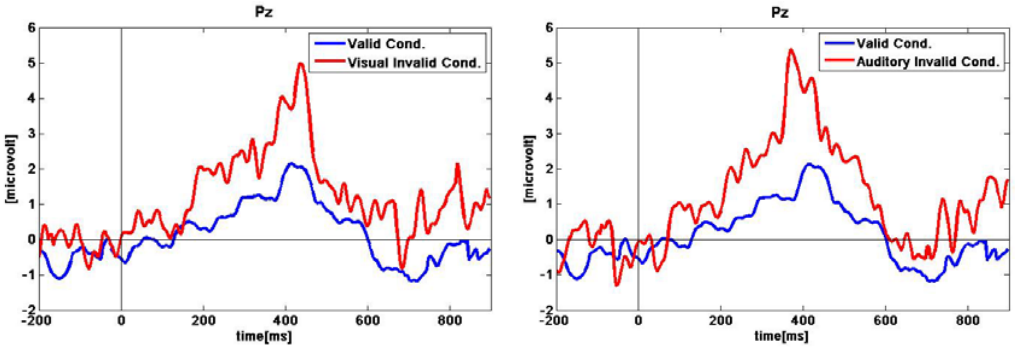

Figure 3.13: Average over all the measured subjects of EEG signals in the Pz point. (Left: Valid (blue line) and invalid (red line) visual condition; Right: Valid (blue line) and invalid (red line) auditory condition).

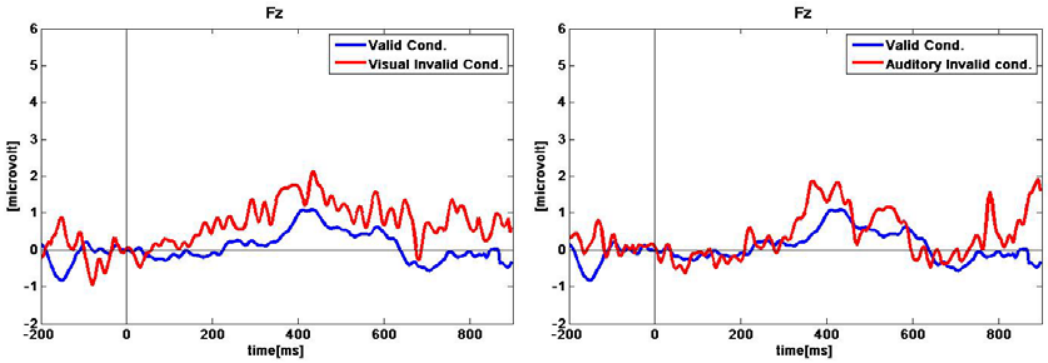

Figure 3.14: Average over all the measured subjects of EEG signals in the Fz point. (Left: Valid (blue line) and invalid (red line) visual condition; Right: Valid (blue line) and invalid (red line) auditory condition).

in the decision making process to distinguish between the three conditions.

At last the EEG signal was analyzed in the frequency domain. EEG frequency analysis was implemented through an autoregressive (AR) batch modeling, performed on the electrode Fz with time windows of 2 s, overlap 50, in order to obtain a stationary signal with a frequency resolution of 1 Hz. Then, by an automatic spectral decomposition, based on a residual integration algorithm [30], the main two EEG rhythms were obtained (8-13,5 Hz Alpha, 13,5-30 Hz Beta).

ECG signal

The RR series were extracted from the ECG derivation. They were re-sampled in order to obtain one value each second of activity, and to have the same sampling rate of EEG and TD-fNIRS signals.

Behavioral data

The 16 subjects committed an average of 0.13±0.49 Visual Omission errors (0.13 missing answers on 15 visual target stimuli), 0.47±0.63 Auditory Omission errors (0.47 missing answers on 15 auditory target stimuli) and an average of 11.63±24.42 Commission errors (all kinds), corresponding to 11.63 wrong answers during all the divided attention test. Subjects answered to the visual target stimuli in 649.55±129.27 ms and to the auditory target stimuli in 698.14±141.30 ms. Behavioral results showed a higher number of

errors in response to the Auditory stimuli rather than to the Visual ones, and a longer response time concerning auditory stimuli. The two stimuli were always presented simultaneously, in order to enhance the duality of the task. The results concerning the response time are in opposition to previous studies that reported a longer time of response to Visual stimuli [21, 29]. It could be due to a not perfect equalization in the stimuli difficulty.

Correlations

After modeling the task as a square wave, high during the test blocks and low during the rest ones, we calculated the Cross Correlation Function (CCF) between it and Alpha and Beta power rhythms, RR series, HF component of depth and surface O_2Hb and HHb signals. Mean value was subtracted from all signals and they have been normalized by the standard deviation. We evaluated the temporal shift between each couple of signals for which the CCF had maximum absolute value and we extracted the corresponding CCF value and the p-value. Depending on the couple analyzed, we considered a maximum or a minimum of correlation. Figure 3.15 shows the grand average

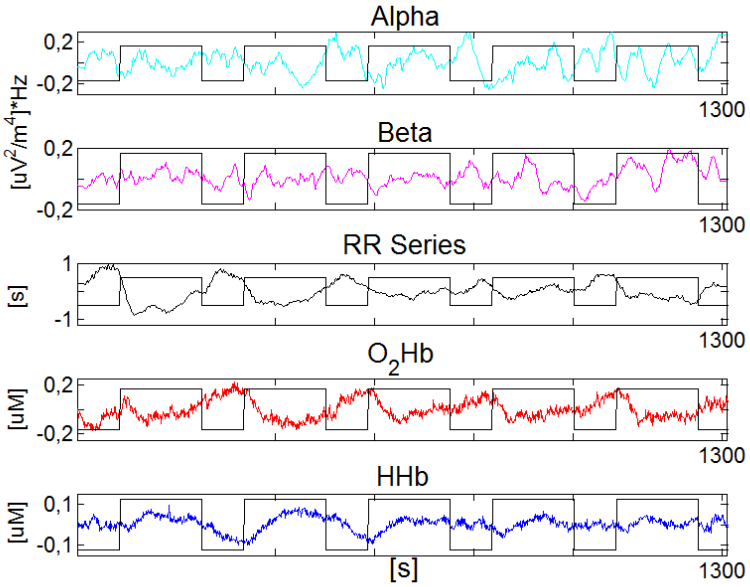

Figure 3.15: Grand Averages of all the acquired signals from all the subjects. From top: power of Alpha and Beta rhythm, RR series, O_2Hb and HHb depth signals.

of signals (EEG Alpha and Beta rhythms, RR series, TD-fNIRS depth signals of Oxy and Deoxy hemoglobin) acquired from all the 16 subjects. The CCF between Alpha rhythm and the task was negative for 11 on 16 subjects (Alpha power increased during the resting periods, mean value -0.31±0.13, $p << 0.001$). The CCF between Beta rhythm and the task was positive for 10 subjects but the mean delay for which the CCF reached its maximum value (17.6±20.21 s) was considered too long to represent a neuronal response, so Beta rhythm was excluded from following analysis. RR series showed a strong modulation by the square wave task. Correlation with the task was negative for all the subjects (that means that RR period decreased during test periods and increased in the resting periods), mean value -0.43±0.23, $p << 0.001$. The CCF with the task was calculated only for HF components of the TD-fNIRS depth and superficial signals. All the p-values resulted $<< 0.001$. The correlation between O_2Hb depth signals and the square wave task was negative for 12/16 subjects. The mean value of CCF minima between the two pads was -0.41±0.6. The CCF of HHb depth signals and the task had a positive value for 11/16 subjects, mean value 0.43±0.17. LF TD-fNIRS depth signals showed a general increase of O_2Hb, opposed to a decrease in HHb. The correlation for the surface signals showed a larger variability among the subjects and between the two pads of the same subject, with respect to the depth ones. We identified a group of 8 subjects (50% of the investigated population) showing the same time course for all the CCF.

We then evaluated the mean delay between each signal and the task, in order to identify the time of response of each physiological district (neuronal, systemic, and hemodynamic) to the divided attention task. The mean delays among the 8 subjects and the correspondent values of CCF are shown in Figure 3.16 (left). Figure 3.16 (right) is representative of the temporal cascade of responses. The results of CCF between each signal and the task showed that: the power of Alpha rhythm increased during the rest period, as found in previous literature [24], and the heart rate increased during test blocks, causing a negative correlation of RR series with the task [31]. The CCF of high frequency depth TD-fNIRS signals requires a more thorough analysis. The HF component appeared to be strictly modulated by the alternation of test and rest blocks and it mirrors the metabolic consumption of oxygen that takes place during test periods. When the subject is required to execute a cognitive task, there is an oxygen consumption, reflected in a decrease of O_2Hb concentration and an increase of HHb one. The LF component trend, confirming previous findings [32], is indeed representative of the amount of oxygen supply that also takes place when carrying out a cognitive task. The subsequent evaluation of the time of activation of the different responses put into evidence the presence of a cascade of responses. Figure

Signals	CCF	Delay [s]
Alpha - Task	-0,26 ± 0,09	0,63 ± 13,87
RR - Task	-0,48 ± 0,19	12,00 ± 6,93
O_2Hb - Task	-0,43 ± 0,17	21,06 ± 21,77
HHb - Task	0,36 ± 0,29	27,56 ± 28,93

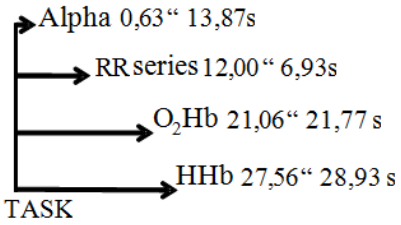

Figure 3.16: Left: table of CCF and mean delay between signals and task. Right: temporal responses' cascade.

3.15 shows an almost instantaneous response of CNS, represented by Alpha rhythm activation, followed by the response of ANS (RR series) and, at last, by the hemodynamic response, represented by changes in O_2Hb and HHb. The average response times are consistent with values previously reported [23, 31].

Finally we considered the CCF between couple of signals, in order to evaluate the amount of shared information. The signs of the correlation values are consistent with the results of the correlation of each signal with the task. As shown in Figure 3.16, the highest correlation values are the ones between RR series and TD-fNIRS depth signals. It suggests that the signals of cardiovascular nature are the most influenced by the cognitive task. The presence of a correlation between RR series and O_2Hb surface could be representative of a common autonomic influence on the two signals. On the contrary we do not find any strong correlation between RR series and superficial HHb. It seems, then, that the RR series correlate only with O_2Hb, probably due to the fact that changes in heart rate cause modulations in arterial compartment. O_2Hb results more affected by these changes, if compared to HHb, as it is the most representative signal of the arterial compartment behavior [33]. The absence of a strong correlation between RR series and Alpha rhythm could be explained with the different origin of the two signals, respectively ANS and CNS. It seems, then, that there is no mirroring of cardiac activity in EEG. The time courses of Alpha rhythm and TD-fNIRS depth signals show the presence of a decrease in neuronal synchronization (reduction in Alpha power) and a reduction in O_2Hb concentration (increase in HHb) during the test period. These results could mirror a metabolic economy: synchronized membrane oscillations could, in fact, be more energetically advantageous. That could explain why there is an increase in synchronization in rest periods, coupled with metabolic consumption. The higher correlation of Alpha and HHb, compared to O_2Hb, is also reported in reference [24].

3.2.3 Conclusion and perspective

We tested the feasibility of simultaneous EEG and TD-fNIRS measurements, demonstrating that the combination of two different neuroimaging modalities can help a better understanding of the cognitive processes during divided attention tasks. The activation of a cascade of responses confirms the presence of the involvement of several systems, each one characterized by a different time delay respect to the task: instantaneous neural electrical response, autonomic response and a slower hemodynamic response. The correlations between couple of signals show that the different responses to the task are not independent. In fact, considering Alpha rhythm, RR series and O_2Hb and HHb, a desynchronization of Alpha rhythm, a reduction in O_2Hb and an increase in HHb and Heart Rate during test blocks are noticed. These phenomena somehow embed metabolic consumption information and show dynamics clearly different from what happens during rest phases. Considered these preliminary results, the proposed task seems to be a valuable tool for the investigation of brain activation during divided attention task. This cognitive function seems to be a valid candidate for studying neurovascular coupling, even if the big variability of physiological signals, mirrored in high standard errors, makes this aim really hard and prevents the research from finding the same trend in the whole studied group.

3.3 TD-fNIRS during Electrical muscle stimulation (EMS)

Near-infrared spectroscopy is not only well applied in the neuroscience field, but has also been used in exercise physiology and clinical medicine for non-invasive investigation of muscle oxygenation and hemodynamics during exercises [34, 35, 36, 37]. In particular, during studies on muscle, it's possible to represent, through the typical TD-fNIRS parameters, the muscle utilization of the oxidative metabolic system. The oxygen saturation reflects the dynamic balance between O_2 supply and demand by the muscle and can be considered a measure of the energy consumption for muscle force production [38]. tHb is instead related to the changes in muscle microcirculation blood volume and it is considered a qualitative indicator of changes in local muscle blood flow. Of particular interest is the study of muscle behavior during electrical stimulation, in order to understand muscle's hemodynamic changes when the current is varied through different thresholds. Electrical Muscle Stimulation (EMS) refers to the application of electrical current to the skin to evoke action potentials in both motor and sensory fibers. This stimulation affects, at first, the muscles and for this reason it is commonly employed during the treatment of muscle atrophy, pain treatment, endurance training and build-up of muscle mass [39, 40]. EMS can also indirectly activate peripheral sensory axons that send pain signals from the muscle to the sensory, motor and association cortices [41, 42]. The purpose of this measurement campaign was to investigate both muscle oxygenation and regional cortical activities during EMS at different thresholds on healthy subjects. The study was possible thanks to the collaboration with the "Institute of Health & Biomedical Innovation", Queensland University of Technology, Brisbane, Australia and the "Department of Health Sciences", University of L' Aquila, L' Aquila, Italy. In addition, the same protocol was undertook with a CW instrument at the Movement to Health Laboratory, University of Montpellier-1, France. Data analysis is still in progress, for this reason only preliminary results on muscle, from the time domain instrument, will be presented.

3.3.1 Materials and methods

EMS

EMS was carried out with the portable system CEFAR Physio 5. The device is a microcontroller-based system with 2+2 current-regulated stimulation channels and is controlled with a chip card. The wrist extensor muscles were stimulated with a pair of 5X5 cm self-adhesive electrodes. The negative electrode was located on the motor point of the right extensor muscles and

the positive one on the distal end of the muscle near the wrist (figure 3.17(a)). Symmetric, biphasic and charged balanced rectangular pulse shapes were applied. The depolarizing pulses had a width of 200 μs and frequency of 30 Hz.

TD-fNIRS systems

To perform measurements on the arm muscles, our instrument in the 2X4 version was employed. We used one source channel and two detection channels, at 2 and 4 cm of interfiber distance. We placed the probes on both the arms: on the right arm to monitor the hemodynamic changes during EMS stimulation, on the left to verify the stability of the instrument and the absence of systemic changes. See figure 3.17(b), for details about muscle probes positioning. For the functional brain mapping a 16 channels TD-fNIRS instrument (figure 3.18(a)), previously developed at our department, was applied [43]. The 2X16 channels covered the bilateral sensorimotor and prefrontal cortices, as shown in figure 3.18(b). The green, red and blue dots represent respectively the detection, injection and measurements points.

Physiological monitoring

ECG, breathing rate and skin conductance were also monitored during the whole experiment by means of the Flex Comp Infiniti encoder (Thought Technology Ltd., Canada).

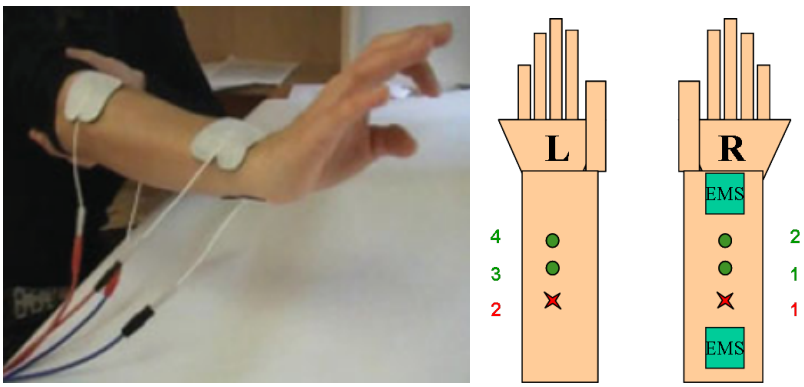

(a) (b)

Figure 3.17: (a) EMS electrodes positioning (b) EMS and TD-fNIRS probe placement in the arms. In red the injection points, in green the detection ones. L= left; R= right.

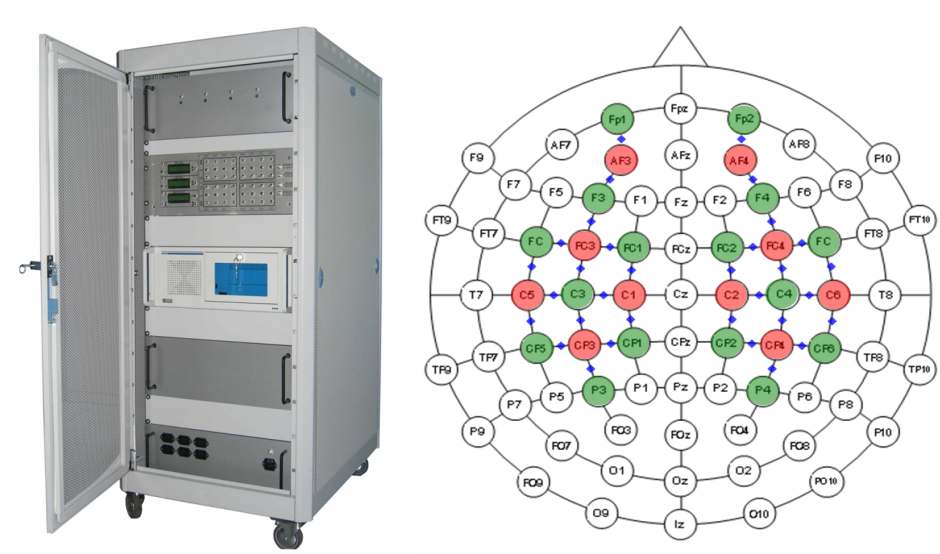

(a) (b)

Figure 3.18: (a) 2x16 TD-fNIRS instrument (b) Probe placement on the head. Green, red and blue dots are respectively the detection, injection and measurement points.

The complete experiment set-up is shown in figure 3.19.

Figure 3.19: Complete experimental set-up.

Experimental Protocol

Nine healthy volunteers, 39.2±13 years, took part at this study, which was approved by the Institutional Review Board (IRB). At least 10 min prior to the EMS protocol, maximal tolerated intensity was determined for each subject by using a series of no more than 6 to 8 brief (3-5 seconds) electrically stimulated contractions with increasing intensity. After each increase in intensity that included a visibly stronger contraction, the participants were asked if they could tolerate any further increase in intensity. In this way was possible to determine the maximal tolerated intensity (MTI), as the intensity of stimulation received when the subjects was no more able to tolerate an increase in intensity. The measurement protocol consisted in 10 s of baseline, 40 s of task (repeated 10 times) and 10 s of recovery for a total experiment length of 420 seconds. Each 40 seconds task block was composed of 10 s baseline, 20 s of experiment and other 10 s of recovery. We undertook six different experiments per each subject:

1. determination of the MTI;

2. voluntary movement of the right wrist, with a frequency of 1 s, in order to simulate the same movement made during the stimulation (VOL);

3. EMS at 10% of the MTI (10%);

4. EMS at 50% of the MTI (50%);

5. EMS at 100% of the MTI (100%);

6. EMS over 100% of the MTI (over);

The acquisition time was set at 1 s, 0.5 each wavelength. The subjects were asked to perform the experiments with closed eyes in a quiet environment. During each experiment, pain rating was monitored using a visual analogue scale (VAS).

3.3.2 Data analysis and preliminary results

In this paragraph only preliminary results about the physiological data and muscle oxygenation will be shown.

Physiological parameters

The skin conductance (SC) is the measure of the skin capability to conduct electricity. This is directly correlated with the sympathetic nervous system activation, which changes the levels of sweat in the glands (ionic sweat is more conductive than dry skin, which causes an increase in bulk conductivity) and has been shown to be linked to the measure of emotion, arousal, and attention. The emotions can have different origin. In experiment like the one recorded, if the SC has a high value, it means that the subject has a high level of stress, due mainly to the pain of EMS. Typical values of SC, for a relaxed person, are around 2 μS, but this value can vary, depending on environment factors, the daily level of stress and different skin types. Any stimulus capable of an arousal effect can evoke the response and the amplitude of the response is more dependent on the surprise effect of the stimulus than on the physical stimulus strength. In graph (a) of figure 3.20 it is clear how increasing the power of the EMS, the skin conductivity increases its value showing an increased level of stress. It is also evident in the figure that there is a modulation of the SC inside each experiment, which reflects the 10 repeated stimulation tasks. During each repetition we observe an initial increase of the SC, which, after a peak, decreases, suggesting a gradual adaptation of the subject to the task itself. Also the decrease in the amplitude of the SC signal through the 10 repetitions, well explain this habituation to the event, according to the fact that the SC amplitude depends primarily on the surprise effect and not on the stimulus intensity per se.

From the recorded ECG signal, the R-R series were extracted and the heart rate (HR) calculated with an algorithm implemented in a custom-made Matlab program. In graph (b) of figure 3.20, the behavior of HR for a typical subject is shown.

With a similar procedure as that used for HR calculation, from the respiratory signal it is possible to extrapolate the respiratory rate (RR). This signal has the same behavior of the HR, as shown in graph (c) of figure 3.20. The trend of these two signals underline that the tasks don't affect the respiratory and the cardiac outputs. Therefore the changes in SC are effectively due only to an emotional component.

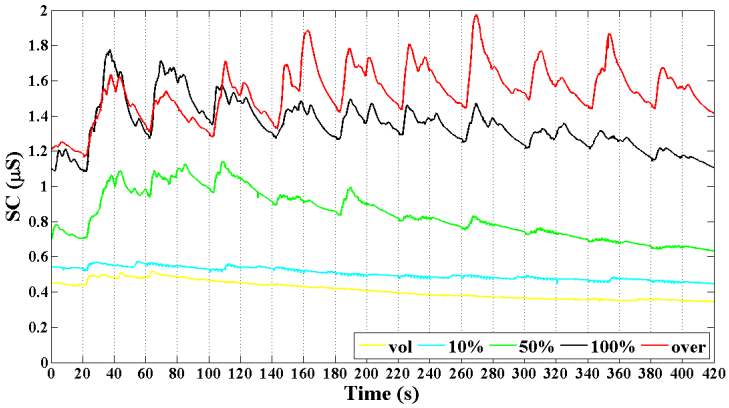

(a) Skin Conductance.

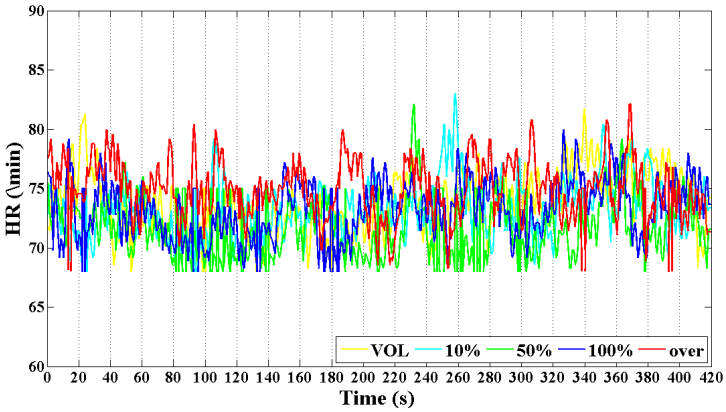

(b) Heart Rate.

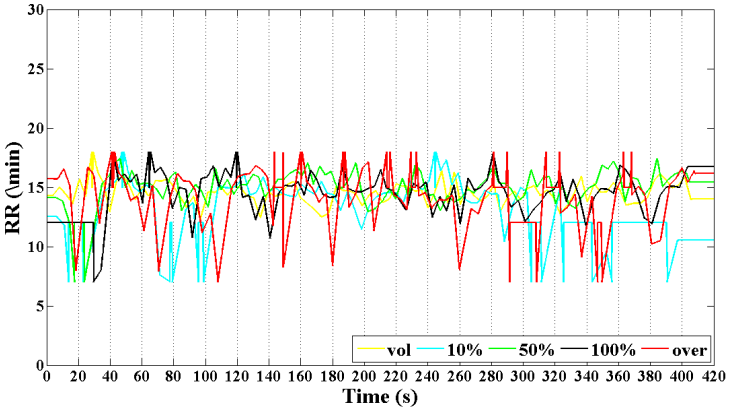

(c) Respiratory Rate.

Figure 3.20: Physiological parameters during the five experiments.

TD-fNIRS on muscle

TD-fNIRS signal on muscle was acquired with a sampling rate of 1 s. A correction method based on the use of temporal windows (1500-5000 ps) as explained in paragraph 1.5.1, was applied, in order to separate the contribution coming from the superficial layers of the muscle tissue and the deeper ones. All the following considerations were done on the depth signal and for 2 cm interfiber distance. At first we calculated the absolute values of the oxy-hemoglobin (O_2Hb), deoxy-hemoglobin (HHb), oxygen saturation (SO_2) and total-hemoglobin (tHb) during the 10 sets of voluntary movement (VOL), EMS at 10%, 50%, 100% of the MTI and over the maximum pain threshold (over). In figure 3.21 the typical behavior of these hemodynamic parameters for a typical subject is shown. In all the four graphs, it's clear a modulation of the signal due to the ten different electrical stimulations over

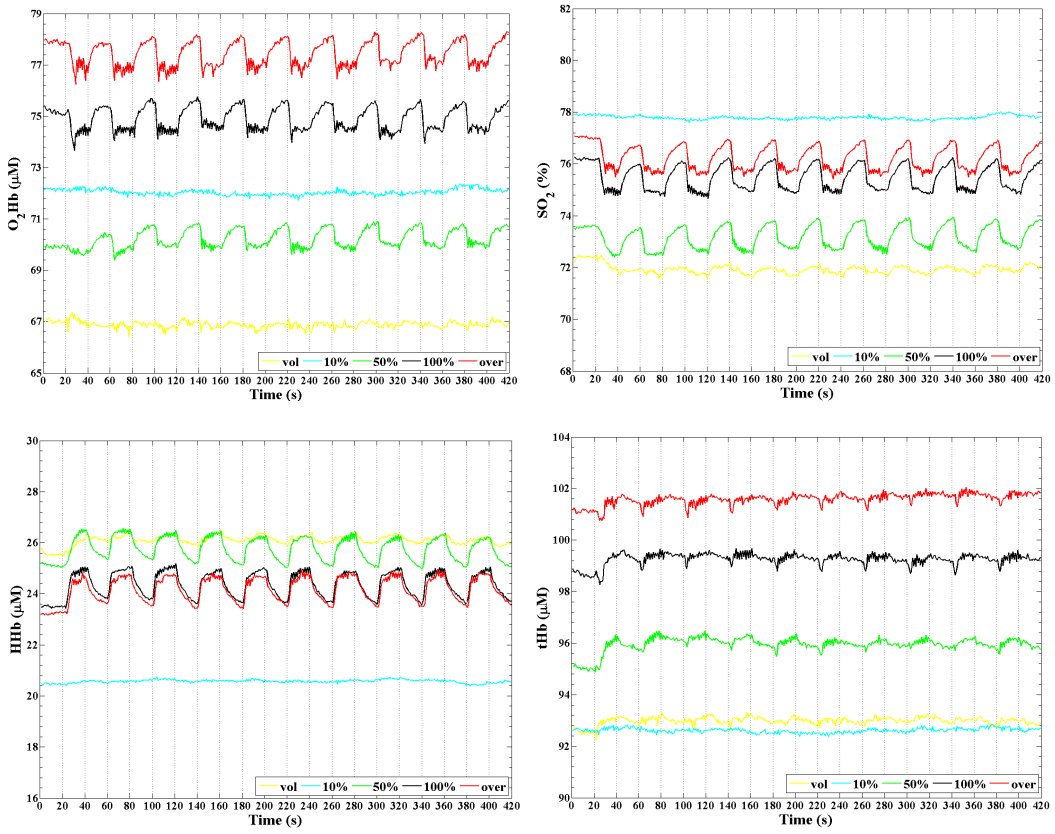

Figure 3.21: Absolute values of the hemodynamic parameters during the five experiments.

the ten sets. The typical behavior for O_2Hb, SO_2 and HHb is to quickly decrease (O_2Hb and SO_2) or increase (HHb) from baseline levels during the beginning of the contraction phase, then they reach a plateau (O_2Hb), minimum (SO_2) or maximum (HHb) value at the end of the tenth contraction, and during the relaxation phases they increase (O_2Hb and SO_2) or decrease (HHb) towards baseline level. The tHb shows a different behavior inside each stimulation period: its value firstly decreased then immediately afterwards increased again to reach, maximum levels near the end of the tenth contraction. The O_2Hb, SO_2 and HHb results indicate that the metabolic demand for oxygen increased during the 10 contractions of each set, and suggest that muscle fibers under the TD-fNIRS probes were activated; during the recovery periods, the oxygen supply was increased above oxygen demand. The reason for the immediate decrease in tHb is that at the start of the first contraction the increased intramuscular pressure causes ischemia in the muscle tissue, which expels blood volume away from the region of interest, then over the other contractions, blood flow/volume is increased to meet the increased metabolic demand of the muscle tissue. Going through the five experiments, we notice that the signal due to the 10% of the MTI is quite flat, suggesting that the EMS at 10% minimally activated muscle fibers under the TD-fNIRS probe. Increasing the amplitude of the stimulation current intensity, the hemodynamic signal amplitudes increased as well. To better understand this behavior we calculated the relative variations (Δ) of the four hemodynamic parameters with respect to the baseline (figure 3.22). The baseline was calculated as the average value of the 9 seconds before each stimulation period and then subtracting it from the relative task block (10 s baseline, 20 s of stimulation and other 10 s of recovery). From graphs in figure 3.22 we can see that effectively the amplitude of the signals is higher if the stimulation current intensity is higher as well. The EMS at 10% shows a minimum for SO_2 at -0.15%, which is smaller than the minimum SO_2 levels attained during VOL and other EMS conditions, which confirms the suggestion of the minimal muscle activation during this condition. By increasing the stimulation current intensity we notice an increase of the hemodynamic signal amplitudes, which shows an increase of the muscle activation at that current intensity. When EMS contractions were performed at maximal pain threshold intensities (100% and over) SO_2 decreased quickly from baseline levels to reach minimum SO_2 level of -1.4%. SO_2 increased gradually towards baseline over the 20 s recovery periods to reach maximum level of 0.2% above baseline. These results would indicate that all muscle fibers under the TD-fNIRS probe were maximally activated, and that further increases in current amplitude did not increase metabolic demand, which suggests that no further muscle fibers were activated, even though current amplitudes and pain

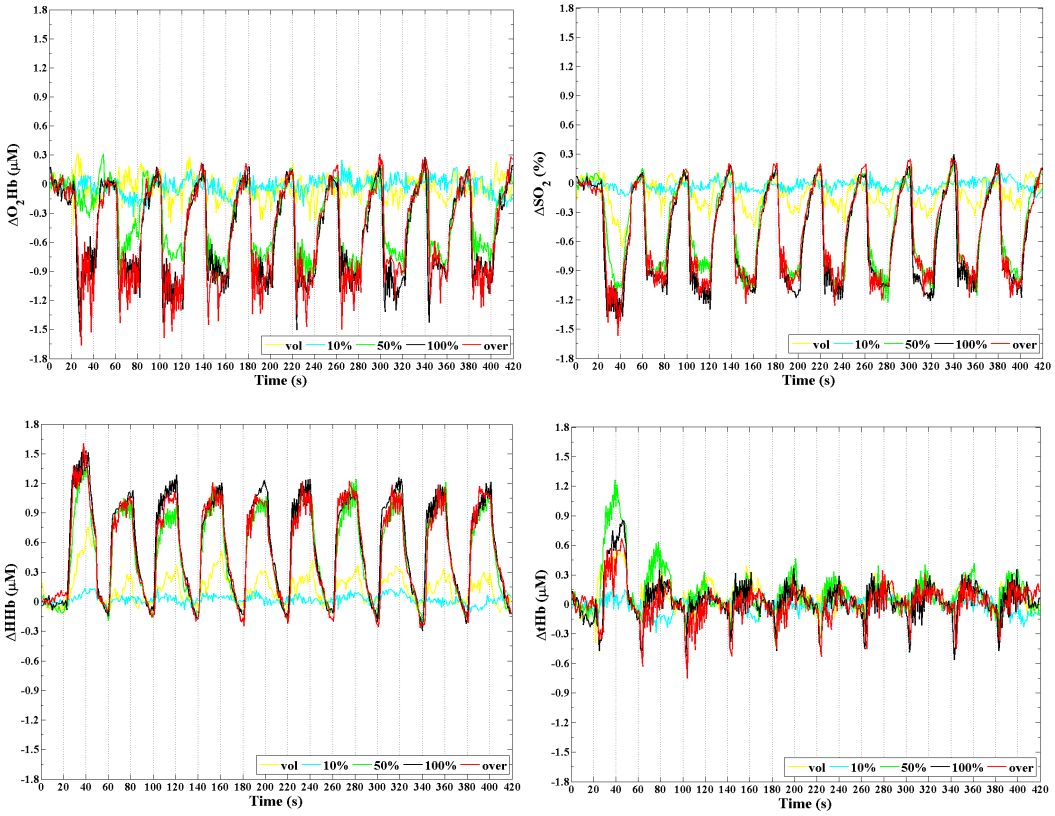

Figure 3.22: Relative changes (Δ) of the hemodynamic parameters during the five experiments.

levels increased over the 10 sets. It's also interestingly to notice how, at 50%, nearly all muscle fibers under the NIRS probes were activated at a lower current amplitude (17 mA vs. 33-55 mA) and pain level, compared to the MTI condition. If we then observe how the signal changes in the different sets of the same experiment, we can observe that the first contraction of each experiment is the one that causes the greatest changes in amplitude with respect to the other contractions, like to underline an adaptation of the muscle to the stimulation.

We then computed the maximum, the minimum and the average value of all the hemodynamic parameters during each stimulation and rest period. These time intervals were not taken as fixed, i.e. determined by the measurement protocol, but were calculated considering that a stimulation period ends when the increase or decrease of the hemodynamic parameter, reaches maximum/minimum levels. We calculated them for both the absolute and the

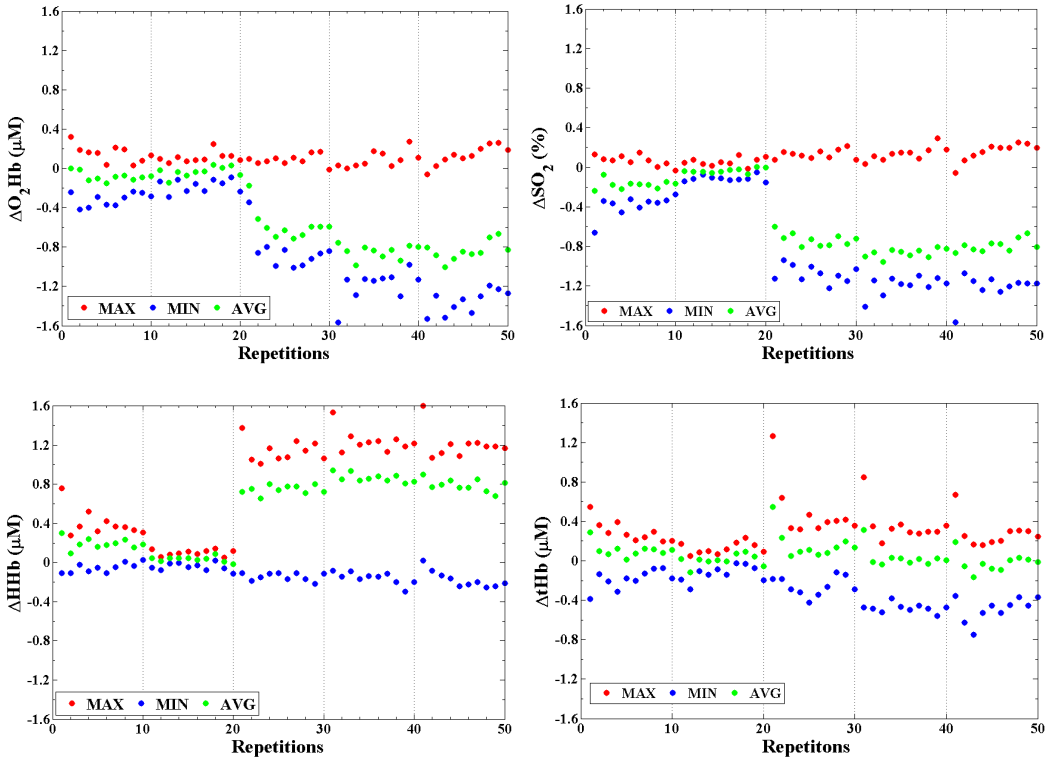

Figure 3.23: Maxima, minima and average values during the five experiments (intervals between the vertical lines).

relative values. In graph 3.23 an example of the values, calculated from the relative data, obtained for the typical subject over all the sets of stimulation and all the experiments, is shown. The vertical lines divide the five experiments, from the left to the right: VOL, 10%, 50%, 100% and over threshold. The points represent the 10 sets of each experiment. The maxima, minima and average values inside one experiment are quite constant when the movement is voluntary or the stimulation is low (10%). When the stimulation is higher (50%-100% and over), the first set of ten stimulation causes always a peak in the hemodynamic parameters with respect to the nine following sets. This is probably due to the fact that, when the stimulation is high, the muscles react strongly to the first solicitations in comparison with the following ones. For what concern the behavior through the different experiments, we can observe that increasing the stimulation, the maxima (minima) of the O_2Hb and SO_2 (HHb and tHb) remains quite stable, while the minima and the average value (maxima and average value) of the O_2Hb and SO_2 (HHb

and tHb) decrease (increase) their values. Also in literature we find examples where the relative changes respect to the baseline during the stimulation are more significant than the ones due to the voluntary movement, see reference [44].

3.3.3 Conclusion and perspective

Preliminary results for a subject show differences in elbow extensor muscle oxygenation between voluntary and different current intensities of EMS. Further analysis are necessary to extrapolate group statistics and correlation with the physiological parameters and the pain scale. Analysis on data coming from the left arm and from the detection channel on the right arm at 4 cm interfiber distance are still in progress. The analysis of the TD-fNIRS signal coming from the brain is also in progress in order to understand the interaction between cerebral and muscular response to the fatigue. It will be also interesting to compare our TD-fNIRS data with the ones coming from a CW-instrument, recorded in Montpellier during the same measurement protocol.

Bibliography

[1] A.P. Shepherd, P.A. Öberg, Laser Doppler flowmetry 1990.

[2] H.D. Kvernmo, A. Stefanovska, M. Bracic, K.A. Kirkeboen, K. Kvernebol, Microvasc Res, 56:173-82 1998.

[3] P. Kvandal, S.A. Landsverk, A. Bernjak, A. Stefanovska, H.D. Kvernmo, K.A. Kirkeboen, Microvasc Res, 72(3):120-27 2006.

[4] C.J. Porth, V.S. Bamrah, F.E. Tristani, J.J. Smith, Heart Lung., 13 (5) 507-518 1984.

[5] J.H.G.M. Klaessens, R.G.M. Kolkman, J.C.W. Hopman, E. Hondebrink, K.D. Liem, W. Steenbergen, F.F.M. de Mul, J.M. Thijssen, Physiol Meas, 24(4):35-40, 2003.

[6] F. Aletti, R. Re, V. Pace, D. Contini, E. Molteni, S. Cerutti, A. M. Bianchi, A. Torricelli, L. Spinelli, R. Cubeddu, G. Baselli, Computers in biology and medicine, 13 July 2011.

[7] G. Baselli, F. Aletti, V. Pace, E. Molteni, S. Cerutti, D. Contini, R. Re, A. Torricelli, L. Spinelli, R. Cubeddu, ESGCO (European Study Group on Cardiovascular Oscillations), Procceding, 12-14 April 2010.

[8] H. Peng, V. Matchkov, A. Ivarsen, C. Aalkjaer, H. Nilsson, Circ. Res. 88, 810815, 2001.

[9] H. Nilsson, C. Aalkjaer, Mol. Interv. 3 (2), 7989, 2001.

[10] M. Benedicic, A. Bernjak, A. Stefanovska, R. Bosnjak, Microvasc. Res. 74 (1), 4550, 2007.

[11] M. Tsuji M, J.P. Saul, A. du Plessis, E. Eichenwald, J. Sobh, R. Crocker, J.J. Volpe, Pediatrics, 106:62532, 2000.

[12] K.M. Brady, J.K. Lee, K.K. Kibler, P. Smielewski, M. Czosnyka, R.B. Easley, R.C. Koehler, D.C. Shaffner, Stroke, 38(10):2818-25, 2007.

[13] A. Stefanovska, M. Bracic, H.D. Kvernmo, IEEE Trans. Biomed. Med. Eng., 1230-39, 1999.

[14] Heart rate variability. Standards of measurement, physiological interpretation, and clinical use. Task Force of the European Society of Cardiology and the North American Society of Pacing and Electrophysiology. Eur Heart J.;17(3):354-81, 1996.

[15] A. Malliani, Principles of Cardiovascular Neural Regulation in Health and Disease, Kluwer Academic Publishers, 2000.

[16] S. Boden, H. Obrig, C. Khncke, H. Benav, S.P. Koch, J. Steinbrink, Neuroimage, 100-107, 2007.

[17] S. Fazli, J. Mehnert, J. Steinbrink, G. Curio, A. Villringer, K.R. Mller, and Be. Blankertz, Neuroimage, 59-1, 519-529, 2012.

[18] Y. Ishii, H. Ogata, H. Takano, H. Ohnishi, T. Mukai, T. Yagi, EMBS, Vancouver, 2008.

[19] A. Jelzow, S. P. Koch, H. Wabnitz, J. Steinbrink, H. Obrig and R. Macdonald, in Digital Holography and Three-Dimensional Imaging, OSA Technical Digest (CD), Miami, 2010.

[20] K. Nebel, H. Wiese, P. Stude, A. De Greiff, H. C. Diener and M. Keidel, Cog. Brain Res. 25, 760-776, 2005.

[21] R. Loose, C. Kaufmann, D.P. Auer and K.W. Lange, Hum. Brain Mapp. 18, 249-259, 2003.

[22] H. Obrig, H. Israel, M. Kohl-Bareis, K. Uludag, R. Wenzler, B. Mller, G. Arnold and A. Villringer, Neuroimage, 17(1): 1-18, 2002.

[23] M. Izzetoglu, S. C. Bunce, K. Izzetoglu, B. Onaral, K. Pourrezaei, IEEE Eng. Med. Biol., 26(4):38-46, 2007.

[24] P. Moosmann, P. Ritter, I. Krastel, A. Brink, S. Thees, F. Blankenburg, B. Taskina, H. Öbrig and A. Villringer, NeuroImage, 20:145-158, 2003.

[25] D. Contini, E. Molteni, R. Re, M. Caffini, A. M. Bianchi, L. Spinelli, G. Baselli, S. Cerutti, R. Cubeddu and A. Torricelli, in Biomedical Optics, OSA Technical Digest (CD) (Optical Society of America, 2010), paper BSuD72, 2010.

[26] V. Bari, P. Calcagnile, E. Molteni, R. Re, D. Contini, L. Spinelli, M. Caffini, A. Torricelli, R. Cubeddu, S. Cerutti and A. M. Bianchi, Conf. Proc. IEEE Eng. Med. Biol. Soc.:1403-1406,2011.

[27] P. Zimmermann, B. Fimm, Manual for the attention assessment test battery, Psytest, Herzogenrath, 1992.

[28] M. Butti, D. Contini, E. Molteni, M. Caffini, L. Spinelli, G. Baselli, A. M. Bianchi, S. Cerutti, R. Cubeddu and A. Torricelli, Phys. Med. Biol. 36 (9), 4103-4114, 2009.

[29] J. Hohnsbein, M. Falkenstein , J. Hoormann and L. Blanke, Electroenceph. Clin. Neurophysiol., 78 (6), 438-46, 1991.

[30] G. Baselli, S. Cerutti, S. Civardi, F. Lombardi, M. Malliani, M. Merri, M. Pagani, G. Rizzo, Int J. of Bio-Medical Comp., 20(1): 51-70, 1987.

[31] M. Moody, R.B. Panerai, P.J. Eames, J.F. Potter, Am. J. Physiol. Regulatory Integrative Comp Physiol, 288:1581-1588, 2005.

[32] T. Schreppel, J. Egetemeir, M. Scheckelmann, M.M. Plichta, P. Pauli, H. Ellgring, A. J. Fallgatter, M.J. Herrmann, Neuropsychobiology, 57(4):188-193, 2008.

[33] M.A. Franceschini, S. Fantini, J.H. Thompson, J.P. Culver, D.A. Boas, Psychophysiology, 40:548-560, 2003.

[34] R. Boushel and C.A. Piantadosi, Acta Physiol. Scand, 168, 615-622, 2000.

[35] T. Hamaoka, K. K. McCully, V. Quaresima, K. Yamamoto, and B. Chance,J. Biomed. Opt. 12, 062105, 2007.

[36] S. Ferrante, D. Contini, L. Spinelli, A. Pedrocchi, A. Torricelli, F. Molteni and G. Ferrigno, JBO, 14(4), 044011, 2009.

[37] M. Ferrari, M. Muthalib and V. Quaresima, Phil. Trans. R. Soc. A, 369, 114, 2011.

[38] K. K. McCully and T. Hamaoka, Exerc. Sport Sci. Rev. 28, 123127, 2000.

[39] L. Bax, F. Staes and A. Verhagen, Sports Med 35: 191-212, 2005.

[40] M. Vanderthommen and J. Duchateau, Exerc Sport Sci Rev 35: 180-185, 2007.

[41] A. Blickenstorfer, R. Kleiser, T. Keller, B. Keisker, M. Meyer, R. Riener and S. Kollias, Human Brain Mapping, 30:963-975, 2009.

[42] M. Muthalib, M. Ferrari, V. Quaresima and K. Nosaka, in ISOTT, Ascona, Switzerland, 2010.

[43] D. Contini, L. Spinelli, M. Caffini, L. Zucchelli, A. Tosi, R. Cubeddu and A. Torricelli, Biomedical Optics and 3-D Imaging: OSA Optics and Photonics Congress, Miami, Florida, USA, 2010.

[44] M. Muthalib, H. Lee, G. Y. Millet, M. Ferrari and K. Nosaka, J. Appl. Physiol., 110: 1390-1399, 2011.

CHAPTER 4

A compact and wireless CW-NIRS instrument with integration of physiological sensors.

During a six months period, I worked at the "Abramson Center for Future of Health" (Houston, TX), a joint effort of the University of Houston College of Technology and the Methodist Hospital Research Institute. Here I contributed to the development of a CW-NIRS prototype, which, to our knowledge, is the only portable NIRS equipment which is capable of measuring absolute concentrations of hemoglobin in real-time. In addition to the NIRS probe, we used a cardiovascular sensing system that includes an electrocardiogram (EKG) and a photoplethysmograph (PPG) sensor. Being a one-channel instrument is particularly suitable for measurement on muscles, where an imaging system is not required. With the integration of EKG and PPG, this NIRS instrument is suitable for providing a complete description of the exercise status of the human both in terms of systemic hemoglobin supply and of skeletal muscle hydration and cardiac output.

In paragraph 4.1 the complete instrument set-up is described. In paragraph 4.2 and 4.3 an *in vivo* application during muscle exercise and preliminary experimental results are respectively presented. The final goal of the measurement campaign is to find new physiological indexes and correlations between them, to better identify and quantify the phenomenon of the muscular fatigue. These indexes can be applied in the cardiac rehabilitation, in the muscular training and in the evaluation of muscle performances during spaceflight. The measurement campaign was possible also thanks to the collaboration with the "Laboratory of Integrated Physiology" of the University of Houston.

4.1 System set-up

In Figure 4.1(a), a picture of the system is presented. As shown in the picture, the system is provided with four different units:

1. central unit: provided with the command buttons and sensors connectors.
   It has a rechargeable battery that guarantee an autonomy of about four hours. It works also as temporal data storage unit. Data are then sent through a wireless communication system to a data hub;

2. Fingertip photoplethysmography probe [1].
   Photoplethysmography (PPG) is an optical measurement technique for detecting blood volume changes in the microvascular bed of tissue. This technology exists in common medical devices like pulse oximeters, vascular diagnostics and digital beat-to-beat blood pressure measurement systems. PPG technology employs a light source to illuminate the tissue and a photodetector to measure the small variations in light intensity associated with changes in perfusion in the sampled volume.

3. NIRS PROBE, figure 4.1(b).
   As light sources, three diode lasers at 685 nm, 830 nm and 980 nm, are used. Each diode laser has a power <1 mW to guarantee a safe emission

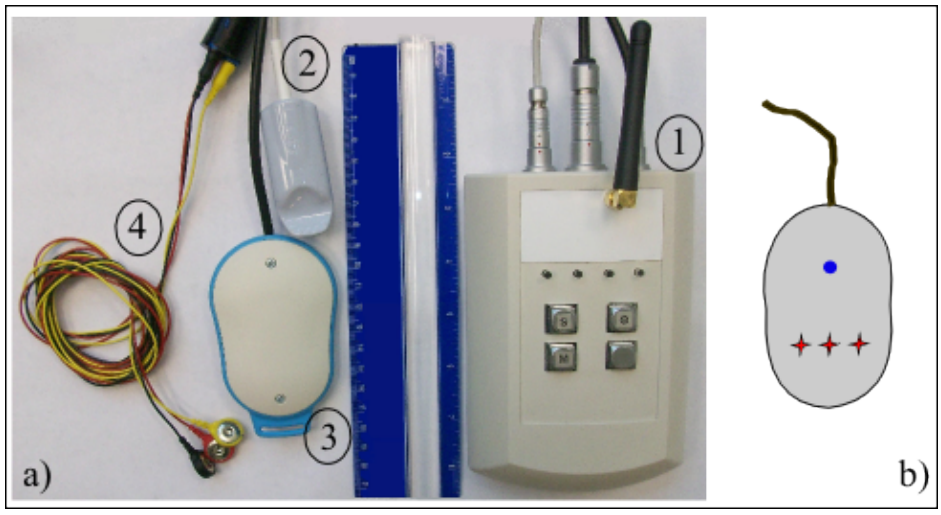

Figure 4.1: (a) Instrument set-up. (b) NIRS probe detail: the blue dot is the detector point and the red stars are the three injection points.

compliant to ANSI and EC laser safety standards. Light is recollected by means of a p-n photodiode at a distance of 3 cm from the sources. In 20 ms all the three wavelengths are consequentially acquired, sent to the computer, and the optical coefficients are computed. The laser sources and the detector are both built-in a polymeric plastic probe for a total dimension of 9 cm.

4. 3-lead electrocardiogram [2].
   For the measurements, adhesive pre-gelled electrodes suitable for acquisition with the subject in movement, were employed. From the EKG signal is possible to extrapolate the heart rate or to monitor the electrical activity of the heart.

The acquisitions from the three different sensors are concurrent and each 20 ms, which is the fixed acquisition time, data are transmitted to a data hub (laptop, personal computer) through a wireless communication (band: 900 MHz, signal coverage: about 100 m in open space). As transmitter and receiver commercial chips were used [3]. The wireless connectivity avoids any movement impediment or measurement artifacts caused by obtrusive cables. Data are displayed in real-time and saved on a storage support for later analysis. Thanks to the small dimensions [10×16×3.5 cm] and the wireless connectivity, the instrument is really compact, portable and suitable to be used in all those applications where the subject has to move around with the instrument (e.g. athletes in the athletics track, measurements with subjects running in a treadmill, spaceflight monitoring, ...).

The real-time displaying of the physiological parameters, i.e. O_2Hb, HHb, oxygen saturation (SO_2), total hemoglobin (tHb), electrocardiogram signal (EKG) and photoplethysmograph signal (PLETH), is possible thanks to the acquisition software furnished with the instrument (figure 4.2). The absolute values of the optical and hemodynamic parameters are computed as explained in paragraph 1.4.2. Once the user presses play, an initial acquisition with all the wavelengths, injected alternatively into the tissue, is done, to calculate the scattering spectrum. This process takes about 5 seconds, after that the effective acquisition starts. With this software is also possible to select, before the measurement, the fat layer thickness and which sample is investigated (i.e. phantom, brain, gastrocnemius, vastus lateralis, ...), in order to use the right calibration parameters during the first phase of the measurement (paragraph 1.4.2) and to eliminate from the signal the contribution coming from the upper layer of the tissue (paragraph 1.5.2).

Figure 4.2: Acquisition software provided with the instrument.

4.2 In vivo application:

4.2.1 Aim of the measurement campaign

Muscle performances during exercise vary with the intensity, duration, and mechanics (shortening, isometric, stretching) of the contractions involved. In particular, muscular fatigue can be monitored with the identification of the anaerobic threshold (AT), which has been used to describe a shift in muscle metabolism during incremental exercise from predominantly aerobic energy pathways (oxygen consumption) to a greater reliance on anaerobic exercise sources (glycogen) [5], but the central concepts of this threshold have been the subject of debate over the last 25 years [6]. Recently, AT has been defined as an intensity of exercise above which oxygen uptake does not account for all of the required energy to perform work and has been associated with lactate accumulation in the blood, elevated carbon dioxide output, and increased ventilatory rate [7]. The lactate threshold (LT) is identified as the level of exercise where there is an abrupt increase in blood lactate concentration as exercise intensity increases. Corrective respiratory changes can also be identified through the measurement of pulmonary CO_2, by determining the ventilatory threshold (VT). These methods have been successfully used in clinical exercise testing and are widely used as predictors of aerobic endurance performances, and are considered indexes of the level of exercise

capacity [8]. The understanding of the fatigue mechanism is also important in some human diseases such as heart failure and serious infections, where it is necessary a rehabilitation process [9]. It is also of interest to monitor the muscle fatigue in terms of hemodynamic changes. NIRS technique was already employed for the assessment of the muscular fatigue during exercises [10, 11] and some preliminary attempt, in order to find a correspondence between all these techniques, was already proposed [12, 13].

This measurement campaign aims at testing the correlation of muscle and systemic physiological parameters, as assessed by exhaled gas analysis and by a combination of near-infrared spectroscopy, electrocardiography and photoplethysmography. Moreover we want to relate these parameters to systemic cardiovascular performance and skeletal muscle power and time to fatigue. The final goal is to find new physiological indexes and correlations between them, to better identify and quantify the phenomenon of the muscular fatigue. These can be then applied in the cardiac rehabilitation, in the muscular training and in the evaluation of muscle performances during spaceflight [14, 15].

4.2.2 Materials and methods

Metabolic cart

The metabolic cart is the instrument typically used to measure and analyze the cardiovascular and respiratory function of a subject, at rest or during physical exercises. In particular, the metabolic cart we employed [Quark CPET, COSMED, Italy] allows a breath by breath gas exchange data analysis [16]. As shown in figure 4.3, it is composed of five main components: 1) a personal computer, 2) a unit responsible for the calibration of the instrument, 3) a gas tank, with nitrogen (N_2), oxygen (O_2) and carbon dioxide (CO_2) used for the instrument calibration, 4) a tube inserted into a plastic mask to collect the expired gases and 5) a wireless belt to measure the heart rate. The parameters that can be extrapolated with the metabolic cart, and we are interested in, are: Oxygen uptake (VO_2), carbon dioxide (VCO_2), respiratory rate (RR), ventilation (VE), respiratory exchange ratio (RER), the ventilator equivalent for oxygen (VE/VO_2) and the ventilatory equivalent for carbon dioxide (VE/VCO_2). With these parameters is possible to extrapolate the Ventilatory Threshold (VT). As suggested by Gaskill et al. [17], VT was determined using the following three methods:

1. The modified V-Slope method (V-slope). VT is chosen at the VO_2 value corresponding to the increase in slope of the VO_2-VCO_2 plot, see figure 4.4(a).

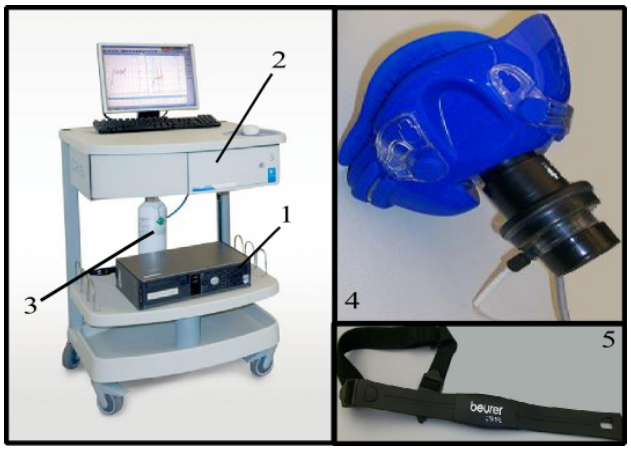

Figure 4.3: Metabolic cart, complete instrument and details.

2. The ventilator equivalent method (VEQ). VT is chosen at the time corresponding to the first sustained rise in the ventilatory equivalent of O_2 (VE/VO_2) without a concurrent rise in the ventilatory equivalent of CO_2 (VE/VCO_2), see figure 4.4(b).

3. Excess carbon dioxide method ($ExCO_2$). VT is chosen at the time corresponding to the first sustained rise from steady state in excess CO_2. $ExCO_2$ is calculated as ((VCO_2/VO_2)- VCO_2), see figure 4.4(c).

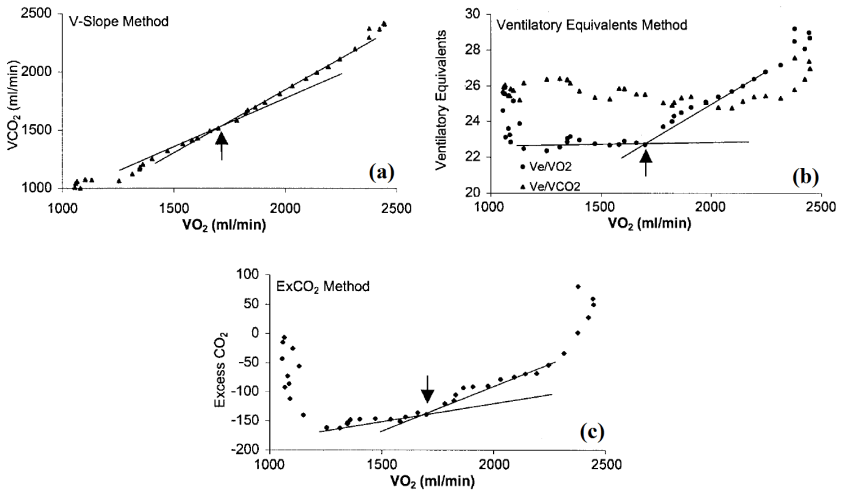

Figure 4.4: Visual determination of VT.

Measurement protocol

A group of 18 healthy adults, took part in this study. All subjects were informed about the protocol and the aim of the study, and they signed a consent approved by the ethical committee of the University of Houston. They were informed to refrain from alcohol and caffeinated beverages 4 hours before their testing appointment. A medical history questionnaire and physical activity questionnaire were compiled. A skin folder caliper test was performed on the tight of the participants, to determine the thickness of the fat layer, which has to be less than 10 mm to ensure clear NIRS measurement. All the participants had to fill out the Fitzpatrick skin type classification scale [18] to correlate the skin type with the readings taken by the NIRS instrument.

The experimental protocol of the present study consisted of one incremental cycle step exercise on an indoor ergonometer. The gear of the bike was maintained fixed and the subjects were instructed to cycle at 60 rpm, in this way the velocity was kept fixed. They could visualize the instantaneous pedal rate on a display connected to the ergonometer. After 5 minutes of warm up at 50 W, the work rate was increased by 15 W/minute. The exercise was stopped when the subject could no longer maintain the pedal rate, despite verbal encouragement, therefore till volitional exhaustion. After this point 5 minutes at 50 W were recorded. During the exercise subjects were asking to provide their rating of perceived exertion every 60 sec during the exercise test using the Borg 6-20 scale [19].

The optical probe was positioned longitudinally on the vastus lateralis muscle of the right leg and secured with an elastic bandage around the thigh. The repeatability of the placement through the subjects was guarantee by the employment of anatomical landmarks: we measured the distance between the ball joint, placed between the femur and the knee, and the femoral head and we placed the probe at half of this distance just above the fascia lata, as shown in figure 4.5(a). The EKG electrodes were placed in the configuration shown in figure 4.5(b), in order to reduce movement artifacts in the signal. The photoplethysmograph sensor was place on the the right thumb and the hand was positioning on the ergonometer' s handlebars avoiding too much pressure on the sensor that could influence the signal.

We also undertook a parallel measurement campaign in order to study the influence that a difference pedaling cadence could have on NIRS and metabolic cart signal. We asked to 7 subjects to repeat the previous protocol maintaining for the whole experiment a cadence of 80 rpm. Our aim was to understand if the muscle behaviour is cadence dependent and if the AT and the VT changed with the increasing of the exercise difficult.

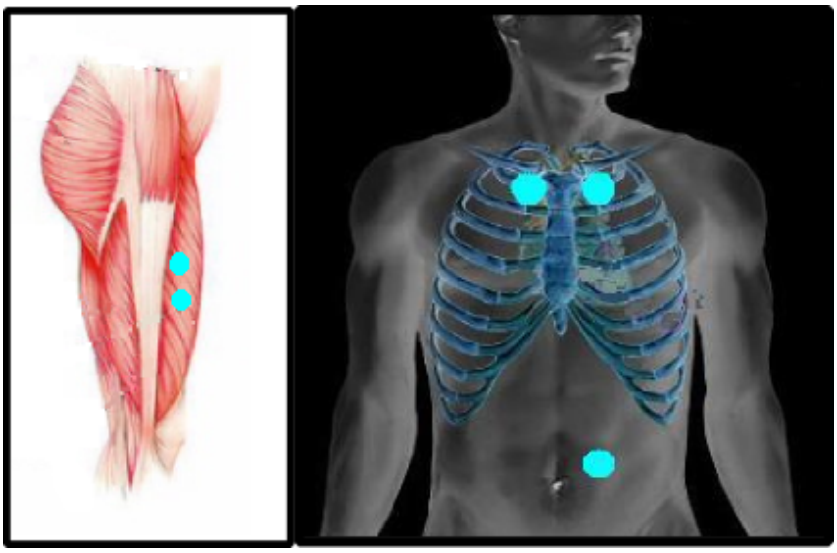

Figure 4.5: (a) NIRS probe positioning and (b) 3-lead EKG positioning.

4.3 Data analysis and preliminary results

A preliminary analysis for the signals coming from our instrument was implemented. In the following paragraphs only preliminary results for a typical subject will be shown. All the analysis were performed with a custom-made Matlab program. A complete analysis is still ongoing and will be finalized in the next months.

4.3.1 Physiological data

From the EKG signal the R-R series were extracted, while from the signal detected with the photoplethysmograph (PLETH), the distance between peaks was computed (P-P series), see figure 4.6. With these values the calculus of the Systolic Time Interval (STI) was possible. This parameter is the time between an R peak of the EKG and the corresponding peak in the PLETH signal, i.e. is the time that the blood needs to reach the body periphery. It is used to assess the left ventricular performances, particularly left ventricular ejection time, electromechanical systole, and pre-ejection period. We calculated the STI also as the difference between an R peak of the EKG and the minimum before the correspondent PLETH peak and between the R peak and the point of slope changing before the correspondent PLETH peak, as shown in figure 4.6. Finally we calculated the ratio between STI

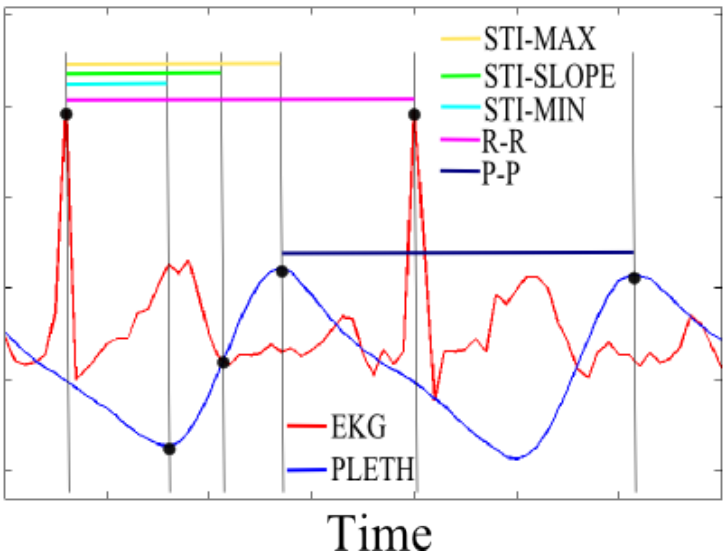

Figure 4.6: Calculation of R-R, P-P series and STI.

and R-R series. As shown in figure 4.7, during the exercise, the value of the R-R and P-P distance decreases (first row), because of the higher heart rate due to the increasing fatigue. As consequence the STI index decreases (second row). In the third row of figure 4.7, the ratio between the STI and the R-R values is shown. This ratio expresses the fraction of the time interval between two consecutive R peak that the blood needs to reach photoplethysmograph sensor. From a physiological point of view the heart rate (or the R-R series) represents the heart response to the exercise. The STI indicates the vascular response to the exercise and reflects, for example, how much the arteries dilate to support the increased demand of oxygenated blood. The ratio between these two values is an attempt to consider together these two different aspects, to represent the cardiovascular response.

4.3.2 NIRS data

The time courses of the absolute values of O_2Hb, HHb, SO_2 and tHb were extrapolated for the whole experiment. Then they were low pass filtered to remove the noisy effect of the pushing on the pedal. Their behaviour for a typical subject is shown in figure 4.8. During the 5 minutes warm up at the fixed wheel resistance, the tHb increases because when the muscular activity starts, there is an increase of the blood volume in the muscular fibers. When the wheel resistance starts to increase, i.e. the exercise becomes harder, the oxy-hemoglobin starts to fall and the deoxy-hemoglobin to increase, showing

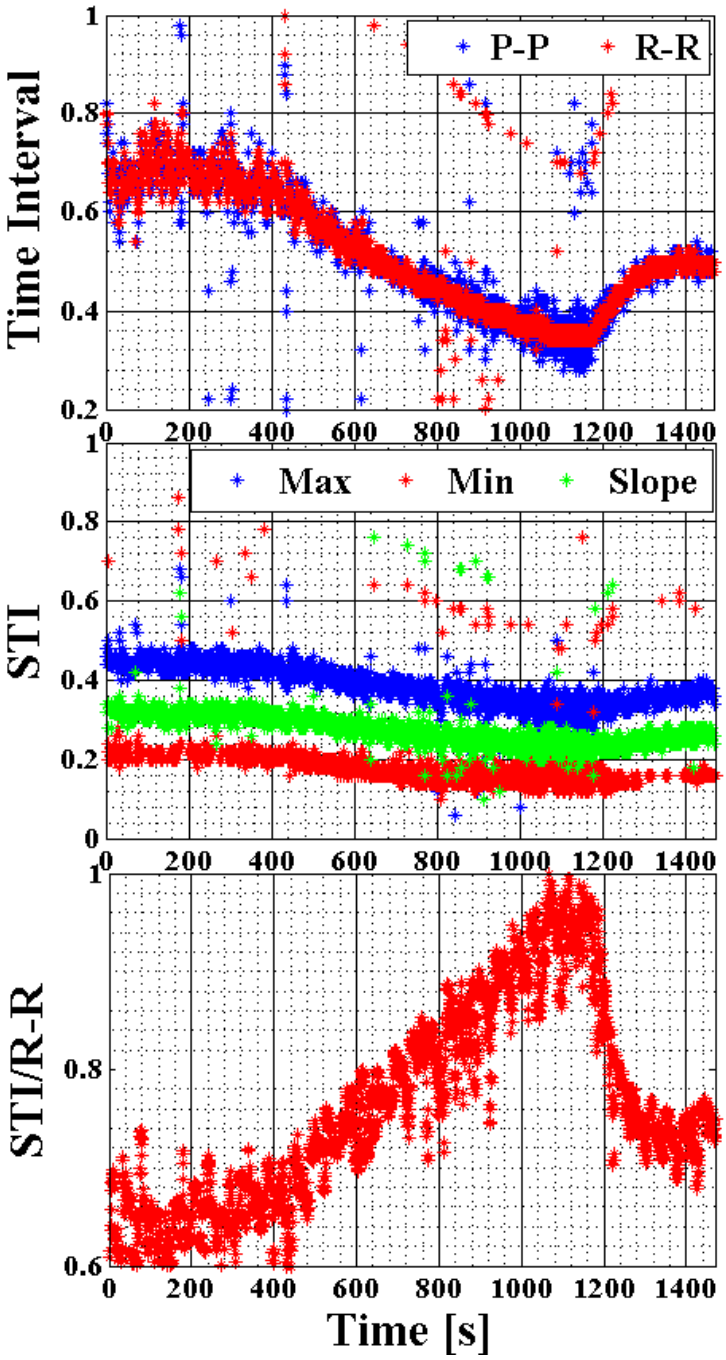

Figure 4.7: Physiological parameters: first row: systolic time interval (STI), second row: R-R and P-P series, third row: ratio between STI and R-R series.

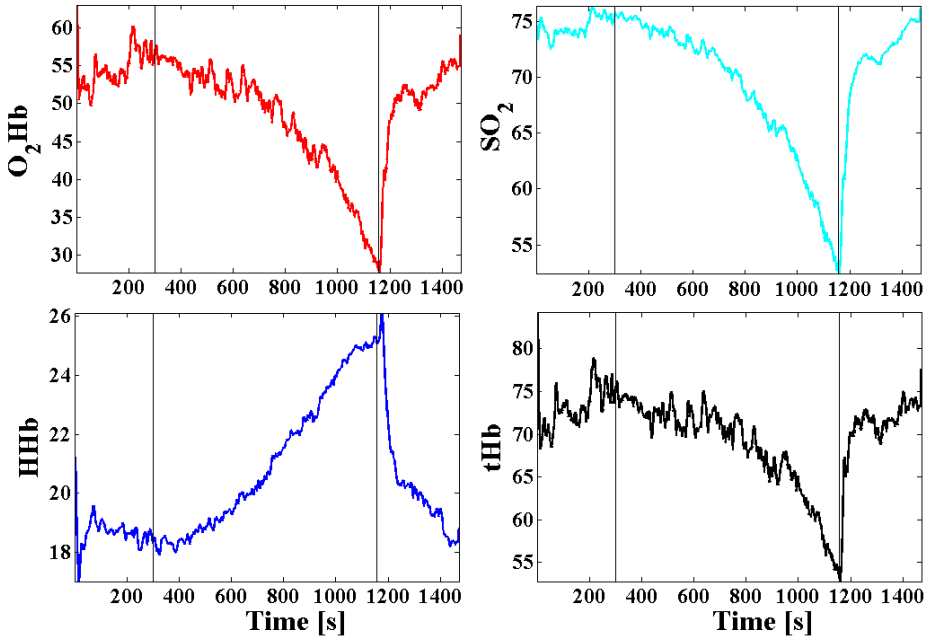

Figure 4.8: NIRS parameters during the whole experiment (60 rpm). Before and after the vertical lines: the warm up and recovery period at a constant wheel resistance.

the typical muscle metabolism process. The tHb decreases because of the gradually decrease of the O_2Hb concentration which is higher than the HHb increases, indeed the O_2Hb and HHb concentrations are in a ratio of 4 to 3. In the SO_2 and tHb graph, is possible to notice, during the exercise, a point where the signal slopes change (inflection point). The muscle, with the increasing of the exercise strength, has difficulty in relaxing after a contraction, causing a condition of hypoxia. The algorithm to find automatically the inflection points' temporal position has already been developed, but it has still to be apply among the subjects. Our aim is to understand if is possible to correlate it with the muscle AT.

In figure 4.9 the NIRS results for the same subject but during the experiment with 80 rpm of pedal frequency. Data were analyzed in the same way of the previous ones. The signals behaviour appears the same as before but the exercise was shorter than the previous one. The subject, pedalling with a higher frequency, reaches the exhaustion before. To understand if the muscle dynamic is the same, the calculus of the signal slope during the exercise (excluding the initial warm-up and the final recovery), on the unfiltered signal, was implemented. For this subject, we found an increase of the slope

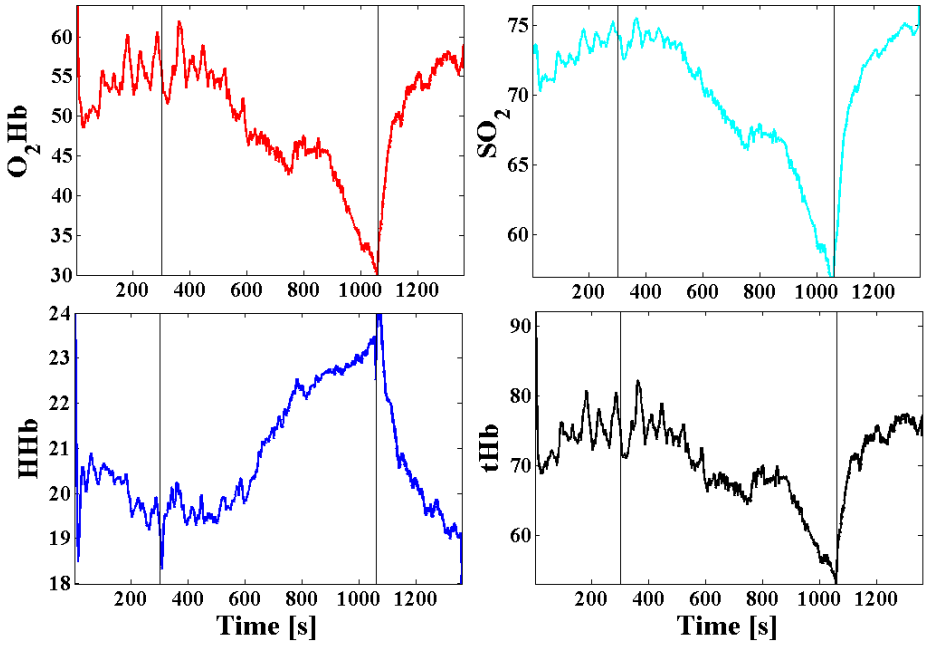

Figure 4.9: NIRS parameters during the whole experiment (80 rpm). Before and after the vertical lines: the warm up and recovery period at a constant wheel resistance.

absolute value for O_2Hb, HHb and SO_2 of respectively the 5.3%, 44.6% and 22.3%, while a decrease of the 6.8% for the tHb. Further investigations are necessary to understand if these values are consistent among the subjects.

4.3.3 Conclusion

The results shown are preliminary analysis on a subject. They suggest that it will be possible to understand the fatigue phenomenon through the employment of parameters of different origin, hemodynamic and systemic as well. In the following we plan to perform all the group analysis and to infer any correlation between the time evolution of NIRS, cardiovascular parameters (O_2Hb, HHb, tHb,SO_2, heart rate, systolic time intervals, etc.) and systemic parameters (oxygen uptake (VO2), carbon dioxide (VCO2), respiratory rate (RR), ventilation (VE), Respiratory Exchange Ratio (RER) and the ventilatory equivalents of oxygen (VE/VO2).

Bibliography

[1] Pulse Oximeter, OEM Board, EG00352, Technical Manual, Medlab 2009.

[2] One Channel ECG, OEM Module, EG 01000,Technical Manual, Medlab 2008.

[3] Texas Instrument, SWRS033G, Data sheet, CC1110Fx/CC1111Fx, 2008.

[4] D. G. Allen, J Appl Physiol 106: 358359, 2009.

[5] B. R. Soller, Y. Yang, S. M. C. Lee, C. Wilson and R. Donald Hagan, J. Appl. Physiol., 104: 837844, 2008.

[6] J.Davis, Med. Sci. Sports Exerc., 17: 621, 1985.

[7] K. Svedahl, B. MacIntosh, Can. J. Appl. Physiol., 28: 299323, 2003.

[8] A. Faisal, K. R. Beavers, A. D. Robertson and R. L. Hughson, J. Appl. Physiol., 106, 1553-1563, 2009.

[9] M. Kravari, I. Vasileiadis , V. Gerovasili, E. Karatzanos, A. Tasoulis, K. Kalligras, S. Drakos, S. Dimopoulos, M. Anastasiou-Nana and S. Nanas, International Journal of Industrial Ergonomics, 40(2),212-217, 2010.

[10] K. W. Rundell, J. Im,Physiological Assessment of Human Fitness-2nd Edition, P. Maud, C. Foster Editors, 2006.

[11] M. I. R. Pereira, P. S. C. Gomes and Y. N. Bhambhani, Sports. Med., 37 (7). 615-624, 2007.

[12] L. F. Ferreira, S. Koga and T. J. Barstow, J. Appl. Physiol., 103, 1999-2004, 2007.

[13] A. Borghi-Silva, C. Carrascosa, C. Carneiro Oliveira, A. C. Barroco, D. C. Berton, D. Vilaca, E. B. Lira-Filho, D. Ribeiro, L. E. Nery and J. A. Neder, Am. J. Physiol. Heart Circ. Physiol., 294, 2465-2472, 2008.

[14] S. Porcelli, M. Marzorati, F. Lanfranconi, P. Vago, R. Piot and B. Grassi, J. Appl. Physiol., 109(1), 101-111, 2010.

[15] B. R. Soller, M. Cabrera, S. M. Smith, J. P. Sutton, Nutrition, 18(10), 930-936, 2002.

[16] Quark CPET, Cosmed, technical datasheet 2010.

[17] S.E. Gaskill , B.C. Ruby, A.J. Walker , O.A.Sanchez , R.C. Serfass , and S.Leon, Med. Sc. Sport Exe., 0195-9131/01/3311-1841, 2001.

[18] Fitzpatrick, TB: Soleil et Peau, J Med Esthet, 2: 3334, 1975.

[19] Borg G., Scand J Rehabil Med., 2(2):92-8, 1970.